Nuclear Calorimetry on GeV Proton Induced Target Multifragmentation Reactions

AUTHOR(S):

Murata, Jiro

CITATION:

Murata, Jiro. Nuclear Calorimetry on GeV Proton Induced Target Multifragmentation Reactions. Memoirs of the Faculty of Science, Kyoto University. Series of physics, astrophysics, geophysics and chemistry 2000, 41(1): 1-132

ISSUE DATE:

2000-03

URL:

http://hdl.handle.net/2433/257650

Memoirs of the Faculty of Science, Kyoto University, Series of Physics, Astrophysics, Geophysics and Chemistry, Vol. XXXXI, No. 1, Article 1, 2000

Nuclear Calorimetry on GeV Proton Induced Target Multifragmentation Reactions

By

Jiro Murata *

Department of Physics, Faculty of Science, Kyoto University
Kyoto 606-8502, Japan

(Received February 5, 1999)

Abstract

A series of GeV proton induced target multifragmentation experiments has been performed at KEK-PS. The first experiment E337 has been carried out with a 12-GeV proton beam using four targets (gold, thulium, samarium, and silver). The second experiment E393 has been performed with a 8-GeV proton beam using three targets (gold, samarium, and silver). Intermediate mass fragments (IMFs; $3 \leq Z \leq 25$) have been detected with a 37-channel Bragg-Curve Counter array and their kinetic energy and charge have been determined. Lithium and beryllium fragments have been successfully separated according to their mass difference. Dependence on emission angle, target mass and IMF-multiplicity has been studied for the energy spectra. All the energy spectra are well described with "deformed moving source model". The fragment emission-angle dependence of the nuclear temperature and free nucleon density has been measured for the first time using yield ratios of the lithium and beryllium isotopes. "U-Shaped" angular distributions have been observed for both the temperature and free nucleon density. This fact suggests that their distributions in the emission source of IMFs should not be uniform. The existence of such non-uniformity could be the origin of the sideward-yield enhancement of the IMF production observed in GeV-energy proton-induced target multifragmentation reactions.

1 Introduction

Nuclear reaction dynamics is now well understood in low energy region. Collective model and shell model were crowned with success to describe properties of nuclei at low-excitation energies. In spite of close studies, most of research on the low energy nuclear reactions fail to grasp the property of nuclear matter in a wide phase space mainly because of their small energy transfer. In order to develop material science of nuclear matter, higher energy nuclear experiments are indispensable. There had been, however, little attention on the nuclear reaction dynamics in high energy experiments. In the last few decades, numerous attempts have been made to study high energy nuclear reactions. Hadron properties in nuclear matter attract a considerable attention, which are suggested by QCD studies in high energy physics. Confirmation of QGP is one of the hottest subjects in both high energy nuclear and particle physics. In the liquid-gas phase transition in water, critical opalescence signals the universal physics unique to the vicinity of the critical point. The QGP signatures can play an analogous role in QCD. In addition, first order liquid-gas phase transition of nuclear matter has been an interesting subject of study for a long time. The studies of nuclear liquid-gas phase transition and QGP phase transition have same structure on the meanings of structuralism in philosophy.

* Present address: The Institute of Physical and Chemical Research, Wako 351-0198, Japan

Knowledge of collision dynamics is indispensable for studying the nuclear matter experimentally. It is because nuclear collision is the only method for depositing a significant amount of energy to a nuclear system. Nuclear multifragmentation is one of the important subjects in studying hot nuclei, which has a main purpose of studying nuclear matter property and collision dynamics at the excitation energy of ~10 MeV/nucleon.

1.1 Nuclear Multifragmentation

Experimental studies on the nuclear reactions with high energy heavy ion beams were started in 1970's at Bevalac [1] with beam energies of $\sim$ 100 MeV/u to $\sim$ GeV/u. One of the main interests was the observation of limiting fragmentation in π rapidity region where πs are emitted from Δ or N^*. Limiting fragmentation phenomena had been observed at Fermi-motion energies (beam energy of 50 $\sim$ 100 MeV/u) as a saturation of excitation energy in target. Numerous studies on the recoil properties of deep spallation and fission processes were attempted [2][3][4][5]. After these attempts, clear limiting fragmentation at about proton beam energy of 10 GeV was reported as shown in Fig.1 [6] for the proton induced reaction.

Most of the experimental data could be understood by using a participant-spectator model. The fragments which are observed in projectile rapidity region are called as projectile fragments. On the other hand, those observed in the target rapidity region are called as target fragments. Both of them are originated from the spectator region. The participant region is considered to generate a fireball [7][8]. Studying the energy spectra of emitted particles, existence of another high energy component in addition to the fireball and the spectator was reported, which is referred as spectator fireball generated in the spectator region [9][10].

Because incident particles in these experiments have a large velocities, effect of incompressibility of nuclear matter could be examined. In particular, possible formation of the nuclear shock wave [11][12] attracts a great interest. In heavy-ion collision experiments, collective flow phenomena have

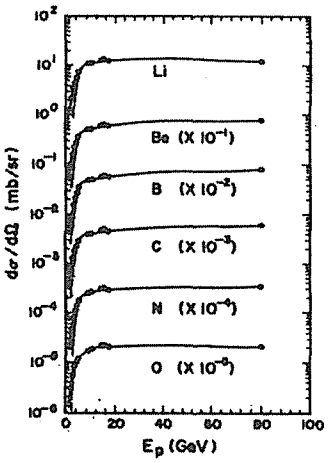

Excitation functions for Li-O fragmen emitted at 48.5° to the beam. The point at 80 GeV is taken from the Fermilab experiment. The dashed curves below 6 GeV represents the contribution of the multifragmentation mechanism.

Figure 1: Observed limiting fragmentation.
Reported by Porile et al.[6] in 1989.

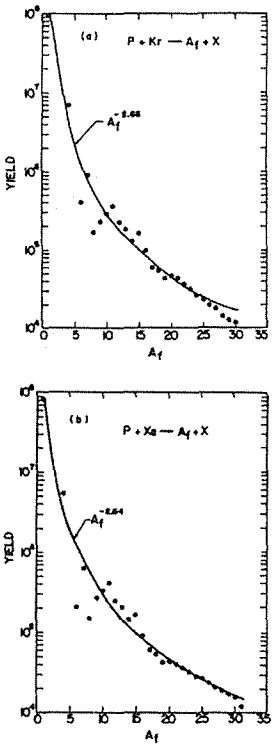

Fragment mass yield vs A_f for (a) p-Kr and (b) p-Xe collisions. The solid curve is a power law fit to the data.

Figure 2: Power law mass spectra.
Reported by A.S. Hirsh et al.[18] in 1984.

been observed [13], which might be associated with the sideward splash [14]. The collective flow was theoretically explained by VUU (Vlasov-Uehling-Uhlenbeck) equation [15]. From those phenomena, the incompressibility of nuclear matter can be studied [16].

Once the excitation energy is above region over the nuclear binding energy, spectator matter can be assumed to decay into many fragments within very small time scale of about $\sim 10 fm/c$. This phenomenon is called as multifragmentation. Searching the appearance of multifragmentation phenomena itself is an interesting subject in both experimental and theoretical studies.

The experiments on the multifragmentation have provoked a great deal of controversy. It is because the multifragmentation phenomena can be associated with nuclear liquid-gas phase transition of the nuclear matter. Porile et al. [17][18][6] have thrown new light on the subject. As shown in Fig.2, they showed that the fragment mass spectra in 80-350 GeV/c proton induced target multifragmentation reaction could be explained by power law mass distribution.

$$Yield \propto A_f^{-\tau} \tag{1}$$

Here A_f is the fragment mass and τ is power law index. This mass distribution is just same as that of cluster size distribution in vapor condensation. Similarly, the observed fragment mass spectra of

the multifragmentation reaction can, therefore, be considered to be a signal of condensed nuclear gas (nuclear fog).

For probing nuclear liquid-gas phase transition, considerable efforts were made to study multifragmentation phenomena. Existence of multifragmentation reactions is still not well confirmed [19]. In the multifragmentation, intermediate mass fragments (IMFs) play a key role. The definition of IMF is that the fragment charge Z_{IMF} is greater than 2 and smaller than $\sim 1/3$ of the system size; i.e. these fragments are lager than typical evaporated light particles and smaller than evaporation residues or fission products. Therefore, considering the nuclear vapor condensation in liquid-gas phase transition, IMFs can be treated as the nuclear fog.

First multifragmentation experiments were performed with emulsions [20][21]. As shown in Fig.3, violent disintegration of nuclei was observed. To overcome the difficulty on fragment charge identification using emulsions, high charge resolution experiments were performed with plastic detectors [22][23]. However, the results did not have complete fragment momentum informations.

In order to get information of the energies of IMFs, large solid angle detectors were built in the early eighties [24]. These studies contributed to confirm the fireball and the target spectator. High resolution tracking devices were built at the Bevalac (EOS [25]) and SIS of GSI (ALADIN [26]). Their devices were aiming to detect projectile fragments. On the other hand, low threshold detectors of new generation were developed at MSU (MINIBALL [27]), at GANIL(INDRA [28]), at Indiana University (ISiS [29]), at JINR (FASA [30]), and at KEK (present work) in mid nineties. The latter devices were developed for studying light ion induced reactions. ISiS, FASA, and out device are aiming to detect IMFs in GeV-proton induced target multifragmentation reactions.

Heavy ion induced multifragmentation studies have advantages for collecting all the emitted particles by using a reversed kinematics. Many observable can be determined as correlation data in these experiments (ALADIN and EOS). Such correlation results have a lot of information about the property of the expanding nuclear matter [26]. However, it is difficult to distinguish the origin of the produced fragments. The light particle induced experiments can select only the target rapidity region. In this case, origin of the detected fragments can be limited to the target spectator as shown in Fig.4. Therefore, the light ion induced reaction experiments have more clean kinematics than heavy ion induced experiments. On the other hand, the collection of the emitted particles needs large solid angle detector setups. For this reason, most of the devices used in the light ion induced experiments are 4π detectors.

ISiS is a low threshold charged particle detector, which consists of 162 triple-elements detector telescopes mounted in a spherical geometry, covering 74% of 4π in solid angle. Telescope elements are composed of gas ionization chamber and passivated silicon detector and thick CsI(Tl) scintillation crystal. Fragment charge up to Z$\sim$16 can be identified and isotopes are also distinguished for H, He, Li and Be fragments. Its main features is the wide energy dynamic range comparing to our detector at the KEK, owing to the thick scintillation counters. ISiS is a 4π detector with large acceptance, high energy resolution and large detection efficiency. However, scintillation counters have a sensitivity even for beam halo, which always causes a big problem in primary beam lines. Bragg Curve Counters (BCCs) used in the KEK experiments are insensitive to the beam halo, because it is essentially gas ionization chambers. ISiS has been used at IUCF, Satune II, AGS, and at LEAR using proton, ^{3}He, anti-proton and π beams of various energies over GeV.

FASA is a fragment multiplicity detector installed at JINR synchrophasotron, consisting of 55 scintillation counters made of thin CsI(Tl) films, five time-of-flight telescopes and a large-area position-sensitive parallel-plate avalanche chamber. Most of the acceptance is covered by multiplicity counters, therefore, fragment informations are obtained by the five telescopes. This detector is suitable to detect event multiplicity. On the other hand, each of BCC used in the KEK experiments can detect fragment charges and energies, therefore, they can be used in fragment correlation studies in spite of the relatively small solid angle coverage (20% of 4π).

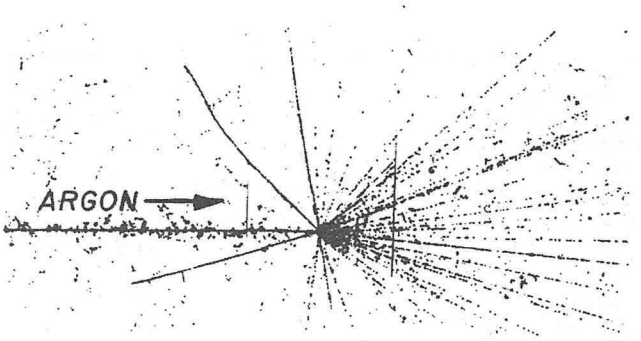

An interaction of an ^{40}Ar projectile, E=1.8 GeV/A, with a heavy emulsion nucleus that leads to catastrophic destruction of the projectile and target nuclei. This example of a central collision has 63 fragment tracks—the largest number of fragments encountered in this experiment.

Figure 3: Central collision events found in emulsion.
Reported in the first multifragmentation experiment [20].

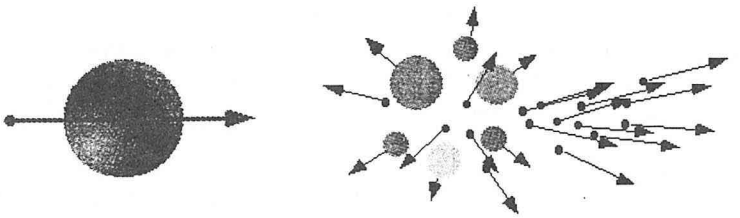

Figure 4: Schematic view of a proton induced multifragmentation reaction

1.2 Phase Diagram of Nuclear Matter

Owing to the high energy beam accelerators, it is now possible to study properties of nuclear matter in a wide phase space. Determining the phase diagram and the equation of states of nuclear matter may be the ultimate objective of nuclear physics. The interest is similar to the material science. Rich structure of the nuclear phase diagram have been predicted by many theorists [31][32][33].

One of the primary motivations to study the nuclear phase diagram is a creation of the pre-hadronic phase of the early universe or the core of neutron stars [34]. Appearance of QGP is the most spectacular example of a nuclear phase transition. The structure of nuclear phase diagram is determined by properties of the nuclear interactions [35][33]. An example of predicted nuclear phase diagram is shown in Fig.5.

The idea of the nuclear liquid-gas phase transition was inspired by the Van der Waals behavior

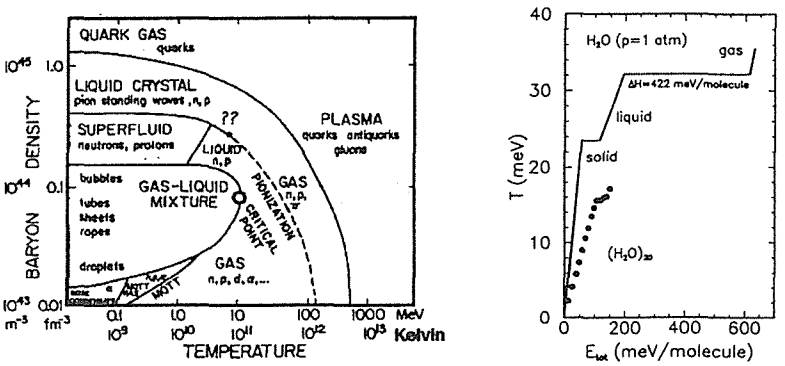

Figure 5: Example of the predicted nuclear phase diagram and the caloric curve of H_2O.

of the nucleon-nucleon force [36][37][38][39]. They claimed the critical point of the liquid-gas phase transition should be located at a critical temperature of about 15 - 20 MeV and a critical nuclear matter density of about 1/3 - 1/2 ρ_0 (normal nuclear matter density).

One of the experimental probes for searching the liquid-gas phase transition is the power law index for the mass spectra mentioned before. According to a percolation theory, the fragment size distribution at the critical point should follow a simple power law, in case of the second order phase transition [40]. For many universality classes, the critical exponent τ (power law index) should lie between 2 to 3. In fact, the experimental observation of the power law mass spectra reported the critical exponent around the value [41][18]. A lot of the studies on the nuclear criticality had been made both experimentally and theoretically [42][43][44][45][46][47][48][6]. After studying the inclusive mass spectra, critical point exponents have been studied on exclusive experiments [49][50][51][52][53][54][55][56][57]. EOS collaboration has reported the critical point exponents from the charge correlations measured for the ^{197}Au on C reaction at 1 GeV/u [25][58][59]. Extracted results are significantly different from the results of the percolation or mean-field theory [25]. As the result, despite enormous efforts, the attempts to deduce critical parameters remained elusive [60][61].

Nuclear calorimetry is another approach to explore the nuclear liquid-gas phase transition. Nuclear caloric curve is predicted to be similar as that of H_2O (Fig.5). However, there are difficulties to extract the reliable caloric curve caused by the finite size of the colliding system [62][63]. Moreover, since no external field can be applied in the laboratory, the expansion may occur prior to the disassembly [64]. In spite of above difficulties, possibility of probing the caloric curves on small cluster system has been studied [65][66][67]. They predicted that nuclear colliding systems may also exhibit sufficiently clear signatures for the phase transition.

In their pioneering work, Bethe [68] and Weisskopf [69] introduced the concept of a nuclear temperature in 1937. Determination of the nuclear temperature is indispensable for the nuclear calorimetry [70]. Inverse slope parameters of the kinetic energy distributions of the emitted particles have been widely used. In intermediate and relativistic energy collision reactions, these energy spectra suffer from some dynamical effects [71][72][73][74], and Fermi motion[75]. Most direct way to measure the nuclear temperature is to use relative population ratios of excited states [76][74][77][78][79][80][81]. This method is insensitive to the dynamical effects, but, those experiments require demanding coincidence measurements of the decay products. It is experimentally hard to achieve high energy

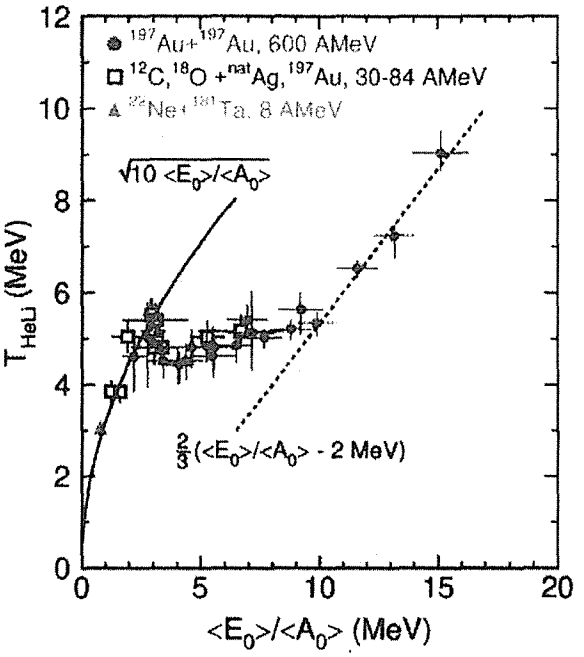

Figure 6: Nuclear caloric curve reported by J. Pochodzalla et al. in 1995. Isotope temperature T_{HeLi} was used for the thermometer [89].

resolution and sufficient detection efficiency to obtain the relative population ratios of excited states. A method using relative-population abundance of the produced isotopes is called isotope temperature [82][83][84][85][86][87]. The isotope temperature can be extracted from single particle yields. All the attempts ever tried were using a double yield ratio technique for the extraction of the isotope temperatures. This technique has been widely used, but, available combinations of the double isotope ratios are strongly restricted. More general formalism for extracting isotope temperature is discussed in this paper (Sec.5). In spite of the experimental simplicity, the isotope temperature method is sensitive to the secondary decays of unstable nuclei. A simple correction method for the sequential decay was introduced by M.B. Tsang et al. in 1997 [88]. They suggested that the sequential decay effects can be corrected by a correction of the double ratio. A modified technique on the direct yield correction is also introduced in this paper (Sec.5).

Using the isotope temperature, the first experimental determination of the nuclear caloric curve was reported in 1995 [89]. In Fig.6, isotope temperatures obtained by the double yield ratios of He and Li isotopes (T_{HeLi}) were plotted as a function of the total excitation energy per nucleon ($\langle E\rangle/\langle A\rangle$). The rising curve in the low excitation energy region below 2MeV is compatible with the low-temperature approximation of a liquid fermionic system. The plateau region for T = 4.5 - 5 MeV may be related to the constant temperature in the liquid-gas mixed phase. Beyond a total excitation energy of 10 MeV per nucleon, a steady rise is seen, which may be associated with the appearance of the nuclear gas phase. This caloric curve figure is very striking, however, the interpretation of this result has been the subject of controversy [90][58][91][92][93][94][95][96]. Central issue is the problems of the thermometer and time evolution of the collision. Similar attempts have been tried to re-confirm

the caloric curve using excited state population ratios, however, most of them under estimate the temperatures at high excitation energies where rising line is expected. Moreover, the temperature rising is confirmed at the high excitation energy region but no plateau are observed in the results of INDRA [97]. It was pointed out that there might be some problem in the assumption for the isotope temperature because the colliding system has a finite size. Understanding the meanings of the observed isotope temperatures in nuclear collisions have been attempted theoretically [98]. Freeze out temperature of the probe fragments and maximum achieved temperature in the collision can not be treated as the same one. Framework of Quantum Molecular Dynamics (QMD) [99] has advantages on the treatment of the fragmentation process. Great progress on interpretation of the experimental results of nuclear calorimetry have been made by the QMD studies. However, QMD cannot be applied for the intermediate energy nuclear colliding systems. The main theoretical difficulty lays on the large energy scale difference between the collision dynamics (GeV) and fragmentation process (MeV). Although a large number of studies have been made, there is little consensus of the interpretation for the caloric curve as a signal of the nuclear liquid-gas phase transition.

In order to study the nuclear calorimetry, dynamical effects and thermal effects should be separated from each others. Light particle induced reactions have the advantage of the clear kinematics for studying the collision dynamics. In the next section, topics on the collision dynamics on this field is introduced. All attempts for the confirmation of the caloric curve is made by the heavy ion induced experiments. A similar work on the light projectile induced reactions is required. The present study provides the first experimental results of probing nuclear calorimetry as a function of fragment emission angles in proton induced reactions.

1.3 Sideward IMF Yield Enhancement

Particle emission from a thermally equilibrated source should be isotropic. The resultant energy spectra can be described by thermal energy distribution with Coulomb energy shifts. Most of the experimental results of multi-particle production have been explained by this idea. This idea is based on the assumption of thermal equilibrated source which has spheric-symmetrical geometry.

Sideward peaking of the fragment emission in proton induced reaction was first observed in 1975 with 28 GeV protons on U and Au reactions at AGS [100]. Because of the peak angle towards 70°, the sideward peaking was considered to be an evidence for the generation of nuclear shock waves. Radiochemical experiments were attempted to study beam energy dependences of the sideward peaking phenomena in a wide energy range from a few GeV to 400 GeV [101][102][103][104][105]. In addition to the interest of the second limiting fragmentation at π rapidity region where πs are emitted by Δ and N^*, drastic change of the angular distribution from usual forward peaking at proton beam energy of 3.0 GeV to the sideward peaking at 11.5 GeV was found (Fig.7). Although a lot of studies have been made on this subject, little was known about the sideward peaking because fragment energies were not measured in the radio chemical experiments.

Owing to the improvement of the counter techniques, exclusive counter experiments became possible. 12 GeV proton induced reactions were studied at KEK-PS from 1993 and the sideward peaking around 70° was observed (KEK-PS E288, see next section). The present results are written in Sec.4 and Sec.7.

Similar results of the sideward peaking have been reported by Indiana University group using ISiS at AGS [106]. As shown in Fig.8, in the case of 5.0GeV/c π^- and 10.0, 12.8, 14.6 GeV/c proton beams the sideward peaking was found for over 10 GeV/c. Reported sideward peakings were obtained on the condition of IMF-multiplicity ≥ 4. Low IMF-multiplicity events showed forward peaking angular distributions which are similar to that of the results of low-beam energy experiments. The IMF-multiplicity dependence on the angular distribution is shown in the right-side frame of Fig.8. The

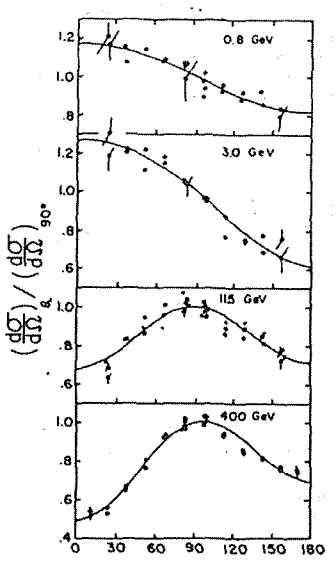

Angular distributions of ^{24}Na from the interaction of ^{238}U with 0.8–400 GeV protons. The various points at each angle represent the results of replicate experiments. The solid points at 11.5 GeV show the results obtained for a "thin" (100 μg/cm^2) target. Typical error bars are shown at each energy. The curves constitute a least-squares fit of Eq. (1). The differential cross sections are normalized to unity at 90°.

Figure 7: Beam energy dependence of angular distribution.
Drastic change from forward peaking to sideward peaking can be found.
It was reported by Fortney and Porile in 1980 [17].

observed beam energy dependence is striking, however, the forward peaking observed for low IMF-multiplicity events is inconsistent with the previous results of inclusive studies shown in Fig.7 and also with the inclusive results of the KEK-PS E288 experiment. The close study on the fragment energy spectra in the KEK experiment is required, where the sideward peaking has been found even for inclusive events.

Theorists have struggled to explain the sideward peaking phenomena. One of Relativistic Quantum Molecular Dynamics (RQMD), which is mainly developed by T. Maruyama [107], have been tried to explain the sideward peaking with "nuclear donuts" formation. Probability of the toroidal-shaped nuclear matter in a heavy ion collision was pointed out by many theoretical studies [108][109][110]. Similarly, toroidal shaped matter formation in water droplets collision is also reported in [111]. In addition, time evolution of the expanding nuclear matter can be examined using the same formalism. In spite of the great theoretical improvement, quantitative explanation of the fragmentation phenomena have not been succeeded. Accurate experimental data with sufficient statics is required for the progress of theoretical study on high energy nuclear dynamics.

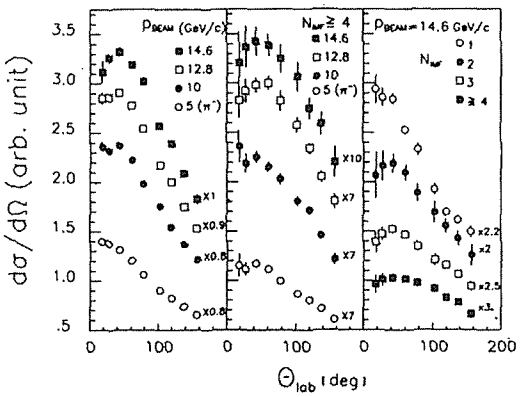

Angular distributions of carbon fragments from a ^{197}Au target. Left frame: inclusive data for 10.0, 12.8, and 14.6 GeV/c protons and 5.0 GeV/c π^-; center: data for the same beam momenta gated on IMF multiplicity $N_{IMF} \geq 4$; and right: 14.6 GeV/c proton data gated on IMF multiplicity. Legends on the figures identify curves; relative cross sections are indicated by scale factors associated with each angular distribution.

Figure 8: Angular distribution reported by Indiana University group. $N_{IMF} \geq 4$ events are selected. Clear sideward peaking can be seen [106].

1.4 KEK-PS Target Multifragmentation Experiments

First target multifragmentation experiment using 12 GeV proton beam at KEK-PS (E288) was performed in 1993 using Bragg Curve Counters (BCCs) [112][113][114]. As shown in Fig.9, fragment yield enhancement around 70° was observed for the inclusive data. Angular distribution of IMFs which were coincident with one extra IMF emitted toward 90° in opposite hemisphere showed strong 70° peaking comparing to that of inclusive data.

The coincidence requirement is considered to be high IMF-multiplicity selection, which can be roughly treated as a centrality selection [115]. From this point of view, the enhancement of the sideward peaking in the coincidence events of E288 seemed to be associated with the central collision. The correlation between particle multiplicity and centrality of the collision has been widely accepted in the heavy ion collisions. The IMF-multiplicity has been treated as a measure of impact parameters because of the results of [115]. IMF-multiplicity dependence of fragment energy spectra, isotope temperature, and free nucleon density are discussed in the later sections.

The possible origin of the sideward peaking phenomena was considered as the formation of nuclear shock wave or toroidal-shaped nuclear matter. In order to make an extensive study on the IMF-multiplicity dependence, a new experimental setup with a large acceptance which can measure the IMF-multiplicity was constructed.

Using the 37ch-BCC array which had almost 20% of 4π acceptance, a new experiment using the 12 GeV proton beam with four targets (gold, thulium, samarium, silver) was performed in 1996 (KEK-PS E337) [116] [117][118][119]. The large acceptance was required for the IMF-multiplicity

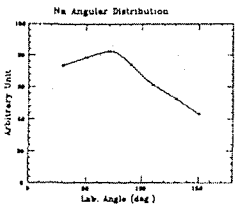

Angular distribution of Na isotopes produced in Au(p,X):Ep=12GeV reaction.

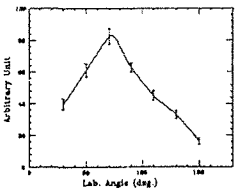

Angular distribution of IMFs which are coincident with one extra IMF emitted toward the 90° in the opposite hemisphere. Reaction is Au(p,X):Ep=12GeV. Energy of the extra IMF is selected above 1.5 MeV/u to reject the contribution from fission event.

Figure 9: Observed sideward peaking in E288.
Upper figure shows the inclusive data and lower figure shows the coincidence data [112].

determination. All the counters can detect fragment charge and energy for particle correlation studies. The main interest was the angular dependence of fragment emission, therefore, high resolution fragment detector array was required, which have higher priority than 4π multiplicity counters. Most of the previous studies on GeV proton induced reactions had attention only in the beam energy dependence than target dependence. However, the target mass dependence is concerned in E337. On the requirement for a systematic understanding of the sideward peaking, four targets were selected, which can be made as thin foils. For the purposes on probing the nuclear matter properties, target mass region was determined to have sufficient source size. Present paper describe the E337 experiment and the results of the data analysis. The experimental setup is introduced in Sec.2. As written in Sec.4, the E337 found that, there is small IMF-multiplicity dependence on the sideward peaking. The enhancement of the sideward peaking observed in the coincident data of E288 was understood as an observation of strong back-to-back inplane correlations between two IMFs [118] (Fig.10). Detailed studies on the shape of the energy spectra and isotope temperature analysis are introduced in this paper.

In order to study the beam energy dependences, an additional experiment was performed in 1997 (KEK-PS E393) using a 8GeV proton beam with three targets (gold, samarium, silver). The beam energy of 8GeV was selected because the critical phenomena were reported around E_p=10GeV as mentioned before. In addition, as shown in Fig.11, obtained results on E337 by a nuclear temperature

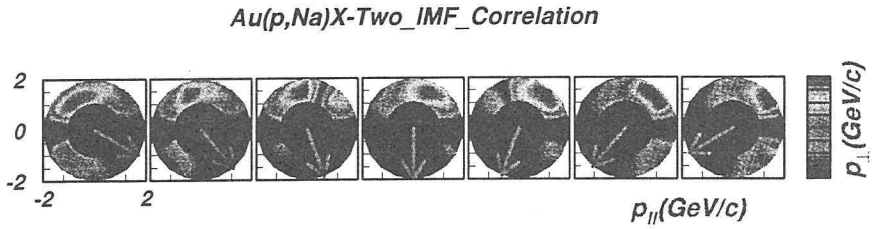

Figure 10: Inplane two IMFs correlation. Invariant cross section of Na fragments with requirement of one IMF detection towards the direction indicated by the arrows.

analysis indicated that the fragment source matter seemed to be just in hadron gas phase[117] , therefore, lower excitation data was needed to confirm the existence of liquid-gas mixed phase in the same experimental setup and the same analyzing procedure. The results of E393 is also the main part of this paper together with the results of E337. Beam energy dependences of isotope temperature and sideward peaking is discussed in later sections.

Analysis of the KEK experiments are separated into energy spectra analysis, isotope temperature analysis, and fragment correlation analysis. The present paper focuses on the results of isotope temperature analysis. Overview of the analysis is written in the next Sec. Detailed discussion on the energy spectra and particle correlations are presented in many master works (Y. Ohkuma [120], F. Kosuge [121], Y. Shibata [122], R. Kubohara [123], and Y.J. Tanaka[124]).

1.5 Overview of Analysis

Determining energy spectra of the fragments is the starting point for most of the analysis. Data analysis for identifying the charge and/or mass of the light fragments is introduced in Sec.3. Standard off-line analysis procedures for the experiment using BCC are written. Resultant energy spectra are discussed in Sec.4. Several models based on thermal moving source are studied. The sideward yield enhancement cannot be explained with a simple moving source model. We found only one model called "deformed moving source model" can well reproduce all the energy spectra. The interpretation of the results of the model analysis is discussed in Sec.4 and Sec.7.

Probing nuclear temperature is one of the main subjects of this paper. Several methods are discussed and results of one method called isotope temperature on E337 and E393 data are introduced in Sec.5. The interpretation of the isotope temperature is discussed in Sec.7.

As introduced in Sec.5, not only nuclear temperature but also nuclear densities can be obtained by isotope yield ratios. The procedure and experimental results are written in Sec.6.

Obtained results of the fragment energy spectra, nuclear temperature, and nuclear densities have information about the collision dynamics and the nuclear matter properties. For studying the colliding system, it is impossible to separate information of the dynamics and matter properties. Considering the geometrical condition and time evolution of the collision, obtained results are interpreted as a signal of expanding nuclear matter system around the critical point of liquid-gas phase transition. It is discussed in Sec.7.

The fragment emission angle dependence of the temperature and densities have been observed for the first time. The origin of the non-uniform fragment emission can be understood by the present work. In addition, the nuclear liquid-gas phase transition is extensively examined in the present

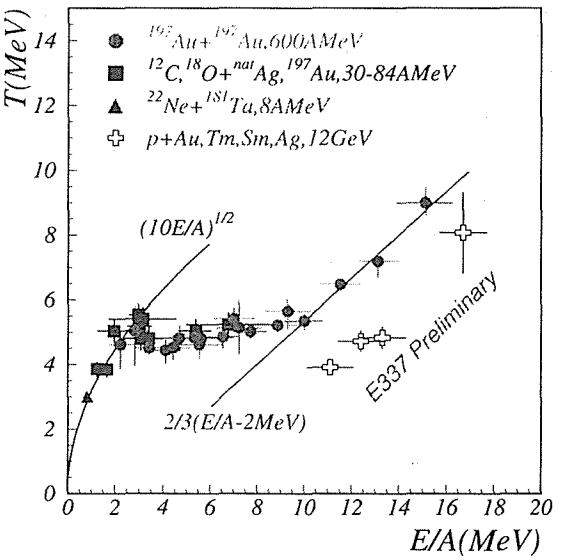

Figure 11: Preliminary results of caloric curve obtained in E337. Obtained points are seemed to be in the gas region.

study. The results are discussed in Sec.7.

2 Experimental Setup

A series of GeV proton induced target multifragmentation experiments have been performed at KEK-PS. The first experiment E337 has been performed with 12GeV proton beam using four targets (gold, thulium, samarium, silver). The second experiment E393 has been performed with 8GeV proton beam using three targets (gold, samarium, silver). Produced intermediate mass fragments (IMFs; $3 \leq Z \leq 25$) are detected by a 37-channel Bragg-Curve Counter array. Kinetic energy and charge numbers are determined for all the detected IMFs. In addition, mass separation for lithium and beryllium fragments are performed. Emission angle dependences, target mass dependences, IMF-multiplicity dependences on the detected fragment energy spectra can be studied using the setup.

2.1 Beam Line

The first experiment KEK-PS E337 using 12GeV proton beam was performed at EP1B beam line of KEK-PS North Counter Hall. EP1B line had been constructed just before running the experiment E337. It was because another primary beam line at East Counter Hall (P1 beam line) did not have sufficient radiation shield for using high intensity primary beam. In addition, P1 beam line had a problem that there were many beam line materials before coming to the experimental area. The problem was beam halo production. The EP1B beam line was newly constructed to settle the

problems. After finishing data taking of E337 at the EP1B line, the previous P1 beam line was reconstructed in order to reward the request for such high intensity primary beam experiments. The later experiment KEK-PS E393 using 8GeV proton beam was performed at the modified P1 beam line at the KEK-PS East Counter Hall after moving all the experimental setup from EP1B line.

Both of the experiment was running under double slow extraction mode of the accelerator. The experiments had become possible owing to the success of the double extraction mode. The beam profile was strongly depending on the accelerator condition. It was a big problem for reducing beam halo. Huge background events were caused by the beam halo, which main component were assumed to be neutron. To subtract the background events in off-line analysis, stable beam condition was indispensable. In order to get proper background runs, event runs and background runs were alternately taken within about five hours, in which time beam condition can be recognized as nearly constant. For both of the experiments, beam intensities were monitored by a ion chamber [125].

2.1.1 KEK-PS EP1B Primary Beam Line

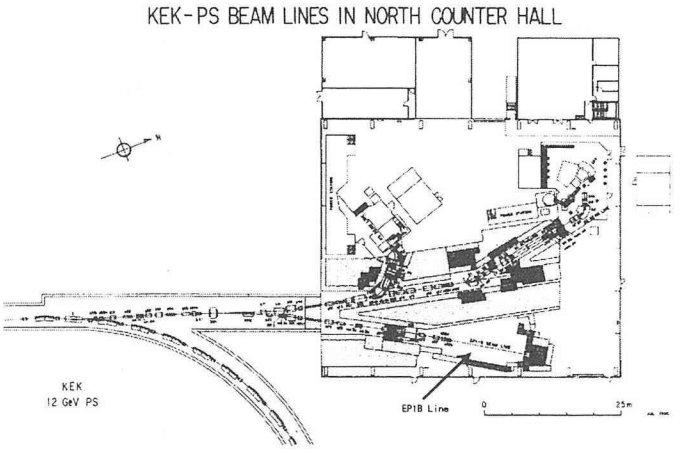

Figure 12: Overview of the KEK-PS EP1 Experimental Hall. EP1B line is shown by an arrow.

EP1B primary beam line was constructed at KEK-PS North Counter Hall for high intensity primary beam experiments. In order to reduce the beam halo, extracted proton beam was transported to the experimental area with a few windows which were indispensable to the vacuum security. After the construction of EP1B line at December 1995, test experiments were performed using the full E337 experimental setup from December 1995 to March 1996. E337 data taking was started from April 1996 and finished in June 1996. All the beam time was shared with another users in the East Counter Hall on the double slow extraction mode.

2.1.2 KEK-PS P1 Primary Beam Line

The second experiment E393 has been performed at P1 line in KEK-PS East Counter Hall after moving all the experimental setup. Beam line reconstruction for improve the beam quality and intensity was completed in September 1997. E393 data taking was started at October 1997 and

Beam Energy	12GeV
Beam Intensity @ Main Ring	$\sim 4 \times 10^{12}$ particles/spill
Beam Intensity @ EP1B	$\sim 3 \times 10^{9}$ particles/spill
Spill	2.0 sec
Repetition	4.0 sec

Table 1: Beam conditions for E337 at EP1B line.

Beam Energy	8GeV
Beam Intensity @ Main Ring	$\sim 3 \times 10^{12}$ particles/spill
Beam Intensity @ P1	$\sim 3 \times 10^{9}$ particles/spill
Spill	0.5 sec
Repetition	2.6 sec

Table 2: Beam conditions for E393 at P1 line.

finished in December 1997. As same as in E337, all the beam time was shared with another users at North Counter Hall on the double slow extraction mode.

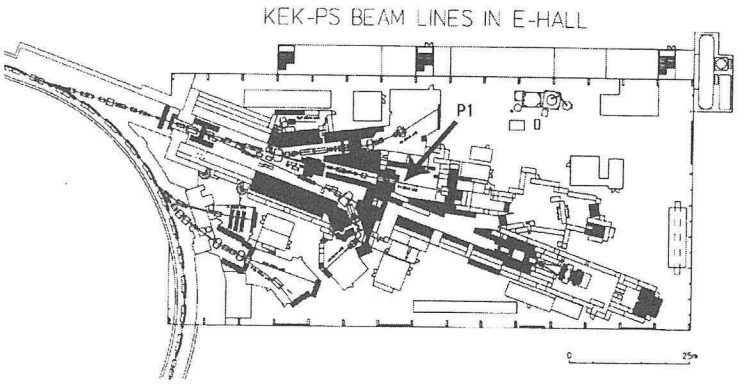

Figure 13: Overview of the KEK-PS EP2 Experimental Hall. P1 line is shown by an arrow.

2.2 Targets

Gold, thulium, samarium, and silver targets were used in E337 and Gold, samarium, and silver targets were used in E393. Gold and silver targets were made of very thin self support foils. Thulium and samarium targets were made of coating on Mylar backing. Geometry of the target holder is shown in Fig.14.

For the alternative data taking of the event run and background run, the targets had to be able

	A	Z	Thickness	Structure
Au	196.97	79	0.633 mg/cm^2	Self Support
Tm	168.93	69	0.582 mg/cm^2	Mylar Backing
Sm	150.36	62	1.596 mg/cm^2	Mylar Backing
Ag	107.87	47	0.608 mg/cm^2	Self Support
Backing Mylar	-	-	0.149 mg/cm^2	-

Table 3: Target Summary Table for E337

	A	Z	Thickness	Structure
Au	196.97	79	0.754 mg/cm^2	Self Support
Sm	150.36	62	0.446 mg/cm^2	Mylar Backing
Ag	107.87	47	0.547 mg/cm^2	Self Support
Backing Mylar	-	-	0.149 mg/cm^2	-

Table 4: Target Summary Table for E393

to be changed quickly in the vacuum chamber. The target changing should be remote controlled from the control room. For the requirements, target driver was developed as shown in Fig.14. The stepping motors used in the target driver were controlled by TTL signals generated in the target driver operating PC.

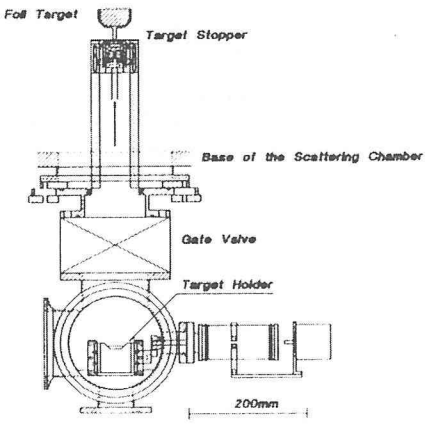

Figure 14: Design of the target driver. Foil targets were exchanged remotely in the vacuum chamber.

2.3 Bragg Curve Counter (BCC)

All the fragment detector used in the E337 and E393 experimental setup were consisted by Bragg Curve Counters [114]. Principle of the Bragg Curve Counter (BCC) is shown in Fig.15. BCC is a kind of gas ionization chamber with a Frisch grid. Incident fragments will be stopped with a Bragg curve-shaped energy loss in the counter gas volume. It is well known that the maximum energy loss at the Bragg peak is nearly proportional to the charge number of the fragments. Bragg curves for various fragments in P10 gas (90% argon + 10% methane mixture gas) are shown in Fig.16. As shown in Fig.16, the peak hight of the Bragg peak could be roughly treated as being proportional to the charge numbers of the incident fragments. Therefore, we can get information about the charge numbers of the incident fragments using the Bragg peaks.

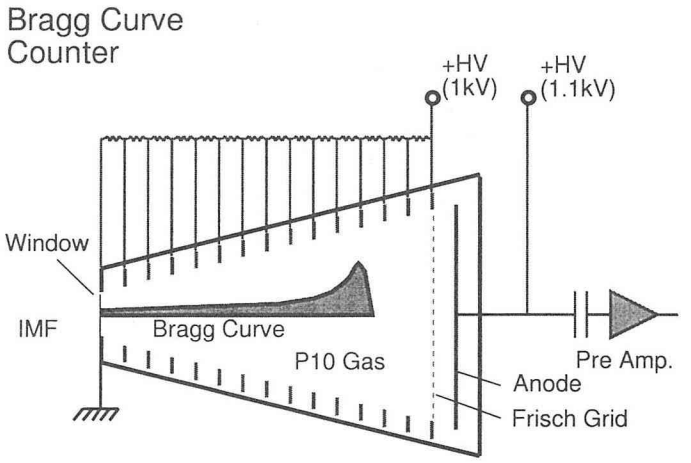

Figure 15: Principle of the Bragg Curve Counter.

In Fig.15, there is a constant electric field which is nearly parallel to the incident path of the fragments. Once a fragment come into the detector, gas ionization will be occurred belong the particle stopping path. Then the created free electrons drift towards the anode and make a signal. Since the electron drift velocity is almost constant in the gas, electron detecting timing information at the anode can be used as a ionized position information from the anode.

Typical electric field is about $30V/cm$. Since this bias voltage is in the region of ionization chamber, collected number of the electrons is same as the number of the ionization. Therefore kinetic energy information can be obtained by the total detected charge in a signal.

At the anode, timing evolution of the voltage in a signal pulse is expected as the Bragg curve itself. Therefore, Bragg peak can be determined as the peak hight of the output signal. At the same time, kinetic energy information can be extracted by the total charge of the signal. In addition, information of the stopping range in the counter gas can be determined as the timing length of the output signal.

The Bragg curve shown in Fig.16 was made by Northcliff's energy loss table [126]. There are no theoretical formalism which can estimate proper energy loss at such very low energy region. The exact peak hight does not have to be estimated for the charge identification. The fact is sufficient for the fragment charge determination, that each fragment has its own original Bragg peak, which is

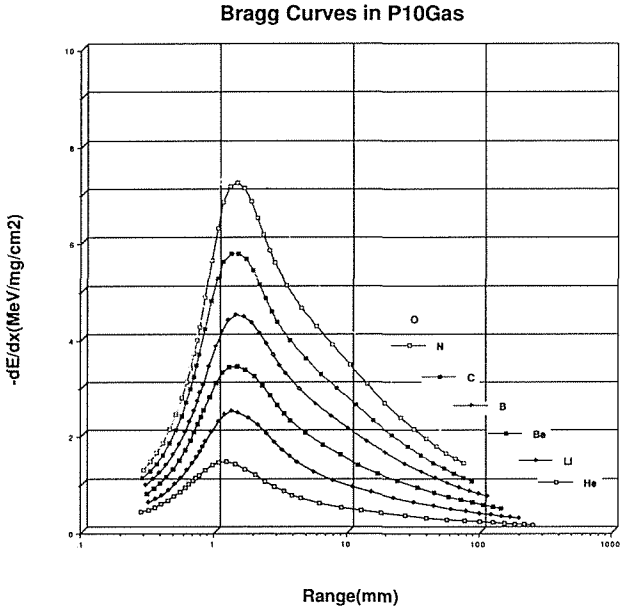

Figure 16: Bragg curves of various ions in P10 gas.

nearly proportional to the charge number of the fragment.

2.3.1 Construction parameters

Construction parameters are written in Tab.5 and Tab.6. $SBCC1$, $SBCC2$, $S_{1/2}BCC1$, $S_{1/2}BCC2$, and $CBCC$ are the name of the five BCCs. The differences of them will be shown in the next section.

Detector Window Detector windows had to be very thin in order to detect low energy heavy fragments because of their large stopping power. Counter gas and vacuum space around the targets were separated with the windows, therefore, it had to be air-tight window. The selected window materials are written in Tab.5 and Tab.6. $1.8\mu m$ Mictron or $2.15\mu m$ Mylar were used. $1.8\mu m$ Mictron is thin and strong, but hard to stretch. $2.15\mu m$ Mylar was the only window material which could be used in the construction of the CBCC window, which had large spherical shape (Fig.23). In the first experiment E337, all the in-plane detector window were made of Mictron, and CBCC window was made of Mylar. Because of the low price, some of $SBCC$ and $S_{1/2}BCC$ window newly prepared for the later experiment E393 was made of Mylar.

Detector window cannot support the gas pressure with itself. In order to support the window film, thin metal net was used. The used metal nets are written in Tab.5 and Tab.6.

In order to make a parallel electric field starting from the entrance window towards the anodes, windows must be electrically conductive. For such purposes, aluminum coating is widely used. However the aluminum coating was difficult to perform on large windows. Instead of the aluminum coating, carbon splay (Acheson Aerodag G) was used to make thin carbon coat on the windows. It was very useful to make conductive window quickly.

	$S_{1/2}BCC1$ 30°,50°	$SBCC1$ 90°-150°	$S_{1/2}BCC2$ 210°,230°	$SBCC2$ 270°-330°	$CBCC$
Window Material	$1.8\mu m$ Mictron				$2.14\mu m$ Mylar
Window Support	Tungsten $\phi 50\mu m$ 30 mesh/inch				SUS $\phi 50\mu m$ 50 mesh/inch
Window Coat	Micron-Sized Graphite (Acheson Aerodag G)				
Total Thickness	0.337 (mg/cm^2)				0.472 (mg/cm^2)
Shaper Electrode	t 1mm SUS				t 0.3/0.5mm SUS
Frisch Grid	SUS $50\mu m$ 2mm pitch Etching mesh				
Anode	t 1mm SUS				t 0.5mm SUS
Total Resistance	$15M\Omega$				$23.5M\Omega$

Table 5: BCC construction parameters used in E337

The total window thickness containing the carbon coat are also written in Tab.5 and Tab.6.

Inner Electrodes There are anode, Frisch grid, and field shaping electrodes in a BCC. Anode was made of a simple stainless plate. It is located for collecting drifted electrons. The anodes were electrically connected to the output port of the BCC.

Inner electric field was formed by the field shaping electrodes and the Frisch grid. Shaping electrodes were connected each others with registers. Geometrical shape of the electrodes are shown in Fig.17, Fig.19, and Fig.21. The distances and the resistances between the shaping electrodes were constant with exception of CBCC. They have half value at the front region of the CBCC inner electrodes. It is also shown in Fig.21.

Frisch grid was introduced in order to shield the electric fields. Frisch grid was located as the end panel of the shaping electrodes. Anode and Frisch grid was isolated with over $M\Omega$ resistance. Frisch grid was made of stainless etching mesh. The merit of using etching mesh is the low price comparing to the stretching wires.

Geometry Geometry of each BCC are shown in Fig.18, Fig.20, and Fig.22. $SBCC$ and $S_{1/2}BCC$ had fan shapes, and $CBCC$ had conical shape. Distance between the electrodes were selected to get the best resolution. Spacer used to locate the electrodes were made of Derlin. Polycarbonite biss were used to set the electrodes. All the components put into the gas volume had been cleaned with ultrasonic cleaner.

Resistance Resistances used between the shaping electrodes were selected in order to obtain stable bias supply considering the trigger rate. The resistance was determined as the largest value which can keep the stable electric fields with the resulting small current $\sim 50\mu A$.

2.3.2 37ch-BCC Array

E337 and E393 experimental setup were consisted by 37ch-BCC array. There were five BCCs with three type. As shown in Fig.18, $S_{1/2}BCC$ contained two BCC channels in a common gas volume. Two $S_{1/2}BCCs$ have been constructed as in-plane counters. $SBCC$ was another type of BCC for the in-plane counter. $SBCC$ was consisted by four BCC channels in the common gas volume just like $S_{1/2}BCC$. Fig.20 shows the design of the $SBCC$. Two $SBCCs$ have been constructed. As shown in Fig.25, in-plane counters were consisted by the two $SBCCs$ and two $S_{1/2}BCCs$. They were located in a common horizontal plane which included the target. Each BCC channels in $SBCC$ and $S_{1/2}BCC$ were located at the angular step of 20°. They had exactly same solid angles. Detailed construction parameters are written in Tab.5 and Tab.6.

	$S_{1/2}BCC1$ 30°,50°	$SBCC1$ 90°-150°	$S_{1/2}BCC2$ 210°,230°	$SBCC2$ 270°-330°	$CBCC$
Window Material	1.8μm Mictron		2.14μm Mylar		2.14 μm Mylar
Window Support	Tungsten $\phi 50\mu m$ 30 mesh/inch		SUS $\phi 50\mu m$ 50 mesh/inch		
Window Coat	Micron-Sized Graphite (Acheson Aerodag G)				
Total Thickness	0.337 (mg/cm^2)		0.472 (mg/cm^2)		
Shaper Electrode	t 1mm SUS				t 0.3/0.5mm SUS
Frisch Grid	SUS 50μm 2mm pitch Etching mesh				
Anode	t 1mm SUS				t 0.5mm SUS
Total Resistance	15$M\Omega$				23.5$M\Omega$

Table 6: BCC construction parameters used in E393

	$S_{1/2}BCC$	$SBCC$	$CBCC$ (Center-,Mid-,Outer-Ring)
Angular Step (θ)	20°	20°	non., 45°, 22.5°
θ acceptance	±7.6°	±7.6°	±8°, ±9°, ±9°
Center ϕ angle	0°	0°	90°, 70°,49°
Solid Angle	73.52 msr	73.52 msr	61.1 msr, 61.3 msr, 62.5 msr

Table 7: Geometries of the BCCs

In order to get information about IMF-multiplicity and out-of plane correlation, large acceptance conical shape BCC was constructed. Design of the $CBCC$ is shown in Fig.22 and Fig.21. In order to obtain large solid acceptance, inner electrodes were designed as producing spheric-symmetrical electric field. $CBCC$ was consisted by 25 BCC channels enclosed in a common gas volume. Each channel has almost same but slightly different solid angles. The alignment of the 25 BCC channels is shown in Fig.22. Further construction parameters are written in Tab.5 and Tab.6.

$S_{1/2}BCC$ $S_{1/2}BCC$ was constructed as in-plane counter which had two BCC channels in one gas volume. $S_{1/2}BCC$ was consisted by the counter chamber, windows, shaper electrodes, Frisch grids and anodes. Each component is shown in Fig. 17. The angular step of the two BCC channels was 20°. Each channel had same solid angle 73.52msr. Angular acceptance were ±7.6°.

$SBCC$ $SBCC$ had four BCC channels in one gas volume as like as $S_{1/2}BCC$ as shown in Fig.19. Each BCC channel had same solid angle 73.52msr just same as $S_{1/2}BCC$. Other features were same as $S_{1/2}BCC$.

$CBCC$ $CBCC$ was a large acceptance conical shape detector. Inner electrodes shown in Fig.21 were set in the conical chamber. The electrodes were consisted by three layered rings named Center-Ring, Mid-Ring, and Outer-Ring. Each layer was divided into one, eight, sixteen channels, respectively. Their solid angles were 61.1msr,61.3msr,62.5msr respectively.

As shown in Fig.22, there were huge gas volume behind the anode plane in the gas chamber. It was designed for preparing future extensions. This gas volume could also make a signal on the anodes from the backward directions if there were gas ionization in any reason. In fact, setting CBCC on the beam line, a lot of back ground events due to beam halo penetrating the back anode gas region was observed. In order to reduce the back anode ionizing events, electric shielding was added before E393. The shielding electrodes were set behind the anodes with same bias voltage as the Frisch grid as shown in Fig.24. Using the shield electrodes, most of the back anode ionizing events were disappeared at least for α-source tests. Although the

CBCC upgrading, the backward ionizing events had not disappeared in E393. With all the existence of the backward events, they could be separated from real events in off-line analysis using Range and Energy information.

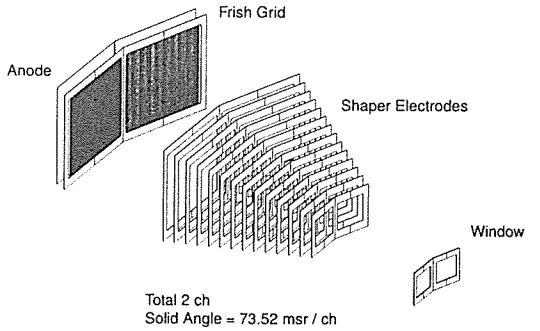

Figure 17: Inner electrodes of the $S_{1/2}BCC$

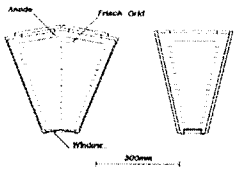

Figure 18: Geometry of the $S_{1/2}BCC$

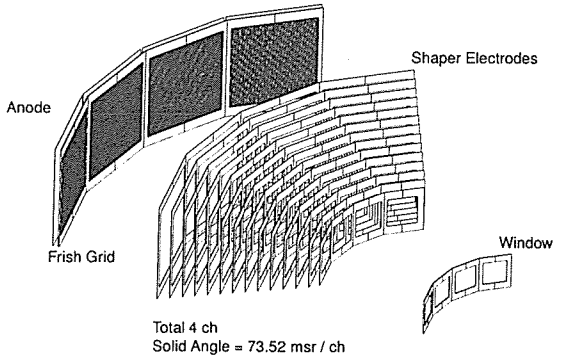

Figure 19: Inner electrodes of the $SBCC$

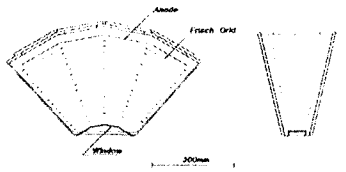

Figure 20: Geometry of the *SBCC*

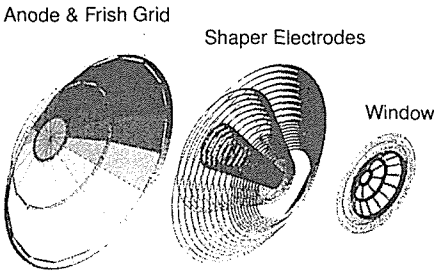

	Outer-Ring	*Mid-Ring*	*Center-Ring*
Total ch	16 ch	8 ch	1 ch
Center Angle	49 deg.	70 deg.	90 deg.
Solid Angle	62.5 msr	61.3 msr	61.1 msr

Figure 21: Inner electrodes of the *CBCC*

2.3.3 Front-end Electronics

Block diagram of the front-end electronics for E337 and E393 are shown in Fig.29 and Fig.30.

pre-amplifier The output signals from the BCC anode amplified in a charge-sensitive pre-amplifier. Typical cable length from the anode to the pre-amplifier was within $1m$. There are also pulser input in the pre-amplifier, which was used for a calibration using pulser signal.

Bragg **Signal** The output signals from the pre-amplifier were sent from the experimental area to the control room. Here they were split into two main amplifiers with different shaping time constants. In order to reconstruct the shape of the Bragg curve in the counter gas, shaper amplifier with small time constants about $0.1\mu sec$ were used. The small timing constant was determined as typical timing constant of the counter response. The peak value of the output signals from the shaping amplifiers with the fast timing constant gives the Bragg peak information (*Bragg*). The Bragg peak signals were fed into peak-sensitive ADCs. To adjust the peak position timing in the ADC gate, they were delayed before putting into ADC.

Range **Information** The range in the counter gas could also be determined using the same output signals. Time difference of the leading edge and trailing edge gave the range information (*Range*). The *Bragg* signal was fed into a pulse-width analyzer (PWA) with a low threshold

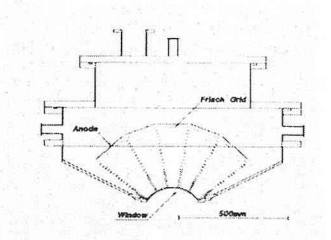

Figure 22: Geometry of the *CBCC*

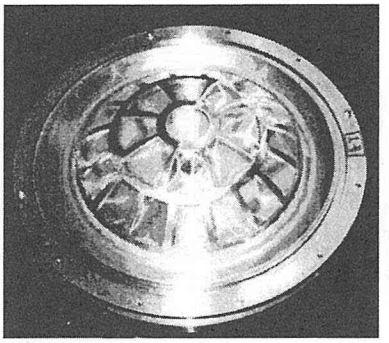

Figure 23: Picture of the *CBCC* window.

(Low V_{th}) and high threshold (High V_{th}). The pulse width analyzer generates a pair of timing pulses at the leading (*Start*) and trailing (*Stop*) edges of the *Bragg* signal with low threshold V_{th}. The timing differences between the two signals were read with TDCs. The pulse generated from the high threshold was used as a raw trigger signal of the corresponding BCC channel. They were fed into a coincidence register in order to recognize coincidence channels. The high threshold V_{th} was tuned to select those events with high *Bragg* signals corresponding to $Z \geq 3$ or 2 in order to reduce trigger rate rejecting light charged particles.

Energy **Signal** *Energy* information was obtained from the output signal of shaper amplifier with long timing constant of about $6\mu sec$. The long time constant is almost corresponding to the maximum timing range of the *Bragg* signal. The *Energy* signals were directly fed into the peak-sensitive ADCs.

2.3.4 Read-out system

Block diagram of the read-out system for E337 and E393 are shown in Fig.31 and Fig.32.

CAMAC crate & ACC Read-out system was constructed as a CAMAC base system. All the ADCs and TDCs were placed in one main crate where an ACC read out data from them. The ACC had 1 Mbytes of the main memory used for data buffer and program area. An interrupt

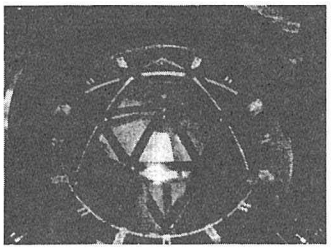

Figure 24: Shielding electrodes set behind the CBCC anodes (for E393).

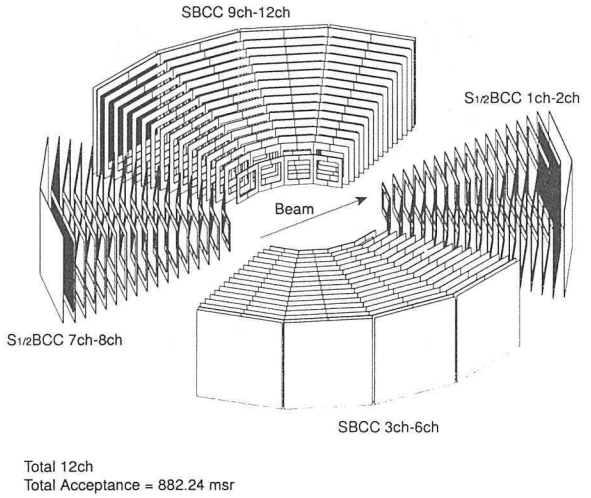

Figure 25: Setup of in-plane counters. Only inner electrodes are drawn.

register was used for interrupting to the ACC when a main event trigger, a pulser event trigger for a calibration, or a beam spill end timing trigger were detected.

Trigger The main event trigger was made as OR of all the raw trigger signals from the 37ch-BCC array. Once a main trigger interrupted the ACC, it would be inhibited with a flip-flop until all the data were collected by the computer. After the end of the data collecting cycle, the flip-fop would be cleared by a reset signal. Gate signals for the coincidence register and the ADCs were formed from the main trigger signal.

The pulser event trigger was formed by additional front-end electronics. The pulser events were generated at the spill off timing in order to check the timing drift of the electronics.

A beam spill end timing trigger was provided from the accelerator. It was used to interrupt the data collection and start sending the collected data from the ACC to the host computer.

Coincidence Register All the raw trigger signals generated from each BCC channel were fed into the coincidence register. A 16-bit 48ch coincidence register was used. Once a main event trigger were accepted by the ACC, bit pattern which had been hit within the coincident gate timing

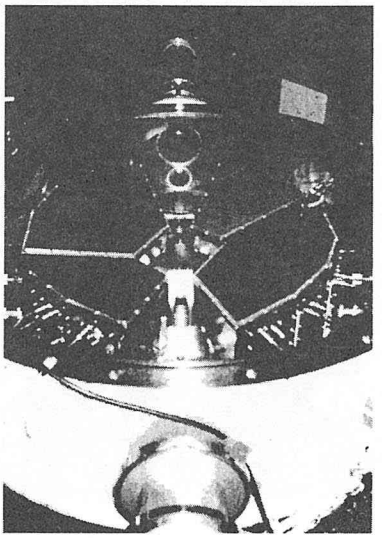

Figure 26: Setup of in-plane counters (E337).

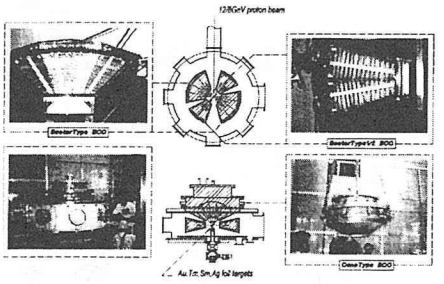

Figure 27: Full experimental setup for the E337 and E393.

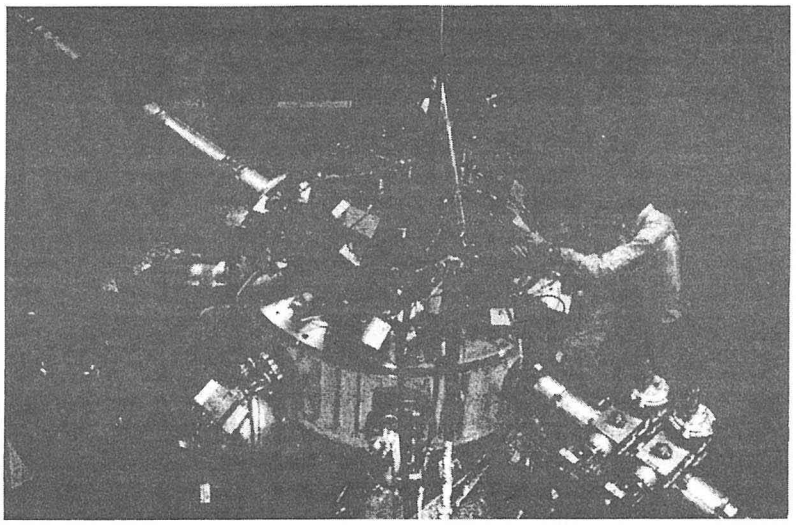

Figure 28: Overview of the experimental setup at EP1B line.

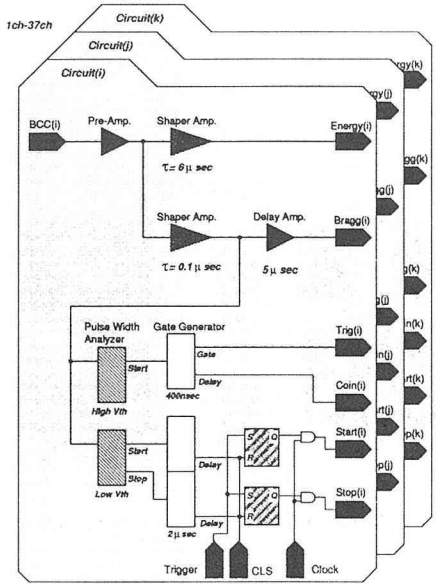

Figure 29: Block diagram of the front-end electronics for E337

of the coincidence register were read. The ACC judge the hit channel and start to read the corresponding ADCs and TDCs.

Peak Sensitive ADC Three modules of 12-bit successive approximation type ADCs with 16-channel inputs and eight modules of the 12bit Wilkinson type ADCs with 4-channel inputs were used for read the *Energy* and *Bragg* signals. Because of the high linearity requirement for the *Bragg* signal in order to make charge separation, Wilkinson type ADCs were used for reading *Bragg* signals. Common ADC gates were used for both *Bragg* and *Energy*.

Timing Counting Scaler In order to count the timing information over μsec, clock counting system was constructed in E337. Scaler counts the pulse numbers corresponding to the timing range. The timing distance from the main trigger to the *Start* and *Stop* signal for each hitting channel had been determined using the clock system. AND outputs of $40MHz$ pulser and a gate started from the main trigger to the *Start* or *Stop* signal were put into the CAMAC scaler. The *Start* counts and *Stop* counts were used to determine the hitting timing and counting the *Range*.

Crock Based TDC To reduce the huge numbers of the electronic modules for the timing counting system used for E337, custom made 100 MHz CAMAC clock-based TDC module with 16-channel fast NIM level inputs had been developed using 5 programmable logic devices for E393 [127]. Four devices were configured as 4 channels of counter chips, and the other one was configured as a controller chip of the counters, input signals and CAMAC interface.

The TDC had a 100MHz internal clock generated by a crystal oscillator that allows the interval time of *Start* and *Stop* signals to be measured to $10nsec$ precision. It also had a NIM external clock input for feeding the variable clock.

Output Register An output register generated a reset signal to the coincidence register, the TDCs, and the flip-flop when the ACC had finished one acquisition cycle.

PC A crate controller (Kinetics 3922) in the main crate communicates with the data-acquisition system of the PC via a K-Bus cable and a PCI interface card (Kinetics 2915) for E393 [127]. For E337, the crate controller was connected with VME onboad computer SPARC (SUN 5CE) instead of PC via VME K-Bus interface card (Kinetics 2917) [128]. A collector program was running on the host computers.

2.4 E337 Experiment

E337 data taking was performed at EP1B line from April 1996 to March 1996. 12GeV proton beam with four targets (gold, thulium, samarium, silver) were used. The additional run for background event estimation using empty targets were taken alternately with the usual data taking runs. Run parameters are listed in Tab.8. All the data taking was performed with usual P10-Gas operation mode (200 Torr). Data acquisition system was based on the CAMAC-VME system [128].

2.5 E393 Experiment

The second experiment using 8GeV protons are performed at KEK-PS P1 beam line from October 1997 to December 1997. Background runs were taken alternatively with the event runs as same as in E337. To reduce the background data taking time, one background run was shared with two different targets event run for the background event subtraction in the off-line analysis. Null target, gold and silver targets runs were performed alternately, and Mylar target and samarium target runs were

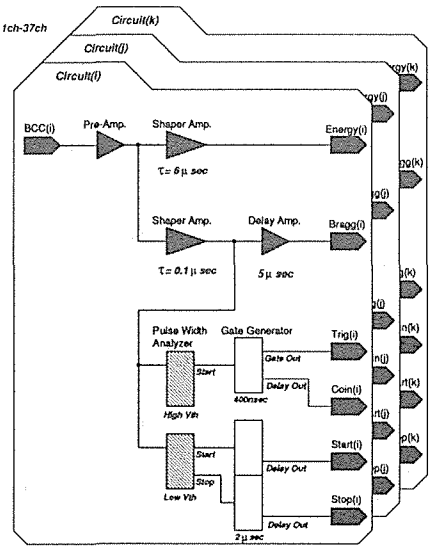

Figure 30: Block diagram of the front-end electronics for E393

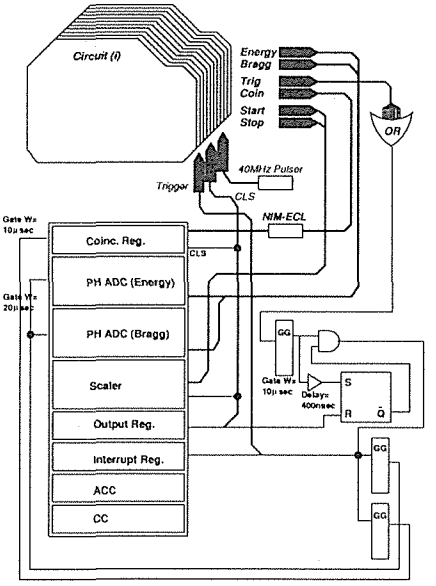

Figure 31: Read-out electronics for E337

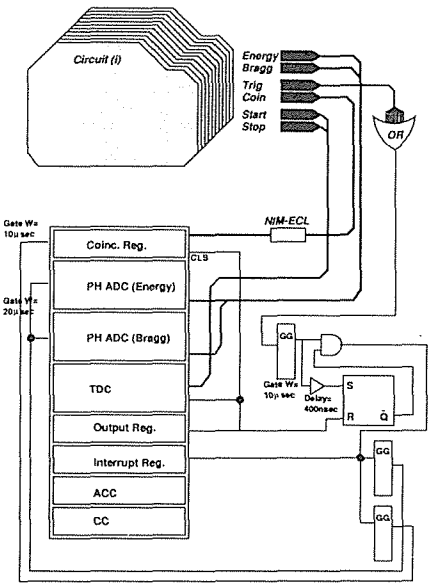

Figure 32: Read-out electronics for E393

	Au	Tm	Sm	Ag
Total p	3.4×10^{14}	2.0×10^{14}	1.8×10^{14}	1.1×10^{14}
Total p for event run	2.3×10^{14}	1.5×10^{14}	1.3×10^{14}	4.2×10^{13}
Total p for background run	1.1×10^{14}	5.2×10^{13}	5.3×10^{13}	7.2×10^{13}
Total Real Trigger	93.2 M	79.7 M	87.7 M	56.5 M
Real Trigger for event run	80.4 M	67.2 M	78.9 M	37.1 M
Real Trigger for background run	12.9 M	12.5 M	8.78 M	19.4 M
Total Accepted Trigger	75.0 M	61.9 M	60.0 M	34.5 M
Accepted Trigger for event run	63.2 M	51.2 M	52.3 M	19.8 M
Accepted Trigger for background run	11.8 M	10.6 M	7.71 M	14.7 M
Total Live Time	80.4 %	77.7 %	68.5 %	61.0 %
Live Time in event run	78.6 %	76.3 %	66.3 %	53.3 %
Live Time in background run	91.4 %	85.2 %	87.8 %	75.9 %
Trigger Condition	$Z_{IMF} \geq 3$	$Z_{IMF} \geq 3$	$Z_{IMF} \geq 3$	$Z_{IMF} \geq 2$

Table 8: Run summary for E337

	Au	Sm	Ag	Null	Mylar
Total p	3.1×10^{14}	5.5×10^{14}	5.9×10^{14}	2.3×10^{14}	2.1×10^{14}
Total Real Trigger	124 M	147 M	161 M	46.0 M	45.7 M
Total Accepted Trigger	86.3 M	104 M	117 M	36.3 M	34.3 M
Total Live Time	69.5 %	70.8 %	73.1 %	79.0 %	75.0 %
Trigger Condition	$Z_{IMF} \geq 3$	$Z_{IMF} \geq 3$	$Z_{IMF} \geq 3$	$Z_{IMF} \geq 3$	$Z_{IMF} \geq 3$

Table 9: Run summary for E393

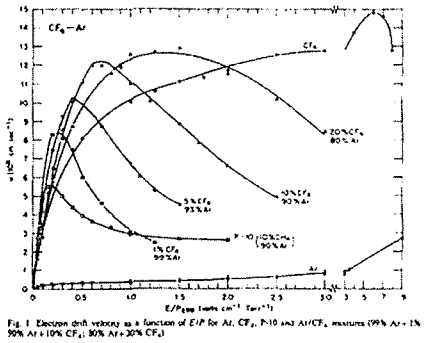

Figure 33: Measured drift velocities for various gas.
Reported in [129]. Drift velocities for P10 gas and CF_4 gas are also shown.

performed alternately. For E393 experiment, additional runs using CF_4-gas operational mode for the BCC was performed in order to obtain high energy fragments. In addition, CBCC was modified for reducing background events as mentioned before. Data acquisition system was modified to the CAMAC-PC based system [127].

3 Operation and Analysis of the Bragg Curve Counter

3.1 Operation Mode of BCC

In the past experiments using the BCCs, P10 gas (90% argon + 10% methane) was used as a standard counter gas because of its nearly constant and maximum drift velocity around the operation bias region ($\sim 0.2 V cm^{-1} Torr^{-1}$). It is shown in Fig.33 [129]. The gas pressure was selected as suitable for detecting IMFs emitted in the multi-fragmentation reactions. It means that the peak region of the Maxwell-Boltzmann shaped energy spectra should be detected. However, such condition is not suitable for detecting light fragments as Li or Be. The stopping power of the standard operation mode is too small for detecting the peak region of the energy spectra for such light fragments.

The possibility of the isotope separation for Li and Be fragments were found in the beam time of

the E337 data taking. Thus all the Li and Be isotope data, which is used for the isotope temperature analysis, was taken in the standard P10 gas operation mode.

The very narrow kinetic energy dynamic range for the light fragments caused difficulty on evaluating isotope yield in the isotope temperature analysis. In order to enlarge the dynamic range, some trial R&D was studied.

- Adding plastic scintillation counters after the BCC anodes for stopping high energy fragments.
- Adding degrader before the BCC entrances.
- Performing additional experimental runs with high pressure and high density gas.

The first trial is the best way if they are possible because the high energy fragments can be detected in the same run with low energy fragments without any operation mode changing. A prototype of a scinti-BCC was constructed and tested using 12 GeV proton with Au target at EP1B line. As a result, because of the very high single trigger rate for the scintillation counter due to the beam halo, it was impossible to identify which signal of the scintillation counter was corresponding to the BCC signal.

Simulation studies were performed for the second idea of using degrader. As a result, dispersion of the energy is expected to be too large for getting the shape information of the spectra.

The last idea is the most simple one but in this case high energy fragments can not be detected at the same time with the low energy fragments. This implies that the energy spectra of the high IMF-multiplicity events can not be combined to the results of the standard operation mode. With all the defect, performing additional experimental run using high pressure and high density gas was decided. Additional mode was performed with 300 Torr using CF_4 gas in addition to the statndard mode with 200 Torr using P10 gas.

3.2 Particle Identification using BCC

3.2.1 Z Separation

Z Separation for IMFs ($3 \leq Z_{IMF} \leq 25$) was performed in $Bragg$ vs. $Range$ plot. The locus shape can be described using empirical Fermi-function like functional form as below,

$$Bragg = \frac{p1 + p4 \cdot Range}{1 + p2 \cdot exp(-p3 \cdot Range)} \tag{2}$$

with four locus shape parameters $p1, p2, p3, p4$. $p1$ is a quantity which is roughly proportional to Z. $p2$ and $p3$ are parameters to determine the curvature in the small $Range$ region. $p4$ is a slope parameter in large $Range$ region where the corresponding locus can be recognized as a simple straight line.

Locus fitting using Eq.2 has been performed for each locus corresponding to $3 \leq Z_{IMF} \leq 25$ (Fig.34). The Z dependence of the fitted shape parameters are shown in Fig.35. The solid lines show the results of empirical function fitting using Eq.3.

$$\begin{aligned} p1(Z) &= a0 + a1 \cdot Z \\ p2(Z) &= b0 + b1 \cdot Z + b2 \cdot Z^2 \\ p3(Z) &= c0 + c1 \cdot Z + c2 \cdot Z^2 \\ p4(Z) &= d0 + d1 \cdot Z \end{aligned} \tag{3}$$

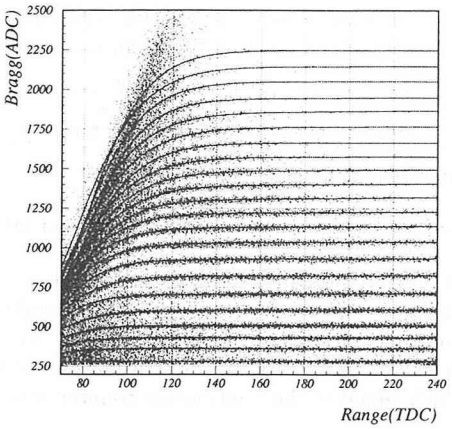

Figure 34: Results of locus fitting on *Bragg* vs. *Range* plot using the empirical function.

As shown in Fig.35, the charge parameter $p1$ is nearly proportional to Z. It means that the parameter $p1$ can be a measure of the charge Z in the Z definition procedure. It means that the locus identification can be performed using only one parameter $p1$. The charge parameter $p1$ is treated as PID function in the following discussion. PID can be written using the parameters $p2, p3, p4$ as a function of $Bragg$ and $Range$.

$$\begin{aligned} PID &= p1 \\ &= Bragg \cdot \{1 + p2(Bragg) \cdot exp[-p3(Bragg) \cdot Range] - p4(Bragg) \cdot Range\} \end{aligned} \tag{4}$$

Strictly speaking, $p2, p3$ and $p4$ are not functions of $Bragg$ but of corresponding Z. However, Z cannot be used in the calculation because experimental measurement was $Bragg$. Considering the fact that Z can be treated as a linear function of $Bragg$,

$$\begin{aligned} Z &\approx \alpha 0 + \alpha 1 \cdot Bragg \\ &(\alpha 0, \alpha 1; paramters) \end{aligned} \tag{5}$$

$p2, p3$ and $p4$ could be roughly treated as functions of $Bragg$. Therefore, PID function can be described as Eq.4 with

$$\begin{aligned} p1(Bragg) &= A0 + A1 \cdot Bragg \\ p2(Bragg) &= B0 + B1 \cdot Bragg + B2 \cdot Bragg^2 \\ p3(Bragg) &= C0 + C1 \cdot Bragg + C2 \cdot Bragg^2 \\ p4(Bragg) &= D0 + D1 \cdot Bragg. \end{aligned} \tag{6}$$

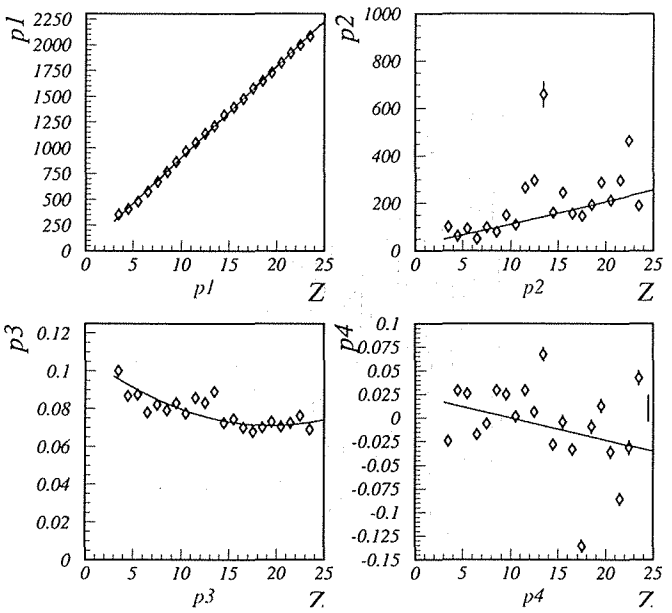

Figure 35: Z dependences of the locus shape parameters.

If we obtained the ten transformation parameters $A0, A1, B0, B1, B2, C0, C1, C2, D0$, and $D1$, PID function could be obtained from *Bragg* and *Range*. Eq.6 means the transformation between (PID,*Range*) and (*Bragg*,*Range*). Considering the relation of Eq.5, Z can be defined using only one dimensional quantity PID in the transformed results.

In order to obtain the ten transforming parameters, we don't have to make locus shape fitting for all the loci $3 \leq Z_{IMF} \leq 25$ using Eq.2. It is sufficient to fit only three loci in order to get twelve unknown parameters. It is very important that we can make Z definition for all the Z_{IMF} without fitting each loci as be performed in the past BCC analysis. The development of this Z definition technique made great improvement on the BCC-off-line analysis.

Once at least three loci are performed the shape parameter fitting, the transforming parameters can be obtained. Then PID function can be calculated. Fig.36 shows the transformed results of PID spectra. IMFs can be separated with PID resolution about 11.3σ for light IMFs and 2.8σ for heavy IMFs. Although locus identification for heavy IMFs are difficult because of their poor statics, they can be separated in the PID spectra.

The effect of the PID transformation can be clearly seen in Fig.37 and Fig.38. It is hard to make reproductive Z separation in two-dimensional plot of Fig.38, on the other hand, Z separation using the one dimensional PID spectra is very simple.

The Z separation technique written above can be used as a standard BCC-off-line analysis procedure.

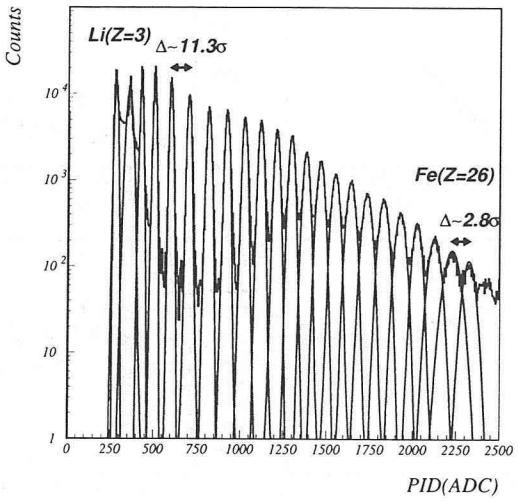

Figure 36: One dimensional PID spectrum.

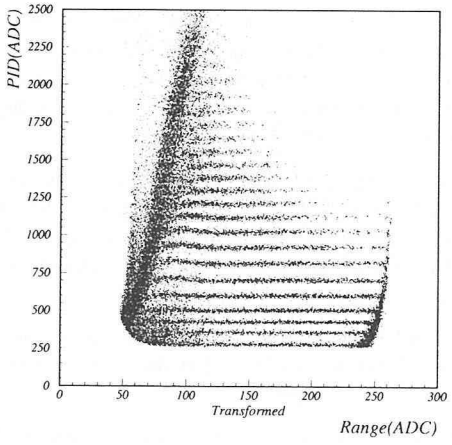

Figure 37: PID vs. $Range$ plot (After Transformation).

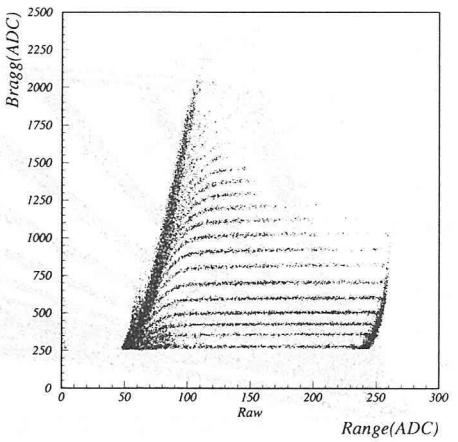

Figure 38: *Bragg* vs. *Range* plot (Before Transformation).

3.2.2 Isotope Separation for *Li* and *Be*

Locus splitting for light IMFs was observed according to their mass differences. The mass splitting can be confirmed especially in *Range* vs. *Energy* plot. They are most clearly separated in this plot comparing to other plots as *Bragg* vs. *Energy* plot. Because the *Bragg* resolution for the mass difference is not sufficient to make isotope separation, mass separation procedure is developed using the *Range* vs. *Energy* plot.

Isotope cut is determined as a quadratic function between *Range* and *Energy*. The expected border of the isotope cut is set as below.

$$Range = c0 + c1 \cdot Energy + c2 \cdot Energy^2 \tag{7}$$

Here $c0, c1$ and $c2$ are cutting parameters corresponding to each border function. The functional form written in Eq.7 is not trivial. General relation between range and kinetic energy is

$$Range \propto Energy^{1.73}, \tag{8}$$

however, the experimental results fit with Eq.7 better than with Eq.8. In order to fix the cutting line, cutting points are determined at first. The cutting curve is obtained as a fitting curve of the cutting points.

Loci are sliced on the *Range* vs. *Energy* plot as the dotted line in Fig39 for lithium and beryllium fragments. The same slice procedure was also performed for boron locus, however, the mass resolution was not sufficient to make isotope separation. Therefore, the isotope separation was performed only for lithium and beryllium isotopes. Sliced data points are projected into the parallel direction to the tangent line of the corresponding loci. Fig.40 shows the typical spectra of the sliced data. The horizontal axis implies the perpendicular direction to the projecting direction.

Cutting points are determined in the sliced spectra. Gaussian fitting is performed to each mass peak in the sliced spectra. The Gaussian width is fixed to be common in the isotopes. Cutting points

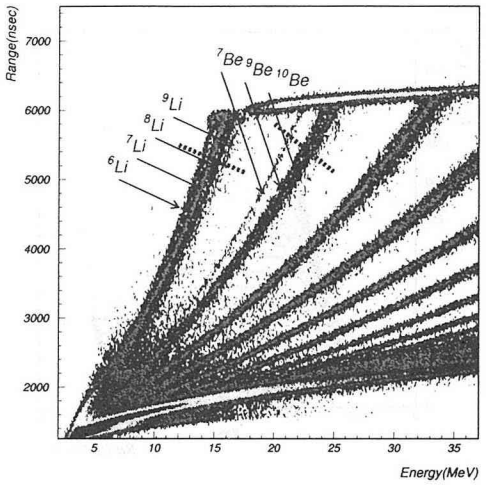

Figure 39: Isotope separation in *Range* vs. *Energy* plot.

are determined using the fitted Gaussian functions. They are determined to divide the spectra in order to keep the area ratio between peaks side by side.

$$\int_{x_0}^{\infty} f_1(x)dx + \int_{x_0}^{\infty} f_2(x)dx : \int_{-\infty}^{x_0} f_1(x)dx + \int_{-\infty}^{x_0} f_2(x)dx$$
$$= \int_{-\infty}^{\infty} f_1(x)dx : \int_{-\infty}^{\infty} f_2(x)dx \tag{9}$$

Here x_0 is the dividing point in the sliced spectra. The variable x is the horizontal axis of the same spectra. $f1(x)$ and $f2(x)$ is the fitted Gaussian functions corresponding to the isotope peaks to be divided. The cutting points x_0 is obtained as numerical solutions of Eq.9 for each sliced spectra. The cutting points are transformed into (*Range*,*Energy*), then cutting curve fitting is performed using Eq.7.

3.3 Energy Calibration

Energy calibration is performed using the turning point at the high energy region of the fragment loci. The events observed at the turning point are assumed to be the stopped event just at the anode position. Therefore the corresponding energy can be obtained by a energy loss calculation. More than five turning points are determined for each channel data. The turning point is determined as the crossing point of the locus fitted lines shown in Fig.42. Each lines are fitted to the locus using linear function and quadratic function respectively.

Obtained turning points are used for fitting the conversion function.

$$E(MeV) = aE(ADC) + b \tag{10}$$

Using the obtained turning points and the zero point obtained by the pulser events, conversion factors are determined for each BCC channel.

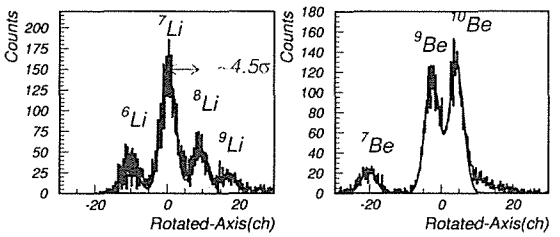

Figure 40: Isotope separation in the spectra obtained by the sliced data.

4 Energy Spectra

4.1 Fragment Energy Spectra

Energy spectra of the each fragments are obtained after charge separation or isotope separation. Energy calibrations are performed as mentioned in Sec.3. Influence of the energy loss in the target foil and entrance windows of the detectors are corrected. Run-by-run background subtractions are performed considering the timing drift of the beam profile and detector gain. Then the obtained energy spectra will be examined with the models.

One example of the obtained fragment energy spectra are shown in Fig.43. The obtained energy spectra have thier shapes of Maxwell-Boltzmann distribution. It implies that the fragmentation process may be occurred in a kind of thermal equilibrated system. These fragment energy spectra can be roughly understood by a thermal moving source model. Particle emission from a thermal equilibrated source should be isotropic, however, observed energy spectra show an obvious sideward yield enhancement, which implies the existence of anisotropic emission. Therefore, simple isotropic moving source model under estimate the fragment yield observed at the sideward directions. In the following sections, some types of fitting models are briefly reviewed.

4.2 Thermal Moving Source Model Fitting

4.3 Functional Forms of Fragment Kinetic Energy Spectra

Functional form of moving source model written as following have been widely used to fit the fragment kinetic energy spectra in intermediate energy multifragmentation experiments.

$$\frac{d^2\sigma}{dEd\Omega} = N\sqrt{E/E^*}(E^* - B)^{1/2}exp(\frac{-(E^* - B)}{T}) \quad (11)$$

$$E^* = E + \frac{1}{2}M_f\beta^2 - 2\sqrt{E\frac{1}{2}M_f\beta^2}cos\theta \quad (12)$$

Here β is velocity of moving source. B is Coulomb energy shift. E^* is kinetic energy in the rest frame. T is the slope temperature parameter. Eq.12 can be obtained transforming to laboratory system from isotropic energy distribution on the rest frame.

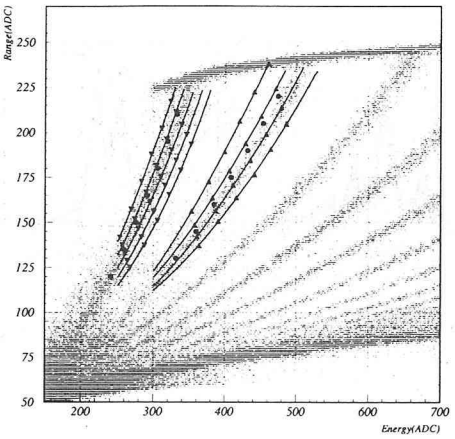

Figure 41: Example of the obtained cutting points (triangle points) and curves (solid line). Large filled circle points are the points corresponding to $x = 0$ points in the each sliced spectrum.

$$\frac{d^2\sigma^*}{dE^* d\Omega^*} = N\sqrt{E^* - B}exp(-\frac{E^* - B}{T}) \tag{13}$$

In order to reproduce low energy tail of the energy spectra, Coulomb shift B should not be constant for all the fragments. B should depend on where the fragments are formed. Once an relation between B and fragment forming point are assumed, resulting energy spectra can be obtained by integrating Eq.12 over B [18]. However, the calculation of the integral is so complicated that it is hard to fit energy spectra. To reduce the computation, phenomenological functional form is used.

$$\frac{d^2\sigma^*}{dE^* d\Omega^*} = N\sqrt{E^*}exp(\frac{-E^*}{T})\frac{1}{exp[\frac{2\pi(B-E^*)}{B_c}] + 1} \tag{14}$$

Here B_c is a variance of the B distribution which is introduced in order to reproduce similar functional forms as that of integrated function over B. Eq.14 can reproduce the effect of the Coulomb shift variance. Obtained energy spectra can well expressed using this functional form. The aim of this modification is to reproduce obtained energy spectra using simple functional form without integral in the function. Thus there are no difference on the treatment of angular distribution between original formula and the simple formula written in Eq.14.

4.4 Single Moving Source Model

Differential cross section on the laboratory system should be obtained. It can be obtained by transforming Eq.14 into laboratory system.

$$\frac{d^2\sigma}{dEd\Omega} = N\sqrt{E}exp(-\frac{E^*}{T})\frac{1}{exp[\frac{2\pi(B-E^*)}{B_c}] + 1} \tag{15}$$

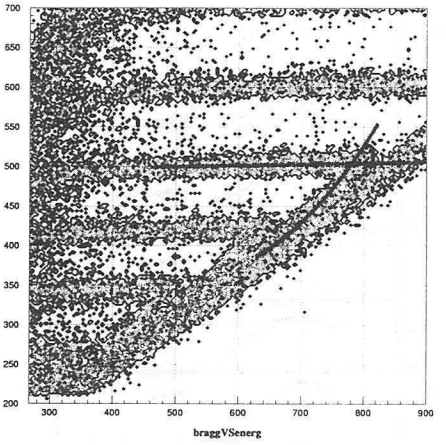

Figure 42: Determination of the turning point for the energy calibration.

$$E^* = E + \frac{1}{2}M_f\beta^2 - 2\sqrt{E\frac{1}{2}M_f\beta^2 cos\theta} \tag{16}$$

This formation based on isotropic fragment emission, therefore, resultant angular distribution at laboratory system should show forward peaking angular distribution. Fig.44 shows an example of the function. Concentric circles can be found around the moving source center in the contour plot of the Lorentz invariant cross section.

$$\frac{1}{p}\frac{d^2\sigma}{dEd\Omega} = \frac{1}{\sqrt{(E-M_f)^2 - M_f^2}} N\sqrt{E}exp(-\frac{E^*}{T})\frac{1}{exp[\frac{2\pi(B-E^*)}{B_c}]+1} \tag{17}$$

The moving source center is plotted as a triangle point in Fig.44. As shown in Fig.44, fragment emission probability should have uniform angular distribution around the moving source frame. This means that forward peaking angular distribution might be obtained in the laboratory frame because of the source moving.

4.5 Two Moving Source Model

The most simple modification on the single moving source model is to put another moving source component. Trying to fit the energy spectra using two or three moving source have been widely studied. This framework can reproduce those energy spectra which have two or three component corresponding to different fragment production stage. Two moving source model can be simply written as following;

$$\frac{d^2\sigma}{dEd\Omega} = N_1\sqrt{E}exp(-\frac{E^*}{T_1})\frac{1}{exp[\frac{2\pi(B_1-E^*)}{B_{c1}}]+1} + N_2\sqrt{E}exp(-\frac{E^*}{T_2})\frac{1}{exp[\frac{2\pi(B_2-E^*)}{B_{c2}}]+1}. \tag{18}$$

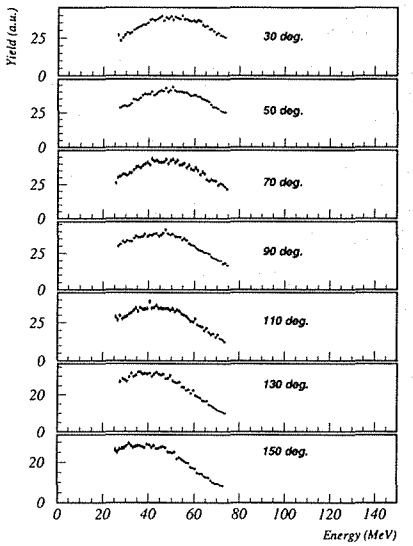

Figure 43: Typical fragment energy spectra. Inclusive energy spectra of F fragment produced in 12GeV p + Au reactions are shown as functions of detected inplane angles.

Both of the component makes isotropic IMF emission. Although, it is not self-evident that their sum produce the isotropic IMF emission. Generally, for a sum of the single moving sources can written as following.

$$\frac{d^2\sigma}{dEd\Omega} = \sum_i N_i \sqrt{E} exp(\frac{E^*}{T_i}) \frac{1}{exp[\frac{2\pi(B_i - E^*)}{B_{ci}}] + 1} \tag{19}$$

The transformation between E and E^* is depending on the source velocity β_i. Therefore if the β_i were different between each i-th source, the total differential cross section in the Lab. frame could have a complex angular distribution. Possibility of the two moving source model fitting have been examined. One example of the resultant cross section using two moving source model is shown in Fig.45. The resultant shape depends on the balance between the two source. Whether this model works well or not for reproducing the sideward enhancement is not easy to understand. This problem will be discussed in the following section.

4.6 Sideward Flow Model

In order to explain the energy spectra quantitatively including the side-ward angles, a model with collective flow is attempted to study. All the fragments are considered to have optional flow momentum component p_f in addition to the isotropic thermal momentum p.

$$(E^* + M_f)^2 = M_f^2 + p^{*2} \tag{20}$$

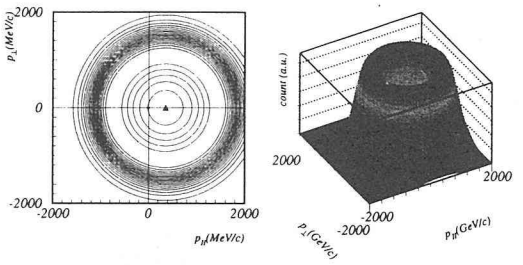

Figure 44: Contour plot of Lorentz invariant cross section for a example of single moving source model.

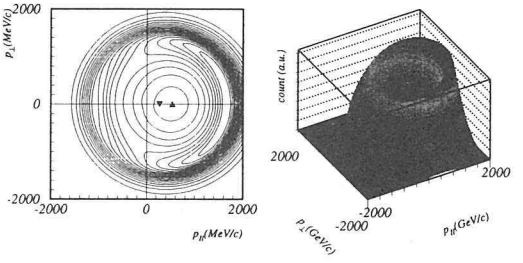

Figure 45: One example of the resulting cross section using two moving source model.

$$\begin{aligned} p_x^* &= p_x = 0 \\ p_y^* &= p_y \\ p_z^* &= -\gamma\beta(E + M_f) + \gamma p_z \end{aligned} \tag{21}$$

In order to add the flow component, fragment momentum should be shifted in the cross section formula Eq.14 for a single moving source model.

$$(p_x^*, p_y^*, p_z^*) \rightarrow (p_x^* - p_{fx}^*, p_y^* - p_{fy}^*, p_z^* - p_{fz}^*) \tag{22}$$

where flow momentum component $p_{fx}^*, p_{fy}^*, p_{fz}^*$ are

$$p_{xy}^* = 0, p_{fy}^* = p_f sin\theta_f, p_{fz}^* = p_f cos\theta_f \tag{23}$$

E, θ in the Lab. system can be written using he total Lab. momentum component (p_x, p_y, p_z) as following,

$$p_x = 0; p_y = psin\theta; p_z = pcos\theta \tag{24}$$

$$p = \sqrt{(E + M_f)^2 - M_f^2} \tag{25}$$

Then we can estimate the differential cross section $d^2\sigma/dEd\Omega$ in the Lab. system substituting Eq.20 with Eq.25 into Eq.15. An typical example of the resultant Lorentz invariant cross section using the flow moving source model is shown in Fig.46. In Fig.46, small arrows are shown which are corresponding to the flow momentum. All the cross sections are shifted from the center of moving source to the flow direction. As a result, fragment yield might be enhance in the flow direction, however, the resultant energy spectra might also shift towards high energy side because of the flow momentum.

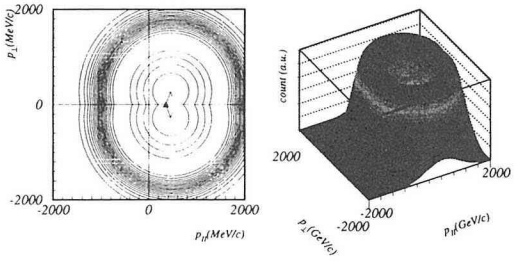

Figure 46: One example of the resulting cross section using the flow moving source model.

4.7 Deformed Moving Source Model

In order to get phenomenological formation which can successfully reproduce the fragment energy spectra including sideward enhancement, deformed moving source model is introduced. Instead of the constant normalization factor N in the single moving source model, anisotropic normalization factor is introduced. On the moving source system, resultant cross section can be expressed as following;

$$\frac{d^2\sigma^*}{dE^*d\Omega^*} = N(\theta^*)\sqrt{E^*}exp(\frac{-E^*}{T})\frac{1}{exp[\frac{2\pi(B-E^*)}{B_c}]+1} \tag{26}$$

where the modified normalization factor $N(\theta^*)$ can be expressed as a function of the emission angle on the rest frame;

$$N(\theta^*) = N_0 + N_f exp[-\frac{(\theta^*-\theta_f^*)^2}{2\sigma_f^{*2}}]. \tag{27}$$

The transformation between laboratory angle θ and that on the rest frame θ^* can be expressed as following.

$$\theta^* = cos^{-1}\left(\gamma\frac{p}{p^*}\cos\theta - \gamma\beta\frac{\sqrt{M_f^2+p^2}}{p^*}\right) \tag{28}$$

The additional normalization deforming factor have a Gaussian functional form in this formalism. It is not introduced inevitably, but only phenomenologically. An example using the deformed moving source model is shown in Fig.47. There can be found a strong sideward enhancement towards the direction corresponding to θ_f^*. As shown in Fig.47, there are no energy shift towards the sideward

	Single MS	Single MS (all)	Two MS	MS with Flow	Deformed MS
χ^2/n	12.41	6.45	5.99	5.24	1.40

Table 10: Reduced χ^2 for the fitting results on the energy spectra of F fragments produced in 12GeV p + Au reaction.

direction. This is the main difference from the results of the flow moving source model. Although the interpretation of this model is unclear, the deformed moving source model can reproduce the sideward yield enhancement without changing the shape of the energy spectra.

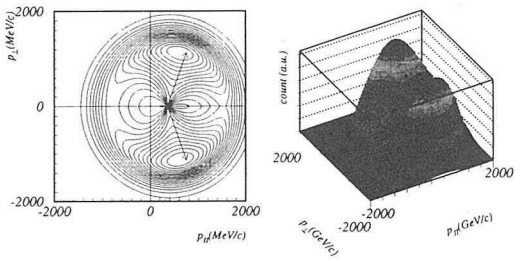

Figure 47: Example of Lorentz invariant cross section resulting using the deformed moving source model.

4.8 Fitting Results

Energy spectra fittings are performed using each fitting model. Here fitting results for F fragment produce in 12GeV p + Au reaction are shown as typical examples.

Fitting results of the single moving source model (Fig.48, 49) underestimate for the side-ward directions. Fig.49 shows a result on the fitting for all angles from $\theta = 30°$ to 150°, and Fig.48 shows a result on the fitting only for $\theta = 30°$ and $\theta = 150°$. The reason why sideward angle have not included into the fitting procedure for the case of Fig.48 is that, this single moving source model cannot reproduce the sideward angles. This model can be applied for only isotropic data. Fig.49 is shown for a reference. Reduced χ^2 value for them are listed in Tab.10 as "Single MS" for the case of Fig.48 and Single MS (all) for the case of Fig.49. These χ^2/n values are obtained by the χ^2 calculation including all the angles. Thus, χ^2/n for the results of the fitting for only 30° and 150° has a large value because of the under estimation on the sideward region. Obtained Lorentz invariant cross section is also shown in Fig.50.

It can not significantly improved even using two moving source model as shown in Fig.51. It is natural because these models are produced by isotropic emission source, therefore, it is hard to produce "deformed" side-ward enhancement. Difference from the results of single moving source model fitting can be found in Fig.52. They are different, to be sure, but the difference is very small. The fitting results using two moving source model is slightly different from that of single moving source model. As written in Tab.10 as "Two MS", there are small improvement on the obtained reduced χ^2 comparing to that of the single moving source model.

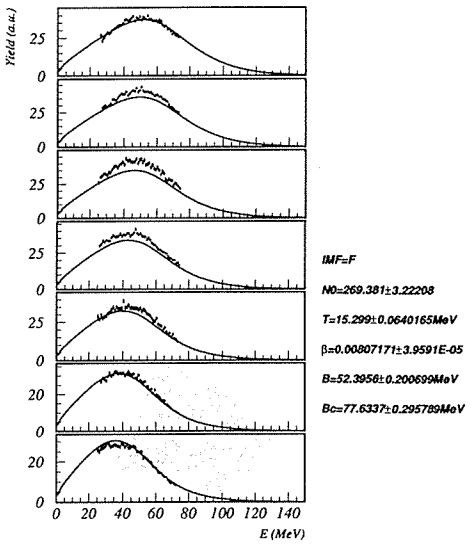

Figure 48: Fitting results of the energy spectra of F fragment produced in 12GeV p + Au reaction with the single moving source model. Fit are performed only for 30° and 150°.

	N	O	F	Ne	Na
χ^2/n	16.7	7.7	5.2	4.9	4.7

Table 11: Reduced χ^2 for each IMFs. Fitted results of the flow moving source model are shown.

On the other hand, flow model and deformed moving source model can produce the side-ward enhancement. As shown in Fig.53, energy spectra can be fitted using the flow effect. In order to reproduce the yield enhancement towards sideward direction, this model may shift the energy spectra toward high energy side for the sideward direction. The resultant χ^2/n for "MS with Flow" is listed in the Tab.10.

The energy shifts are not found in Fig.53, to be sure, but a possibility of the energy shift at higher energy tail should be examined. Those energy spectra for relatively heavy IMFs which contain the high energy tail within their energy dynamic range, are studied using the flow moving source model. The fitted results of χ^2/n are listed in Tab.11. We cannot find an improvement even for those energy spectra of the heavy IMFs which completely contains their high energy tail.

We can find a great improvement on Tab.10 in the results of the deformed moving source model fitting ("Deformed MS") in Fig.55 and Fig.56. This is the only model which can fit the obtained energy spectra with reduced χ^2 around one. In the following analysis, all the energy spectra are fitted with the deformed moving source model. Fitting results on the IMFs are introduced in [123].

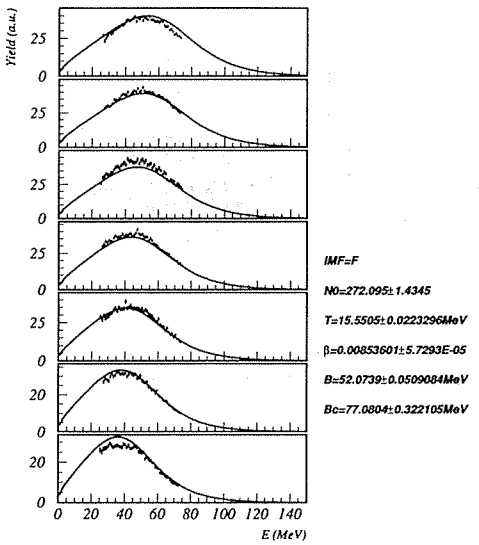

Figure 49: Fitting results of the energy spectra of F fragment produced in 12GeV p + Au reaction with the single moving source model. Fit are performed only for all angles.

4.9 Origin of the Side-ward Enhancement

Considering the fitting results using the various models, main source of the sideward yield enhancement can not be a dynamical effect as the nuclear flow. It is because any kind of flow can enhance the yield towards flow direction, however, it shifts the energy spectra because of the flow momenta. Observed sideward yield enhancement have no significant energy shift. This fact implies that there must be fragment formation probability enhancement at the sideward region. The Gaussian formed sideward enhancement factor have introduced only phenomenologically into the deformed moving source model. Therefore it cannot directly deduce interpretations of the model, however, the possibility of the fragmentation probability deformation without energy shift can be concluded.

4.10 IMF-multiplicity dependence

Only inclusive spectra have been considered in the previous sections. It was because there are slight IMF-multiplicity dependences observed. As for the sideward enhancement, there cannot find clear IMF-multiplicity dependences. For example, energy spectra with IMF-multiplicity gate are shown in Fig.57, Fig.58, and Fig.59. As for the shape of the energy spectra, small energy shift towards small energy direction were observed for high IMF-multiplicity data. However, there are no phenomena which shows a clear IMF-multiplicity dependences. The reason why there are slight IMF-multiplicity dependence on the IMF energy spectra will be discussed in the following section.

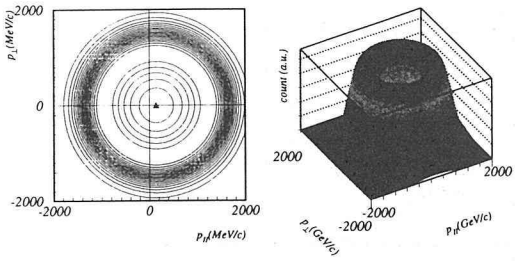

Figure 50: Resultant contour plot of the invariant cross section. Corresponding to the fitted result of Fig.48.

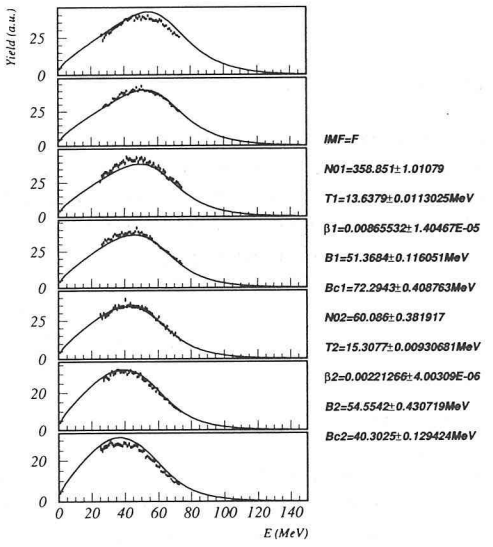

Figure 51: Fitting results of the energy spectra of F fragment produced in 12GeV p + Au reaction with the two moving source model.

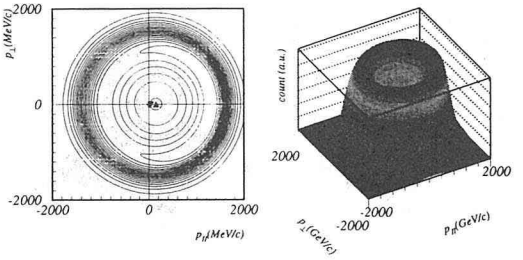

Figure 52: Resultant contour plot of the invariant cross section. Corresponding to the fitted result of Fig.51.

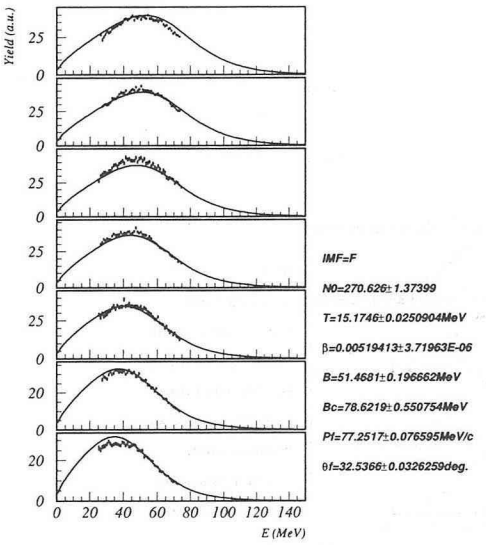

Figure 53: Fitting results of the energy spectra of F fragment produced in 12GeV p + Au reaction with the flow moving source model.

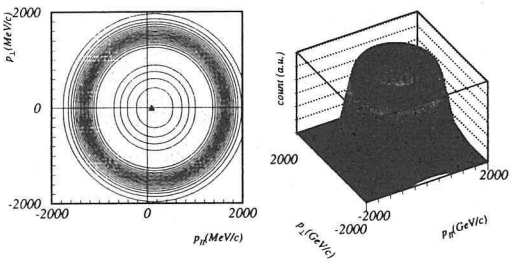

Figure 54: Resultant contour plot of the invariant cross section. Corresponding to the fitted result of Fig.53.

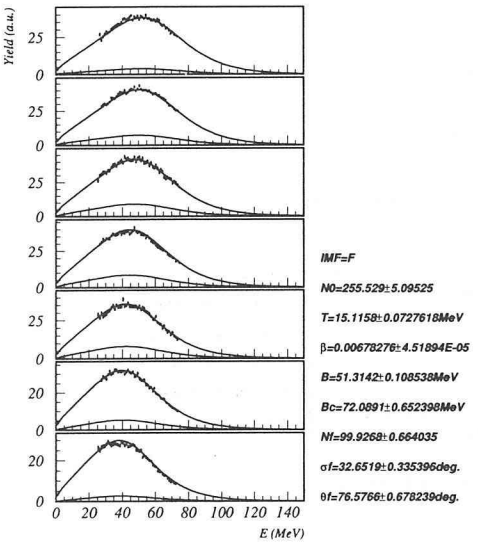

Figure 55: Fitting results of the energy spectra of F fragment produced in 12GeV p + Au reaction with the deformed moving source model.

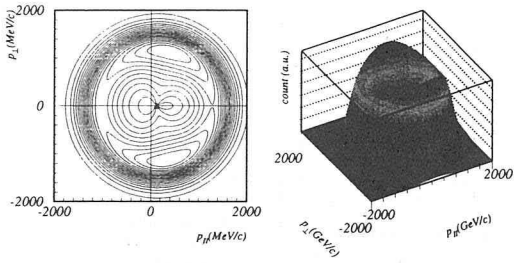

Figure 56: Resultant contour plot of the invariant cross section.
Corresponding to the fitted result of Fig.55.

4.11 Sensitivity on the IMF-multiplicity

The fitted results have small IMF-multiplicity dependence. Fig.57, Fig.58, and Fig.59 shows the results of deformed moving source model fitting with IMF-multiplicity selection. As shown in the figures, there can not be found the IMF-multiplicity dependence except of the production cross sections. IMF-multiplicity can be a probe for the impact parameter of the reaction[115]. On this assumption, we should conclude that there are very small impact parameter dependence on the energy spectra. It is not clear that whether the angular distribution for the large impact parameter b events should have same sideward peaking angular distribution as that of central colliding event. In order to check the phenomena, impact parameter dependence on the resulting angular distribution have been studied.

$$Y(\theta, b) = \frac{1}{2\pi} \int_0^{2\pi} d\phi \int_0^1 dr \rho(r, \theta, \phi) \tag{29}$$

$$\rho(r, \theta, \phi) = \rho_c(\theta_c), \tag{30}$$

where $\rho_c(\theta_c)$ is the fragment density function of θ_c. The definition of the θ_c is shown in Fig.60.

Transformation between (r, θ, ϕ) and (r_c, θ_c, ϕ_c) is defined as below.

$$\theta_c = cos^{-1}\left(\frac{r}{r_c} cos\theta\right) \tag{31}$$

$$r_c = \sqrt{r^2 + 2br sin\theta cos\phi + b^2} \tag{32}$$

$\rho_c(\theta_c)$ is a density function of θ_c. Yield angular distribution at the moving source system obtained by deformed moving source model fitting in Fig.55 is used for the $\rho_c(\theta_c)$. Here the fragment emission direction is assumed to be started from the target center O in Fig.60. There are another possibility. The emission center can be the center of the penetrating line P in Fig.60. In the latter case the resultant angular distribution can not have impact parameter dependence. Therefore, we do not have to study for this case. The emission center is assumed to be at the target center O in the following calculations. As shown in Fig.61, we can find strong sideward suppression for large b. In order to compare between this calculation and the experimental data, $Y(\theta, b)$ should be integrated over the impact parameter from 0 to adequate maximum impact parameter corresponding to the IMF-multiplicity. The impact parameter integrated angular distribution have been shown in Fig.61.

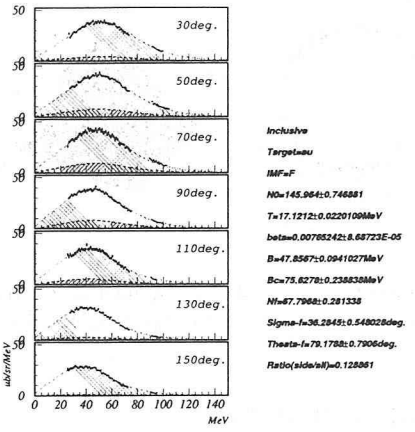

Figure 57: Results of the deformed moving source model fitting on F inclusive energy spectra produced in 12 GeV p + Au reaction.

$$Y(\theta) = \int_0^{b_{max} \leq 1} dbY(\theta, b) \tag{33}$$

In Fig.61, the impact parameter dependence is small both for exclusive case and inclusive case. The small impact parameter dependence obtained here shows that there can not be large impact parameter dependence on the angular distribution even if we suppose the target center as the emission center.

5 Temperature

5.1 Nuclear Temperature

Over the past few decades a considerable number of studies have been made on extracting nuclear temperatures from experimental data of intermediate and relativistic energy heavy ion collisions. The main aim of the temperature measurement is a search for a signal of nuclear liquid-gas phase transition. Although many people tried to determine the nuclear temperature from slope of the energy spectra, usually they had much higher temperatures than expected because of dynamical effects. To avoid the difficulty, relative populations of excited states were used, but this method is experimentally difficult to determine the yield of the excited states. Isotope yield ratio has been recently brought to light by the determination of the "caloric curve" [89]. One advantage of this method is the experimental simplicity. Isotope temperature, as a probe for a chemical freeze out temperature, can be obtained only by forming isotope yield ratios [83]. We can also determine the free proton and free neutron density at the same time [83]. On the purpose of extracting information about property of nuclear matter and dynamics on the reaction, nuclear temperature and density evaluation have been performed using isotope temperature method in this study. At first, each thermometer will be briefly reviewed [70].

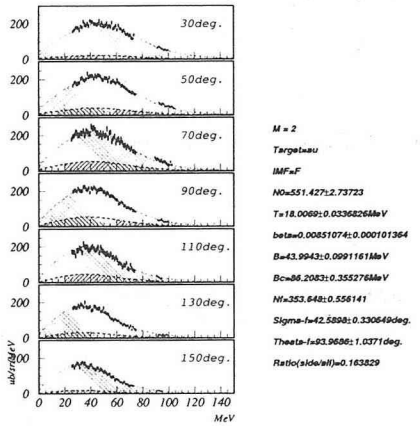

Figure 58: Results of the deformed moving source model fitting on F IMF-multiplicity = 2 energy spectra produced in 12 GeV p + Au reaction.

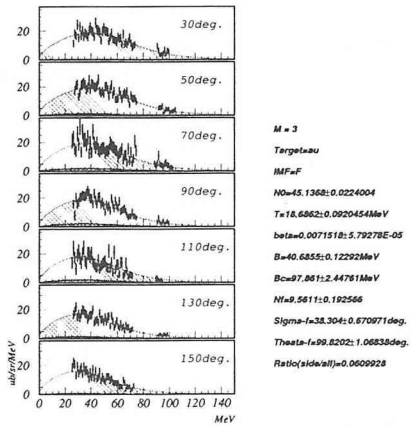

Figure 59: Results of deformed moving source model fitting on F IMF-multiplicity = 3 energy spectra produced in 12 GeV p + Au reaction.

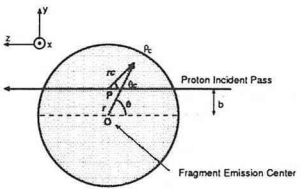

Figure 60: Definition of the coordinates.

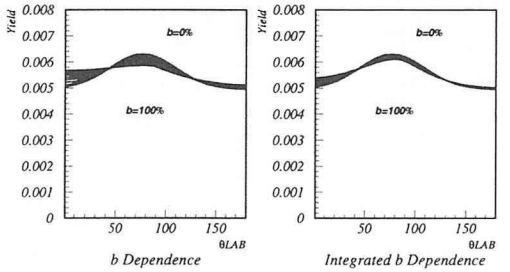

Figure 61: Impact parameter dependence of the yield angular distribution at the moving source frame.

5.1.1 Inverse Slope Parameter

The kinetic energy spectra of IMFs can be parameterized by a Maxwell-Boltzmann distribution with the temperature parameter T. The "slope temperature" have been widely used as a thermometer. However, the measured slope temperatures showed much more high value than expected. It should mainly due to non-thermal collective contributions to the energy spectra in the heavy ion collisions. Although the slope temperature observed at proton induced reaction have also high value. It is hard to explain the large slope parameter using collective expansion because of their small pressure in the colliding system. As shown in Sec.4, the obtained slope temperatures in this experiments using the moving source models have their value over 10MeV. The very high values can be understood as a consequent of the Fermi-Dirac statics of the nucleons for the light particle induced reactions [75].

5.1.2 Energy Distribution of the Nucleons

In order to study the energy distribution of the fragments, energy distribution of the nucleons which consist the observed fragments should be considered. There are two case to be considered.

1. Maxwell-Boltzmann (MB) distribution

$$F_{MB}(E) \propto exp\left(-\frac{E}{T}\right) \tag{34}$$

2. Fermi-Dirac (FD) distribution

$$F_{FD}(E) \propto \frac{1}{1+exp\left(-\frac{E-\mu}{T}\right)} \tag{35}$$

Here T is the initial temperature parameter, and E is the kinetic energy of the nucleons. μ is Fermi energy for the Fermi-Dirac distribution. F_{FD} should be different for proton distribution and neutron distribution because of their Fermi energy differences. Fermi energy for the proton and neutron have been obtained assuming that proton-shell and neutron-shell have same volume area. Fermi momentum can be written as following using the proton-shell radius R_p and neutron-shell radius R_n.

$$\begin{aligned} k_{Fp} &= \left(\frac{9\pi}{4}\right)^{1/3} \frac{1}{R_p} \\ k_{Fn} &= \left(\frac{9\pi}{4}\right)^{1/3} \frac{1}{R_n} \end{aligned} \tag{36}$$

Then Fermi energy for proton shell and neutron shell can be written as following.

$$\begin{aligned} E_{Fp} &= \frac{\hbar k_{Fp}}{2Mp} = \mu_p \\ E_{Fn} &= \frac{\hbar k_{Fn}}{2Mn} = \mu_n \end{aligned} \tag{37}$$

Using Eq.37, initial Fermi-Dirac distribution for proton and neutron can be obtained.

5.1.3 Energy Distribution of the Fragments

Energy spectra of the fragments can be obtained by summing up the nucleons which have their energy distribution described as Eq.34 or Eq.35. The direction of the individual nucleon momentum are randomly chosen in the summation. The summed fragment (mass number A) momentum $\vec{P}_A$ can be obtained as following using the i-th nucleon momentum $\vec{P}_i$.

$$\vec{P}_A = \sum_{i=1}^{A} \vec{P}_i \tag{38}$$

Resultant momentum distribution $\rho(\vec{P}_A)$ should be Gaussian distribution due to the central limit theorem. Energy distribution of the composite particle can be written using initial nucleon energy distribution analytically.

$$\rho(\vec{P}_A) = \int \prod_{i=1,A} \{d^3p_i F_{FD}(\vec{P}_i)\} \delta^3 \left(\vec{P}_A - \sum_{i=1,A} \vec{P}_i\right) \tag{39}$$

$$= \frac{1}{\sqrt{2\pi A\sigma^2}} exp\left(-\frac{P_A^2}{2A\sigma^2}\right) \tag{40}$$

Where σ is standard deviation of the momentum distribution. Transformed fragment energy distribution may be Maxwell-Boltzmann like functional form Eq.41.

However the most simple way to study the relation between initial nucleon temperature and resultant fragment energy distribution is to perform a Monte Carlo simulation. Example of resulting fragment spectra obtained by a Monte Carlo simulation are shown in Fig.62. In this figure, initial temperature for the nucleon energy distribution is set to be $T = 10MeV$. Energy spectra for Fermi-Dirac distribution is obtained using the Fermi energy for ^{197}Au. Solid lines in the spectra is results of Boltzmann-like function fitting. The fitting function is

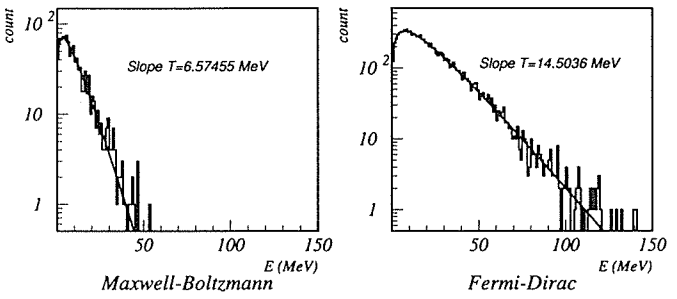

Figure 62: Fragment energy spectra obtained by a Monto Calro Simulation for MB and FD initial statics with $Tin = 10MeV$.

$$F_{IMF}(E) = N\sqrt{E}exp\left(-\frac{E}{T_{out}}\right). \tag{41}$$

Because of the existence of the factor $\sqrt{E}$, obtained T_{out} cannot has same value as the initial temperature even for MB initial distribution. This factor is indispensable to fit the low energy region of the spectra. If we used simple exponential functional form to get the slope temperature, T_{out} should be same value as the initial temperature for MB case. In order to understand the very high absolute slope temperature obtained in Sec.4, slope temperature in Eq.41 will be used in the following discussions. As shown in Fig.62, the obtained slope temperatures T_{out} for MB and FD cases are different from each other. T_{out} for FD case is much more higher than that for MB case. It is because the influence of Pauli blocking. This effect may be able to ignore in a very high temperature condition comparing to the Fermi energy of the target nuclei. In the present case, expected temperature should be same order as the Fermi energy, therefore, Pauli blocking effect can not be ignored. In order to obtain "real" temperature of the fragment source nuclear matter, relation between T_{out} for FD and the initial temperature T_{in} should be studied. In Fig.63, $T_{in} - T_{out}$ correlation is shown. In the region of $T_{in} < 20MeV$, T_{out} have an offset about 13MeV. This offset is caused by the effect of the Pauli blocking. This result is obtained for ^{10}B system. The solid line is a fitting result. In this case, the result is

$$T_{out} = 0.868T_{in} - 1.558 + \frac{211.39}{T_{in} - 14.702}. \tag{42}$$

Using Eq.42, we can extract initial temperature from the slope temperature. As shown in Fig.63, T_{out} is almost constant around $13MeV$ in low T_{in} region. In other words, there are small sensitivity to the T_{in} in this temperature region. Therefore, we cannot make detailed study on nuclear temperature using the slope temperature. Of course the transformation between T_{in} and T_{out} depends on the system. If we want to extract nuclear temperature only from the slope of the energy spectra, all the relation should be studied. There is fairly general agreement that the energy spectra suffer from (1) collective flow effects, (2) secondary decay processes, (3) multiple Coulomb interaction and (4) the Fermi motion effects discussed above.

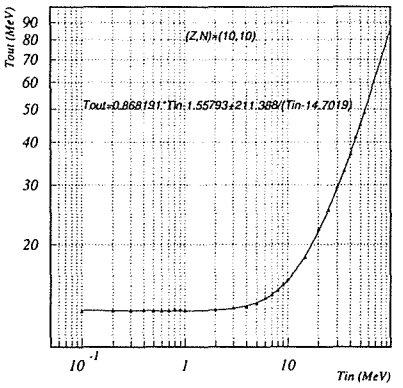

Figure 63: Relation between T_{in} and T_{out} for FD statics (^{10}B).

5.1.4 Excited State Temperature

The most direct way to make temperature determination is to measure the relative population ratio of two excited states of a given fragment. The exsisting probability at each energy level can be assumed to have Maxwell-Boltzmann distribution with an equilibrium temperature T.

$$P_i = (2s_i + 1) \cdot exp(-\frac{E_i}{T})/\omega \tag{43}$$

Here P_i is the existing probability on i-th state of a fragment. E_i is the energy level and s_i is the spin. ω is a internal partition function of the fragment. Thus relative population ratio between two excited states i, j of a same fragment can be written as following.

$$\frac{Y_i}{Y_j} = \frac{P_i}{P_j} = \frac{2s_i + 1}{2s_j + 1} \cdot exp(-\frac{E_i - E_j}{T}) \tag{44}$$

Therefore we can estimate "excited state temperature" using two level yield as following.

$$T = (E_j - E_i)/ln\left(\frac{Y_i}{Y_j}\frac{2s_j + 1}{2s_i + 1}\right) \tag{45}$$

For example, we can estimate the emission temperature from population ratio between two states of ^5Li fragments. The population of the states can be estimated from a coincidence measurement of the decay products. In this case, the relation

$$\frac{Y(^5Li_{16.66MeV})}{Y(^5Li_{g.s.})} \propto exp(-\frac{\Delta E}{T}) \tag{46}$$

can be assumed. Here Y is the state population and ΔE is the state energy difference between the ground state (g.s.) and the $16.66MeV$ state. Existence of the each state can be experimentally

obtained using below decay.

$$\begin{aligned} {}^5Li_{16.66MeV} &\rightarrow d + {}^3He \\ {}^5Li_{g.s.} &\rightarrow p + \alpha \end{aligned} \tag{47}$$

This method can be used to extract temperature in high energy heavy ion collision experiment using relative population ratio between excited states of mesons and baryons. For example, reaction temperature can be determined using relative yield of Δ baryons and N baryons instead of excited states of the nuclear fragments like below.

$$\frac{Y(\Delta)}{Y(N)} \propto exp(-\frac{\Delta E}{T}) \tag{48}$$

In order to obtain the emission temperature using the internal excitation as introduced above, demanding coincident measurement of the decay products must be required for the analysis. On the other hand, isotope temperatures which will be discussed in the following can be extracted from particle yield ratios. The main two particle correlation to be studied in order to reconstruct the fragment excited states are $(p+\alpha), (d+\alpha), (\alpha+\alpha)$. The experimental threshold of the *Bragg* peak is set to be above Li fragments for reducing the trigger rate. Therefore there are no experimental data for p, d and α. Experimental yield of the light charged particles as p, d and α must be strongly affected by sequential decay feeding comparing to heavier particles. The another reason why we have not taken H and He isotopes besides the trigger rate is the difficulty on the yield correction for those light charged particles. On this point of view, isotope temperature is the most simple methods to obtain the nuclear temperature in the experimental setup using BCC.

5.1.5 Chemical Temperature

Isotope temperature is a strong tool to make nuclear temperature measurement because of its experimental simplicity. The principle of this methods is same as excited state population methods assuming Maxwell-Boltzmann distribution on the states population. Instead of identifying the states, total yield ratio between isotopes are used to extract temperature. In this method, binding energy difference is the probe for extracting temperature instead of the excited state energy difference on the excited state temperature method. Not only thermal equilibrium but also chemical equilibrium is assumed in this method. The detail will be discussed in following section.

5.2 Isotope Temperature

Isotope temperature method was first introduce by S.Albergo in 1985 [83]. After the publication of his paper in this method, many experimental study have been performed in order to extract nuclear temperature. Although isotope temperature method is a very simple and strong tool, excited state temperature became more common tool as a nuclear thermometer because the excited stated temperature can make more direct the temperature measurement. Unfortunately, probing nuclear liquid-gas phase transition, which has been the main aim of the temperature measurement, have not be succeeded using the excited state temperature. In 1995, J. Pochodzalla reported the "caloric curve" which clearly show the appearance of nuclear liquid-gas phase transition [89]. There are two points which insist that they are in complete gas phase because of their very high temperature above a plateau. Using excited state temperature, they cannot produce such sharp turning point from the plateau in the high energy density region. The conclusion on the origin of the difference between caloric curves obtained by the isotope temperature and by the excited stated temperature, have not still been confirmed. Opinions are divided on this subject. My opinion is that, one cannot readily

believe that the appearance of the liquid-gas phase transition can be measured neither by the isotope temperature nor by the excited state temperature. It is because these method assume the existence of the fragments to be detected, which can not exist in a complete nucleon gas phase. They have sensitivities on only a remaining information on the produced temperature on the nuclear collision. The relation between the isotope temperature or the excited state temperature and the maximum temperature appeared in a nuclear collision have been vigorously studied by theorists [98]. The physical meaning of the isotope temperature is still not clear. We may leave this details to Sec.7 and discuss about the analysis using isotope temperature method.

5.2.1 Original Formalism

There are two widely used isotope thermometers T_{HeDT} and T_{HeLi}. They can be expressed in the following relation using the isotope yield Y.

$$T_{HeDT} = 14.3/ln\left(\frac{Y_D \cdot Y_{^4He}}{Y_T \cdot Y_{^3He}} \cdot 1.6\right) \tag{49}$$

$$T_{HeLi} = 16/ln\left(\frac{Y_{^6Li} \cdot Y_{^4He}}{Y_{^7Li} \cdot Y_{^3He}} \cdot 2.18\right) \tag{50}$$

These thermometers can be obtained within original isotope method introduced by S. Albergo et al. [83]. T_{HeLi} was used in the caloric curve reported by Pochodzalla [89]. Eq.50 includes a correction factor for the sequential decay. According to Albergo et al., density of a fragment (A, Z) at the local thermal and chemical equilibrium with temperature T can be expressed as below.

$$\rho(A,Z) = \frac{A^{3/2}}{\lambda_{TN}^3}\omega(A,Z)exp\left(\frac{\mu(A,Z)}{T}\right) \tag{51}$$

Here $\lambda_{TN} = h/\sqrt{2\pi M_N T}$ is thermal nucleon wave-length. M_N is the nucleon mass. $\omega(A,Z)$ is internal partition function of (A,Z). It can be expressed as below.

$$\omega(A,Z) = \sum_{i=allstates}(2s_i+1)exp\left(-\frac{E_i}{T}\right) \tag{52}$$

The chemical potentials $\mu(A,Z)$ can be expressed using chemical potential of free proton μ_p and neutron μ_n and the nuclear binding energy $B(A,Z)$ at the chemical equilibrium.

$$\mu(A,Z) = Z\mu_p + (A-Z)\mu_n + B(A,Z) \tag{53}$$

From Eq.51, free proton density ρ_{pF} and neutron density ρ_{nF} can be expressed using their chemical potential μ_p and μ_n.

$$\begin{aligned}\rho_{pF} &= \frac{2}{\lambda_{TN}^3}exp\left(\frac{\mu_p}{T}\right)\\ \rho_{nF} &= \frac{2}{\lambda_{TN}^3}exp\left(\frac{\mu_n}{T}\right)\end{aligned} \tag{54}$$

Using Eq.51 and Eq.54, fragment density can be expressed using the three unknown quantity T, ρ_{pF} and ρ_{nF}.

$$\rho(A,Z) = A^{3/2}\frac{\lambda_{TN}^{3(A-1)}}{2^A}\omega(A,Z)\rho_{pF}^Z\rho_{nF}^{A-Z}exp(\frac{B(A,Z)}{T} \tag{55}$$

Now if we got three independent fragment densities, we could extract T, ρ_{pF} and ρ_{nF}. Instead of extracting the fragment densities, isotope yield ratios will be used in order to get T, ρ_{pF} and ρ_{nF}. If

$$\frac{\rho_(A_1, Z_1)}{\rho_(A_2, Z_2)} = \frac{Y_(A_1, Z_1)}{Y_(A_2, Z_2)} \tag{56}$$

can be assumed for fragment yields Y of fragments (A_1, Z_1) and (A_2, Z_2), the single isotope yield ratio can be expressed as below.

$$\begin{aligned}\frac{Y(A_1, Z_1)}{Y(A_2, Z_2)} &= \left(\frac{A_1}{A_2}\right)^{3/2} \left(\frac{\lambda_{TN}^3}{2}\right)^{A_1 - A_2} \frac{\omega(A_1, Z_1)}{\omega(A_2, Z_2)} \rho_{pF}^{Z_1 - Z_2} \rho_{nF}^{(A_1 - Z_1) - (A_2 - Z_2)} \\ &\quad \times exp \frac{B(A_1, Z_1) - B(A_2, Z_2)}{T}\end{aligned} \tag{57}$$

Taking into only ground states into the internal partition function $\omega(A, Z)$, Eq.49 and Eq.50 can be obtained. Generally, T can be expressed using double yield ratio $(Y_1 Y_2)/(Y_3 Y_4)$.

$$T = B/ln\left(\alpha \frac{Y_1 Y_3}{Y_2 Y_4}\right) \tag{58}$$

Here $Y_{1,2,3,4}$ are isotope yields. In order to get Eq.58, there are strong restriction on selecting isotope combinations and the excited state influence on the internal partition function;

$$\begin{aligned}&[(A_1 - Z_1) - (A_2 - Z_2) = (A_3 - Z_3) - (A_4 - Z_4) = 0] \cap [|Z_1 - Z_2| = |Z_3 - Z_4|] \\ \cup\ &[Z_1 - Z_2 = Z_3 - Z_4 = 0] \cap [|A_1 - A_2| = |A_3 - A_4|]\end{aligned} \tag{59}$$

and

$$\omega(A, Z) = 2s_{g.s.} + 1. \tag{60}$$

These restriction is to get simple temperature formula Eq.58 using double ratio. All the experimental and theoretical studies except of the present work have used Eq.58 because of the simplicity. It may because the detected isotopes are restricted on p, d, α and Li isotopes. With all the simplicity, the restriction Eq.59 have small significance. Without Eq.59, there are huge number of combinations which can be used as the thermometers. In the following section, extended formalism to get all the possible thermometers will be introduced. This double ratio method can be applied to a high energy heavy ion experiment as same as for the excited states temperature. For example,

$$T = B/ln\left(\alpha \frac{\pi^- \Xi^-}{K^- \Sigma^-}\right) \tag{61}$$

can be a chemical thermometer for a very high temperature ($T > 100 MeV$) system.

5.2.2 Extended Formalism

In our experiment, ^6Li,^7Li,^8Li,^9Li,^7Be,^9Be,^{10}Be fragments can be identified, and then their yield can be obtained. Using these seven isotope yields, there are only eight double ratios which satisfy Eq.59. All the eight double ratios are written in the following.

$$\begin{aligned}&\frac{Y(^7Li)Y(^9Be)}{Y(^6Li)Y(^{10}Be)}, \frac{Y(^7Li)Y(^8Li)}{Y(^6Li)Y(^9Li)}, \frac{Y(^7Li)^2}{Y(^6Li)Y(^8Li)}, \frac{Y(^8Li)Y(^{10}Be)}{Y(^9Li)Y(^9Be)}, \frac{Y(^7Li)Y(^{10}Be)}{Y(^8Li)Y(^9Be)}, \\ &\frac{Y(^7Li)Y(^9Li)}{Y(^8Li)^2}, \frac{Y(^6Li)Y(^{10}Be)}{Y(^7Be)Y(^9Li)}, \frac{Y(^6Li)Y(^9Be)}{Y(^7Be)Y(^8Li)}\end{aligned} \tag{62}$$

Without the restriction Eq.59 for making double ratio, there are huge number of available ratio combinations. There are four unknown quantities to be extracted. T, ρ_{pF}, ρ_{nF} and the ratio $r = \rho/Y$ between the fragment density $\rho(A,Z)$ and the yield $Y(A,Z)$. The ratio r is needed because of the assumption Eq.56. Thus, T, ρ_{pF}, ρ_{nF} and r can be obtained from four isotope yields. The direct deviation from the four yields to T, ρ_{pF}, ρ_{nF} and r is very complicated. Of course it is possible using Eq.55 and Eq.56, but we will use the single yield ratio as the experimental observable instead of the raw isotope yields. It is because the calculation is much more simple than that from raw isotope yields.

As shown in Eq.57, all single yield ratios $R_i = Y(A_1,Z_1)/Y(A_2,Z_2)$ can be expressed as below [83].

$$R_i = (\frac{\lambda_{TN}^3}{2})^{\eta_i+\xi_i}\rho_{pF}^{\eta_i}\rho_{nF}^{\xi_i}\alpha_i exp\frac{\Delta B_i}{T} \tag{63}$$

where R_i is the i-th single ratio. The index η, ξ means $\eta_i = Z_1 - Z_2$ and $\xi_i = (A_1 - Z_1) - (A_2 - Z_2)$. Binding energy differences are $\Delta B_i = B(A_1,Z_1) - B(A_2,Z_2)$, and $\alpha_i = (\lambda_{TN}/2)^{A_1-A_2}(A_1/A_2)^{3/2}\omega(A_1,Z_1)$

Single yield ratio Eq.(63) can be obtained using Eq.(56) with the assumption,

$$\rho(A,Z) \propto Y(A,Z) \tag{64}$$

We should notice that the information about the angular distribution of the fragment density $\rho(A,Z)$ have been included into the calculation as experimental results.

The three unknown quantity T, ρ_{pF} and ρ_{nF} can be extracted from the three experimental single ratios. Using the single ratios, the ratio r do not have to be extracted because of Eq.56.

From Eq.63, the three single isotope yield ratio R_i, R_j, R_k can extract T, ρ_{pF} and ρ_{nF} as following.

$$T = \sum_{i=1,3} a_i\Delta B_i/ln\prod_{i=1,3}(R_i/\alpha_i)^{a_i} = B/ln(R/\alpha(T)). \tag{65}$$

$$\rho_{pF} = \frac{2}{\lambda_{TN}^3}[(\frac{R_i}{\alpha_i})^{\xi_j}(\frac{R_j}{\alpha_j})^{\xi_{-i}}exp(\frac{\Delta B_j\xi_i - \Delta B_i\xi_i}{T})]^{\frac{1}{\eta_i\xi_j-\eta_j\xi_i}} \tag{66}$$

$$\rho_{nF} = \frac{2}{\lambda_{TN}^3}[(\frac{R_i}{\alpha_i})^{\eta_j}(\frac{R_j}{\alpha_j})^{\eta_{-i}}exp(\frac{\Delta B_j\xi_i - \Delta B_i\xi_i}{T})]^{\frac{1}{\xi_i\eta_j-\xi_j\eta_i}} \tag{67}$$

where $a_i = \xi_j\eta_k - \xi_k\eta_j$ for (i,j,k) = cyclic order of $(1,2,3)$. There are three possible combinations to select which two single ratios to make ρ_{pF} and ρ_{nF}.

$$(i,j,k) \to (i,j),(j,k),(k,i) \tag{68}$$

In Eq.65, binding energy parameter B, "multi ratio" R and a factor $\alpha(T)$ are introduced for a simplicity.

$$\begin{aligned} B &= \sum_{i=1,3} a_i\Delta B_i \\ R &= \prod_{i=1,3} R_i{}^{a_i} \\ \alpha(T) &= \prod_{i=1,3} \alpha_i{}^{a_i} \end{aligned} \tag{69}$$

The reason why the factor $\alpha(T)$ depends on T is that, α_i contains the internal partition function $\omega(A,Z)$ which are generally depend on T if they contain the excited states into the summation except of the ground states.

5.2.3 Available Combinations

In this section number of possible combinations to reconstruct the T, ρ_{pF} and ρ_{nF} is studied. There are twenty one single ratios combined by the seven isotopes.

$$\begin{aligned}
&\frac{Y(^{10}Be)}{Y(^{6}Li)}, \frac{Y(^{10}Be)}{Y(^{7}Be)}, \frac{Y(^{10}Be)}{Y(^{9}Li)}, \frac{Y(^{9}Be)}{Y(^{6}Li)}, \frac{Y(^{10}Be)}{Y(^{7}Li)}, \frac{Y(^{10}Be)}{Y(^{8}Li)}, \frac{Y(^{9}Be)}{Y(^{7}Be)}, \\
&\frac{Y(^{9}Be)}{Y(^{7}Li)}, \frac{Y(^{9}Be)}{Y(^{8}Li)}, \frac{Y(^{7}Be)}{Y(^{9}Li)}, \frac{Y(^{8}Li)}{Y(^{6}Li)}, \frac{Y(^{9}Be)}{Y(^{9}Li)}, \frac{Y(^{7}Li)}{Y(^{6}Li)}, \frac{Y(^{10}Be)}{Y(^{9}Be)}, \\
&\frac{Y(^{9}Li)}{Y(^{6}Li)}, \frac{Y(^{7}Be)}{Y(^{6}Li)}, \frac{Y(^{9}Li)}{Y(^{8}Li)}, \frac{Y(^{7}Be)}{Y(^{7}Li)}, \frac{Y(^{8}Li)}{Y(^{7}Li)}, \frac{Y(^{9}Li)}{Y(^{7}Li)}, \frac{Y(^{7}Be)}{Y(^{8}Li)}
\end{aligned} \tag{70}$$

The maximum combination number C_{max} is the combination choosing three quantity from twenty one quantity.

$$C_{max} = {}_{21}C_3 = \frac{21!}{3! \cdot 18!} = 1330 \tag{71}$$

Because of the possibility of selecting two single ratio to reconstruct free nucleon densities as Eq.68, there are

$$C_{max} \times {}_3C_2 \times {}_3C_2 = 11970 \tag{72}$$

combinations to get T, ρ_{pF} and ρ_{nF}. The main aim this chapter is to extract the nuclear temperature, therefore, the optional combinations from Eq.68 are ignored. That will be discussed in Sec.6. In $C_{max} = 1330$ combinations, there are those combinations which can produce only two quantity (T,ρ_{pF}) or (T,ρ_{nF}). It is because all the single ratios selected for these multi ratio don't have informations about ρ_{pF} or ρ_{nF}. They are corresponding to those ratio which $\eta = 0$ or $\xi = 0$. There are nine single ratio which $\eta = 0$ and three single ratio which $\xi = 0$. In order to get T, we don't have to use three single ratio but two for these combinations. Thus the corrected number of combination is

$$C_{total} = C_{max} - {}_9C_3 - {}_3C_3 + {}_9C_2 + {}_3C_2 = 1284. \tag{73}$$

Although 1284 patterns of multi ratio can be extracted from the 1284 single ratio combinations, they are not independent from each other. It is because the single ratios are consisted by the raw isotope yields, therefore, produced multi ratio written by isotope yields can be same as another single ratio combinations. After reducing the "double counting" patterns, the number of the combination is 238. In those 238 multi ratios, there are eight multi ratio which $\alpha(T) = 0$. These ratio can not produce the temperature. Thus, the available independent combination C_T should be reduced.

$$C_T = 238 - 8 = 230 \tag{74}$$

This number $C_T = 230$ is the available number of multi ratio combinations for extracting temperatures.

5.3 Excited State Correction

5.3.1 Correction Procedure

If we consider the existence of the excited states, $\omega(A, Z)$ should be a function of T. Therefore T should be obtained as a numerical solution of Eq.65.

$$\omega(A,Z) = \sum_{i=allstates} (2s_i+1) exp\left(\frac{E_i}{T}\right) \tag{75}$$

where s_i and E_i means the spin and excitation energy of the i-th states. The summation should be performed for $0 \leq E_i \leq several \times T$. It is because those excited states which $E_i \leq several \times T$ are difficult to be produced in the environment with T. Here T is assumed to be within $10MeV$ at the freeze out condition, therefore the maximum excited state energy in the summation should be about $\sim 20-30MeV$.

5.3.2 Corrected Results

The relation between T and R have been obtained as numerical solutions for each ratio combination for

1. $\omega(A,Z) = (2s_{gs}+1)$
   ground state only
2. $\omega(A,Z) = \sum_{i=gs+\gamma}(2s_i+1)exp\left(\frac{E_i}{T}\right)$
   ground state + γ-excited states

have been estimated as Fig.64. Expected temperature for (gs+γ) must be significantly smaller than that of (gs) for same R. As shown in Fig.64, the correction effects are strongly depend on the ratio combination. The reason why the ratio combination dependence on the correction effects are so strong may due to the structure of the excited states. The correction should be performed in order to get proper temperature. Although the excited states correction is indispensable, the correction is not needed if we make yield correction which is discussed the in sequential decay correction (section 5.5). The main aim of the yield correction is considered to be sequential decay, however, the yield correction can be applied for any kind of physical effects which can make influence on the experimental yields. Thus, after the yield correction fitting, we can consider that the yield correction factor contains the correction effects for the existence of the excited states at the chemical freeze out. Therefore the excited state correction on the internal partition function do not have to be performed explicitly in the calculation. No one have tried to put the excited states into the internal partition function ω for the ground-canonical classical model. According to Albergo, the influence of the excited states in the partition function can be negligible in the classical grand-canonical treatment [132]. He compared the results obtained by a classical grand-canonical treatment without excited states influence, and by Quantum Statistical Model which take all the excited states into the calculation. The results are very similar with each other. It means that at least for the classical treatment, we can obtain the temperature without excited states correction, which have close value to the results of Quantum Statistical Model.

5.4 Isotope Yield Estimation

Energy spectra are obtained using the isotope separation procedure written in Chap3. Background events are subtracted run by run considering the fluctuation of the beam profile. IMF-multiplicity (Inclusive, 2, and 3) selected energy spectra for $^{6,7,8,9}Li$ and $^{7,9,10}Be$ fragments are obtained. For E393 data, high multiplicity events are studied only for the P10-gas mode. Energy shift caused by the energy loss in the foil targets and the entrance windows of the detectors are corrected. Seven energy spectra obtained by the inplane counters, which are corresponding to the laboratory angle of 30°, 50°, 70°, 90°, 110°, 130°, and 150°, are used for the isotope temperature analysis.

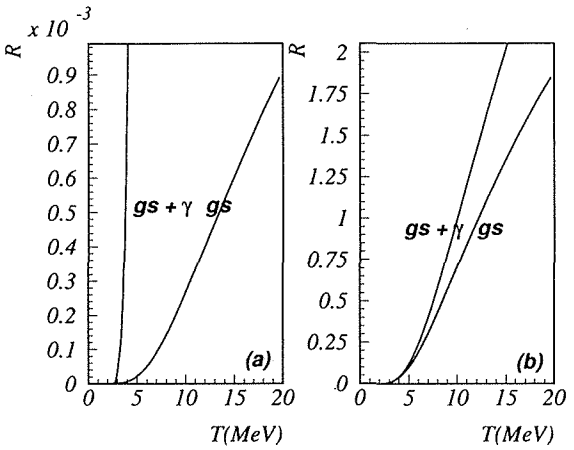

Figure 64: γ-excited state effects. Relation between T and R for (gs:ground state) and (gs+γ:ground state + γ-excited states) were shown. The excited states effects have strong ratio combination dependences,(a):$R = (Y_0(^9Li)^3Y_0(^7Be)^2)/(Y_0(^7Li)^3Y_0(^{10}Be)^2)$, and (b):$R = (Y_0(^8Li)^3Y_0(^7Be))/(Y_0(^7Li)^3Y_0(^{10}Be))$.

5.4.1 Deformed Moving Source Model Fitting

In order to estimate the total yield of the each fragment, deformed moving source model have been used to fit all the each energy spectra. Considering the existence of sideward yield enhancement [112][113], sideward deformation factor is introduced phenomenologically into the usual single moving source model.

All the inclusive energy spectra can be fitted using the deformed moving source model successfully, therefore, the total yields of each isotopes can be obtained as continuous functions of the angle. Fig.113, 114, 115, 116, 117, 118, 119 show the results of the deformed moving source model fitting on the E393 inclusive energy spectra for Au, Sm and Ag targets. The complete deformed moving source model fitting can be performed only for E393 inclusive data because both of the P10 data and CF_4 data are needed to produce energy spectra with wide energy dynamic range. Fitting parameters except of the normalizing parameters N_0 and N_f have been fixed with those value obtained by the deformed moving source model fitting on E393 inclusive data in the energy spectra fitting on E393 high multiplicity data and E337 data. It is because the meaning of the IMF-multiplicity is different from each other in P10 mode and CF_4 mode. In the CF_4 mode, low energy fragments cannot make a trigger because of its large stopping power. For E337 data, there are no CF_4 data. For the Tm target data of E337, the same shape parameters for Au target are used.

All the obtained fitting parameters on the E393 inclusive spectra are listed in Tab.19, 20 and Tab.21 without listing fitting errors. Isotope dependence of the shape parameters are also shown in Fig.65. Here normalization factor N_0 and N_f are treated in arbitrary units. N_0 and N_f obtained on E393 high IMF-multiplicity events and E337 data are written in Tab.22, 23, 24, 25, 26, 27, and Tab.28.

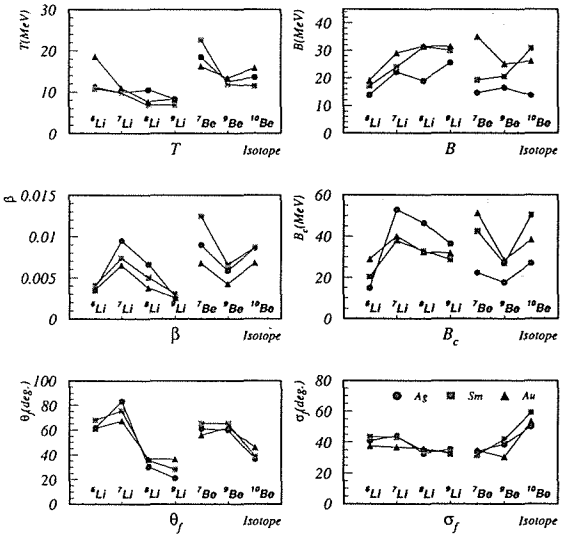

Figure 65: Isotope dependence of the fitting parameters for Au,Sm and Ag targets, obtained by the deformed moving source model fitting.
The fitting results are shown in Appendix.8.

5.4.2 Error estimation

Initial statistical error is contained in the energy spectra. Typical isotope yield and resultant statistical errors are shown in Tab.12. Statistical error of the integrated isotope yield (Y, σ_Y) is estimated by the fitting errors.

$$Y(\theta, p_1, p_2, , , , p_8) = \int_0^\infty f(E, \theta, p_1, p_2, , , , p_8) dE \tag{76}$$

Here f is the fitting function of the energy spectra, p_i are the fitting parameters. Resultant statistical error σ_Y of the yield Y is estimated using the statistical errors of the fitting parameters σ_i as following.

$$\sigma_Y(\theta, p_1, p_2, , , , p_8)^2 = \sum_{i=1}^{8} \left(\frac{Y}{p_i}\right)^2 \sigma_i^2 \tag{77}$$

Typical value of the statistical errors on the isotope yield is about $1 \sim 5\%$.

Systematic errors caused in the energy spectra fitting should be considered. Possible source of the systematic errors are listed in the following.

- Detector dependence of the fragment detection efficiencies
- Uncertainties on the isotope separation

	^6Li	^7Li	^8Li	^9Li	^7Be	^9Be	^{10}Be
Raw counts	4508.1	14796	4621.7	1435.2	1715.5	8809.2	11494.3
Stat. errors	78.37	140.88	92.54	45.15	56.44	104.08	120.16
(Inc.)	(1.74 %)	(0.95 %)	(2.00 %)	(3.15 %)	(3.29 %)	(1.18 %)	(1.05 %)
Raw counts	1515.5	5278.3	1985.7	599.67	632.23	2635.1	3669.3
Stat. errors	39.105	73.098	45.941	26.097	25.447	51.786	60.920
(M2)	(2.58 %)	(1.38 %)	(2.31 %)	(4.35 %)	(4.03 %)	(1.97 %)	(1.66 %)
Raw counts	168.0	549.0	191.8	75.2	74.0	250.0	389.0
Stat. errors	12.962	23.431	14.105	8.872	8.602	15.811	19.723
(M3)	(7.72 %)	(4.28 %)	(7.36 %)	(11.80 %)	(11.63 %)	(6.35 %)	(5.07 %)

Table 12: Typical isotope yield detected by a counter with Au targets in E337 (after background subtractions).

- Determination of the energy range for the fitting

Each of the above source may results systematic fluctuation as the angular dependence of the energy spectra. The fact that there are small observed fluctuations, such kind of systematic error may be treated as small. However, systematic errors caused in the energy spectra fitting may not be negligible. Resultant systematic fluctuations of the isotope yield will be contradicted to the yield distributions expected by thermal equilibrium. They will be discussed and systematic errors will be estimated in the following section. As shown in there, typical systematic errors on the final results of the temperature is about 10 %.

5.4.3 Shape Difference and Angular Distribution Difference between Isotopes

Using the results of the deformed moving source model fitting, total yields can be obtained by integrating from $E = 0$ to $E \to \infty$ at each angle. Obtained yields are shown in Fig.66 and Fig.67 as a function of the laboratory angle.

What must be noticed is the shape-differences between the angular distributions of the different isotopes. The sideward peaking angular distributions are observed for ^6Li, ^7Li, ^7Be, ^9Be. On the other hand, ^8Li, ^9Li, ^{10}Be have relatively small sideward yield enhancement for all the reactions (Fig.66 and Fig.66). If we try to explain the shape differences between the different isotopes using statistical thermodynamics, we must conclude that relatively low temperature should be observed at the sideward region of the emission source. It is because unstable fragment production should needs higher temperature environment, as high as their binding energy differences, than that of the stable fragments. On other words, if the temperature distribution of the hot source were uniform, the angular distributions of the each isotope yields might have same shapes of the angular distributions. Now qualitative discussion can be made on anisotropy of nuclear temperature distribution of the source nuclear matter only using isotope yield angular distributions, however, quantitative discussion will be able to performed after isotope temperature analysis. I shall return to this subject later.

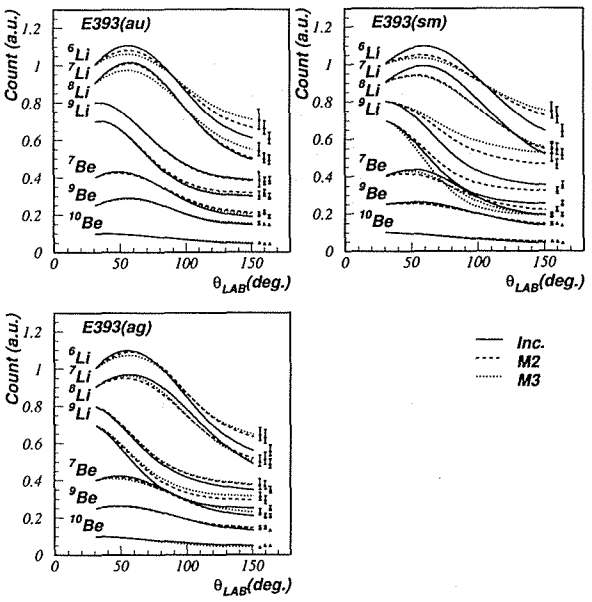

Figure 66: Resultant angular distribution (in arbitrary unit) for E393.

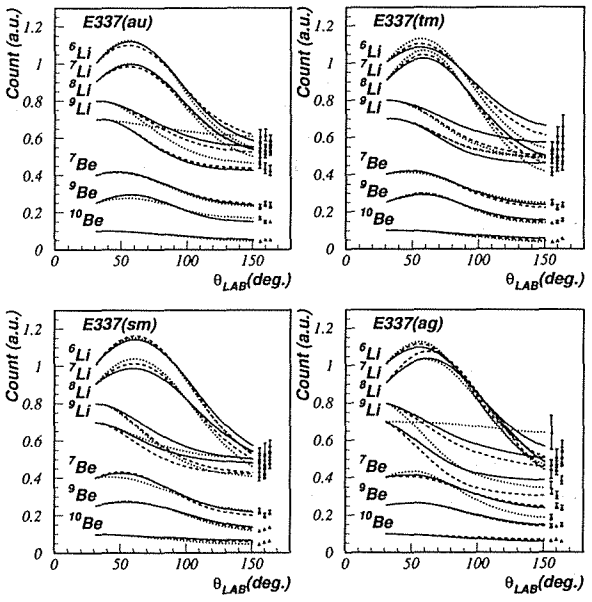

Figure 67: Resultant angular distribution (in arbitrary unit) for E337.

5.5 Sequential Decay Correction

5.5.1 Yield Correction

At first temperatures are calculated for all the combinations as functions of angles without any yield corrections. In this calculation, we consider only ground states into the $\omega(A,Z)$. The influence of the excited states can be also corrected in the yield correction discussed in the following. The results are distributed in a wide range between $-20MeV < T < 50MeV$. In order to select proper ratio combination, the binding energy difference $B = \sum_{i=1,3} a_i \Delta B_i$ in Eq.65 can be used as a standard. It is because if we select large value of the quantity

$$\delta B = |\sum_{i=1,3} a_i \Delta B_i| / \sqrt{\sum_{i=1,3} a_i^2}, \tag{78}$$

the fluctuation of the temperature distribution become narrow [88]. Scatter plot of the obtained temperature .vs. δB are shown in Fig.69. The main origin of the fluctuation can be the influence of the sequential decay. In order to correct the influence, each isotope yields $Y(A,Z)$ may be corrected as below.

$$Y_0(A,Z) = Y(A,Z)/k(A,Z) \tag{79}$$

If we knew exact values of the $k(A,Z)$ and calculated the temperatures using corrected yields Y_0, the fluctuation must be disappeared. That is to say, if we put one set of $k(A,Z)$ and got sharp temperature distribution, the origin of the fluctuation might be the sequential decay or some other unknown influence on the isotope yields.

On the similar procedure used in [88], the temperature distributions are tried to be fitted using seven $k(A,Z)$ parameters in order to get sharp temperature distribution. The experimental inclusive results of our KEK experiments ($12GeVp + Au, Tm, Sm, Ag; \theta_{LAB} = 34°$ and $8GeVp + Au, Sm, Ag; \theta_{LAB} = 34°$), FNAL experiment ($80GeV/cp + Xe; \theta_{LAB} = 34°$) [18] and MSU experiment ($35AMeVN + Ag; \theta_{LAB} = 38°$) [77] are studied. Here θ_{LAB} means the emission angle of the fragments. The yield at $\theta_{LAB} = 34°$ for the KEK experiment is extracted using the results of the deformed moving source model fitting. The fitting parameters are the seven $k(A,Z)$, which are set to have common values between each reactions. The variance around T_0 for all the combinations which has $\delta B > 5MeV$ are calculated in the fitting procedure. The parameter fitting is performed in order to produce the minimum variance.

$$T_0 = \frac{\sum_i T_i/\sigma_i^2}{\sum_i 1/\sigma_i^2} \tag{80}$$

$$Variance = \sum_i (T_i - T_0)^2/\sigma_i^2 \tag{81}$$

Here the summation on i is performed for $\delta B > 5MeV$ combinations. A very sharp temperature distribution can be obtained using the fitting results of $k(A,Z)$.

5.5.2 Parameter Fitting

In the parameter fitting, the yield correction factor $k(A,Z)$ for the seven isotopes are the parameters to be determined. The quantity to be minimized is

$$S = \sum_{j=1}^{9} \sum_{i} \left(\frac{T_i - T_{0j}}{\sigma_i} \right)^2 + W \left(T_{0j=9} - T_0(MSU) \right)^2 , \tag{82}$$

where i is corresponding to all the ratio combinations with $\delta B > 5$. j is the suffix of each reaction. $j = 9$ means the MSU results. W is constraint parameter which is indispensable to get close T_0 value for MSU [88] to the corresponding excited state temperature $T_{ex} = 4.0 \pm 0.4MeV$. W has been determined in order to get the most sharp temperature distribution within the constraint of $4.0 - 0.4 \leq T_0(MSU) \leq 4.0 + 0.4$. There are strong correlation between W and T_0, and between W and $Width$;

$$Width = \sum_{j=1}^{9} \sum_{i} \left(\frac{T_i - T_{0j}}{\sigma_i} \right)^2 . \tag{83}$$

As shown in Fig.68, we must use very small values of T_0 comparing to $T_{ex} = 4.0 \pm 0.4MeV$, in order to get the smallest $Width$. Using non-zero value of W, we can get acceptable $T_0(MSU)$ value. Considering the lower limit of $T_0(MSU)$, W has been determined as $W = 500MeV^{-2}$. Typical fitted results are listed in Tab.13.

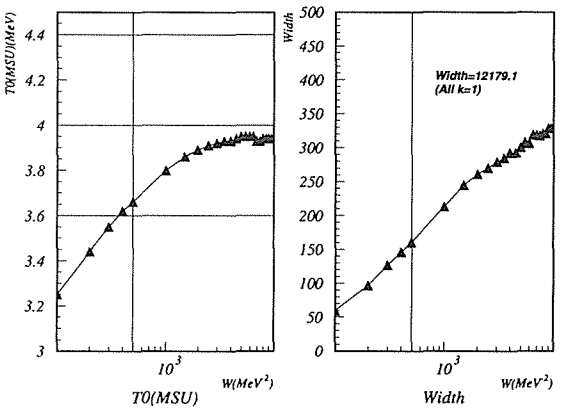

Figure 68: W dependence of $T_0(MSU)$ and $Width$

5.5.3 Fitting Results

After the parameter fitting, sharp distribution of corrected temperatures are obtained as shown in Fig.69 and Fig.70.

The existence of the remaining fluctuation of the corrected temperature distribution may imply that there are another origin of the yield distortion in addition to the common yield distortion.

The common correcting factor $k(A, Z)$ should be not common in a strict sense because of the different freeze out temperatures. It is because the $k(A, Z)$ strongly depend on the excited state population distributions, which may depend on the freeze out temperature. Considering the fact that there are some reactions which have very sharp corrected distribution, the large remaining

W	^6Li	^7Li	^8Li	^9Li	^9Be	^{10}Be	$Width$	$T_0(MSU)$
10000	0.27	0.20	0.11	0.045	0.10	0.40	328	3.94
5000	0.21	0.14	0.065	0.024	0.092	0.28	301	3.95
1000	0.16	0.11	0.060	0.024	0.095	0.31	213	3.80
500	0.26	0.20	0.12	0.053	0.11	0.39	161	3.66
100	0.15	0.11	0.079	0.040	0.091	0.33	59.4	3.25
0	2.8×10^{-6}	1.0×10^{-5}	1.2×10^{-3}	0.050	0.025	0.21	1.5×10^{-4}	0.882

Table 13: Obtained yield correction factors $k(A, Z)$ for various $W(MeV^{-2})$. The listed factors are normalized with $k(^7Be) = 1$.

$W(MeV^{-2})$	$12GeVp + A^a$				$8GeVp + A^b$			FNAL[c]	MSU[d]	Width
	Au	Tm	Sm	Ag	Au	Sm	Ag			
10000	3.93	4.74	6.28	5.35	4.69	6.79	6.50	5.23	3.94	328
5000	3.96	4.73	6.30	5.38	4.71	6.90	6.52	5.24	3.95	301
1000	3.84	4.49	6.00	5.19	4.51	6.57	6.17	5.06	3.80	213
500	3.72	4.27	5.70	4.97	4.32	6.24	5.85	4.85	3.66	161
100	3.34	3.67	4.85	4.34	3.77	5.30	4.93	4.24	3.25	59.4
0	0.909	0.920	0.995	0.968	0.931	1.02	0.981	0.962	0.882	0.00015
No Correction	4.09	4.10	5.52	5.15	4.54	4.80	5.63	4.96	3.53	12179

Table 14: (a),(b): KEK results are deduced using the isotope yields which are estimated for $\theta_{LAB} = 34°$.
(c): FNAL result ($80GeV/c\ p + Xe$, $\theta_{LAB} = 34°$) [18].
(d) : MSU result ($35AMeV\ N + Ag$, $\theta_{LAB} = 38°$) [77].
T_0 for MSU is forced to be around $4.0 \pm 0.4MeV$.

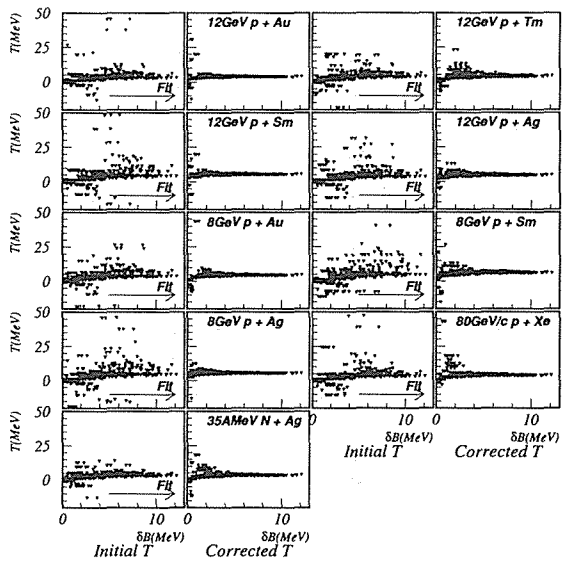

Figure 69: Correction results on the nine reactions. Left frames show the temperature distributions of before the corrections, plotted as functions of δ_B. The right frames shows the results of after the correction.

	^6Li	^7Li	^8Li	^9Li	^7Be	^9Be	^{10}Be
$k(A,Z)$	0.25	0.19	0.12	0.052	1	0.11	0.39

Table 15: Obtained yield correction factors for each isotope. $k(A,Z)$ is normalized as $k(^7Be) = 1$.

fluctuation for some other reactions must be caused by a systematic error in the yield estimation. The fluctuation of the corrected temperature distribution can not be disappeared even using non-common $k(A,Z)$. It means that a width of the corrected temperature distribution can be treated as a reliability of the experimental data. The width

$$RMS = \sqrt{\sum_{\delta B_i > 5MeV} (T_i - \overline{T})^2 / \sum_{\delta B_i > 5MeV}} \tag{84}$$

for each reactions are listed in the Tab.15. The most probable temperatures T_0 for the each reaction are also listed in the Tab.16. Here T_i means the extracted temperatures corresponding to each ratio combinations obtained by corrected $Y_0(A,Z) = Y(A,Z)/k(A,Z)$. The summation is performed only for such combinations that $\delta B > 5MeV$.

In order to define a single thermometer which can present the temperature close to the T_0, one combination which has the largest $\delta B = 12.1MeV$ is selected. For this combination, R, α, B in

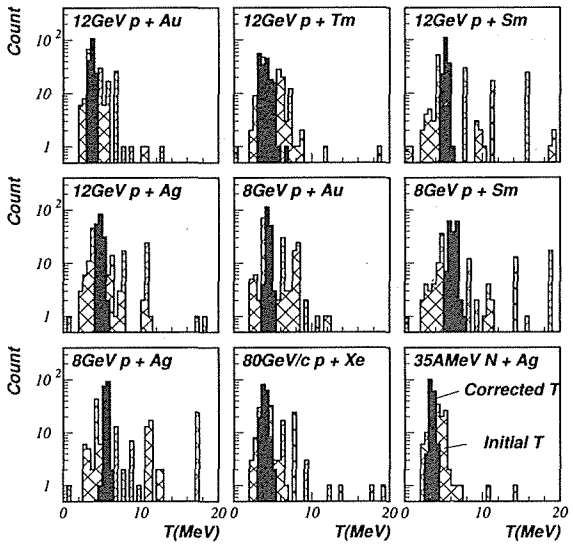

Figure 70: Correction results on the nine reactions. Resultant temperature distributions are shown for before and after the correction.

	$8GeVp + A^a$			$12GeVp + A^b$				FNAL[c]	MSU[d]
	Au	Sm	Ag	Au	Tm	Sm	Ag		
T_0	4.1	5.9	5.8	3.6	4.3	5.3	5.0	4.8	3.6
RMS	0.30	0.44	0.20	0.21	0.66	0.29	0.36	0.34	0.26

Table 16: The most probable temperatures $T_0(MeV)$ and standard deviations of temperature distributions $RMS(MeV)$.
[a,b]Present results estimated for $\theta_{LAB} = 34°$.
[c]FNAL result (80-350 GeV/c $p + Xe$, $\theta_{LAB} = 34°$) [18].
[d]MSU result (35 MeV/nucleon $N + Ag$, $\theta_{LAB} = 38°$) [77].
T_0 for MSU is forced to be around 4.0±0.4 MeV.

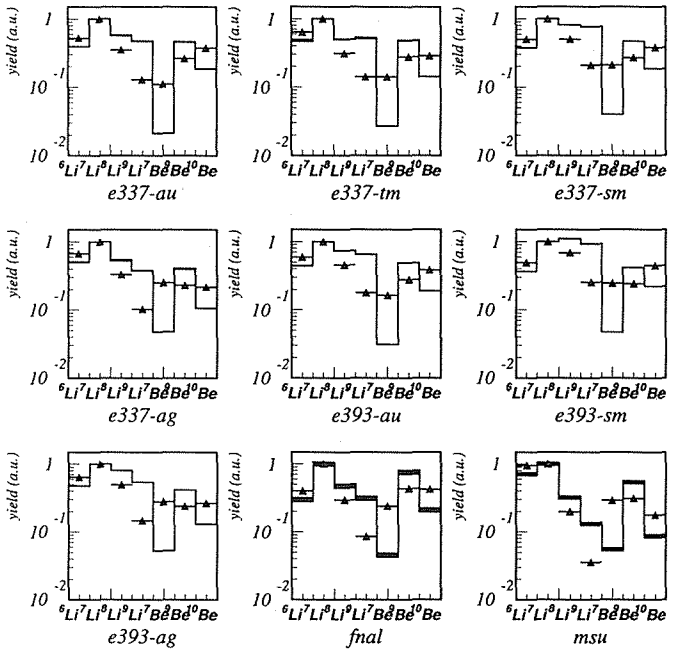

Figure 71: Isotope yield distribution of before correction (triangle points) and after correction (histograms).

Eq.65 can be written as below.

$$
\begin{aligned}
R &= \left(\frac{Y_0(^9Li)}{Y_0(^7Li)}\right)\left(\frac{Y_0(^{10}Be)}{Y_0(^9Li)}\right)^{-2}\left(\frac{Y_0(^7Be)}{Y_0(^7Li)}\right)^2 \\
&= \frac{Y_0(^9Li)^3 Y_0(^7Be)^2}{Y_0(^7Li)^3 Y_0(^{10}Be)^2} \qquad (85) \\
B &= [B(^9Li) - B(^7Li)] - 2[B(^{10}Be) - B(^9Li)] + 2[B(^7Be) - B(^7Li)] \\
&= -36.44MeV \qquad (86) \\
\alpha &= \{\left(\frac{9}{7}\right)^{\frac{2}{3}}\left(\frac{\lambda_{TN}^3}{2}\right)^2\frac{\omega(^9Li)}{\omega(^7Li)}\}\cdot\{\left(\frac{10}{9}\right)^{\frac{2}{3}}\left(\frac{\lambda_{TN}^3}{2}\right)\frac{\omega(^{10}Be)}{\omega(^9Li)}\}^{-2}\cdot\{\frac{\omega(^7Be)}{\omega(^7Li)}\}^2 \\
&= 17.01(gs), \qquad (87)
\end{aligned}
$$

here α is estimated considering only ground states into the partition function $\omega(A,Z)$. Then the nuclear temperature for this selected combination "T_{LiBe}" can be simply obtained.

$$T_{LiBe} = -36.44MeV/ln\left(\frac{Y_0(^9Li)^3 Y_0(^7Be)^2}{Y_0(^7Li)^3 Y_0(^{10}Be)^2}/17.01\right) \qquad (88)$$

One can estimate nuclear temperature using Eq.88 that will reproduce almost same value as the most probable temperature T_0 without the complicated procedure. The difference between T_0 and the selected thermometer T_{LiBe} can be found on Fig.72 and Fig.73. In Fig.72, angular distribution of T_0 are shown in Fig.73, and that of T_{LiBe} are plotted. They are very similar with each other. The δB for this case can be calculated as below.

$$\delta B = \frac{|B|}{\sqrt{1+2^2+2^2}} = 12.15 MeV \tag{89}$$

In addition, we can calculate free proton density and free nucleon density using Eq.54 for this combination. They can be obtained using the two single ratios in the combination as below. As mentioned before, there are additional possibility to select the two single ratios from the above three ratios.

Free proton density ρ_{pF} can be written as;

$$\begin{aligned}\rho_{pF} &= \frac{2}{\lambda_{TN}^3}\frac{Y_0(^{10}Be)}{Y_0(^9Li)}\left(\frac{9}{10}\right)^{2/3}\frac{\omega(^9Li)}{\omega(^{10}Be)}exp\left(\frac{-B(^{10}Be)+B(^9Li)}{T}\right)\\ &= \frac{2}{\lambda_{TN}^3}\frac{Y_0(^{10}Be)}{Y_0(^9Li)}\left(\frac{9}{10}\right)^{2/3}exp\left(\frac{-19.12MeV}{T}\right)\end{aligned} \tag{90}$$

or

$$\begin{aligned}\rho_{pF} &= \frac{2}{\lambda_{TN}^3}\frac{Y_0(^7Be)^2}{Y_0(^7Li)^2}\frac{Y_0(^9Li)}{Y_0(^7Li)}\left(\frac{7}{9}\right)^{2/3}\frac{\omega(^7Li)}{\omega(^7Be)}\frac{\omega(^7Li)}{\omega(^9Li)}\\ &\quad exp\left(\frac{-B(^9Be)+B(^7Li)-2B(^7Be)+2B(^7Li)}{T}\right)\\ &= \frac{2}{\lambda_{TN}^3}\frac{Y_0(^7Be)^2}{Y_0(^7Li)^2}\frac{Y_0(^9Li)}{Y_0(^7Li)}\left(\frac{7}{9}\right)^{2/3}exp\left(\frac{-1.8MeV}{T}\right)\end{aligned} \tag{91}$$

and free neutron density ρ_{nF} can be written as;

$$\begin{aligned}\rho_{nF} &= \frac{2}{\lambda_{TN}^3}\left[\frac{Y_0(^9Li)}{Y_0(^7Li)}\left(\frac{7}{9}\right)^{2/3}\frac{\omega(^7Li)}{\omega(^9Li)}exp\left(\frac{-B(^9Li)+B(^7Li)}{T}\right)\right]^{1/2}\\ &= \frac{2}{\lambda_{TN}^3}\left[\frac{Y_0(^9Li)}{Y_0(^7Li)}\left(\frac{7}{9}\right)^{2/3}exp\left(\frac{-6.1MeV}{T}\right)\right]^{1/2}\end{aligned} \tag{92}$$

or

$$\begin{aligned}\rho_{nF} &= \frac{2}{\lambda_{TN}^3}\frac{Y_0(^{10}Be)}{Y_0(^9Li)}\frac{Y_0(^7Li)}{Y_0(^7Be)}\left(\frac{9}{10}\right)^{2/3}\frac{\omega(^9Li)}{\omega(^{10}Be)}\frac{\omega(^7Be)}{\omega(^7Li)}\\ &\quad exp\left(\frac{B(^{10}Be)-B(^9Li)-B(^7Be)+B(^7Li)}{T}\right)\\ &= \frac{2}{\lambda_{TN}^3}\frac{Y_0(^{10}Be)}{Y_0(^9Li)}\frac{Y_0(^7Li)}{Y_0(^7Be)}\left(\frac{9}{10}\right)^{2/3}4\cdot exp\left(\frac{-16.97MeV}{T}\right).\end{aligned} \tag{93}$$

It will be discussed in Sec.6. In Sec.6, most probable values of the free nucleon densities are treated as same as for the T_0 estimation discussed in this section. If we want to obtain a value of free nucleon density without calculating all the available combinations, above formula can be used as well as for the temperature estimation.

	E337				E393		
	Au	Tm	Sm	Ag	Au	Sm	Ag
inclusive	6.22 %	15.26 %	5.19 %	7.39 %	8.28 %	7.83 %	3.95%
Multiplicity=2	6.61 %	16.47 %	5.27 %	9.98 %	7.67%	7.83%	5.25%
Multiplicity=3	5.86 %	15.26 %	11.41 %	11.77 %	7.38%	8.64%	7.40%

Table 17: Resultant total errors (statistical error + systematic error) in the final results of isotope temperature, obtained by the RMS values.

5.6 Extracted Temperature

5.6.1 Angular Distribution

Angular distributions of the obtained temperature T_0 are shown in Fig.72. The RMS value has been used as systematic error. The typical error bar (RMS) is shown in the same figure. RMS of the corrected temperature distribution for the high multiplicity events are also obtained as same as for the inclusive data.

We performed complete "deformed moving source model" fitting on the energy spectra of all isotopes in order to make yield estimation, so angular distributions can be obtained as continuous functions of emission angle. The results are shown in Fig.72 with IMF-multiplicity selection. Here IMF-multiplicity = 2 or 3 means that there were 2 or 3 counter hits in the P10 gas operation mode. In Fig.72, anisotropic "U-Shape" angular distributions are observed for temperature distribution. There are small IMF-multiplicity dependences on the temperature distributions. The global shape of the angular distribution has small ratio selection dependences at least for large δB combinations. We noted a little earlier that the shape differences between the angular distributions of the isotope yields should give anisotropic angular distribution of the temperature. The results shown in Fig.72 agree with the expectation.

Turning now to discuss about angular distribution and origin of the sideward peaking of the fragment emission. The anisotropic angular distributions of the temperature and the density imply that the chemical freeze out have been established before the total remnant reached to thermal equilibrium. What must be noticed is that even forward channels show high temperatures as well as backward channels. One explanation may be that, this is the trace of fire ball which penetrate the target nuclei with the projectile. If we suppose the penetrating picture, U-Shape of temperature and free nucleon density, and also sideward peaking fragment density can be expected as a natural consequence. It must be noted that there is an assumption in the isotope temperature method that the fragment density at the chemical equilibrium should be proportional to the experimental yields ($\rho_1/\rho_2 = Y_1/Y_2$). Therefore, the sideward peaking of the isotope density have been put into the calculation. In spite of the assumption, shape difference of the angular distribution of the isotope yields are indispensable to get anisotropic angular distribution of the temperature and the density. The U-Shape angular distribution prove clearly that there are anisotropic temperature and density distribution in the fragment emission source, and that the fragment density distribution must be the origin of the sideward yield enhancement of the fragments.

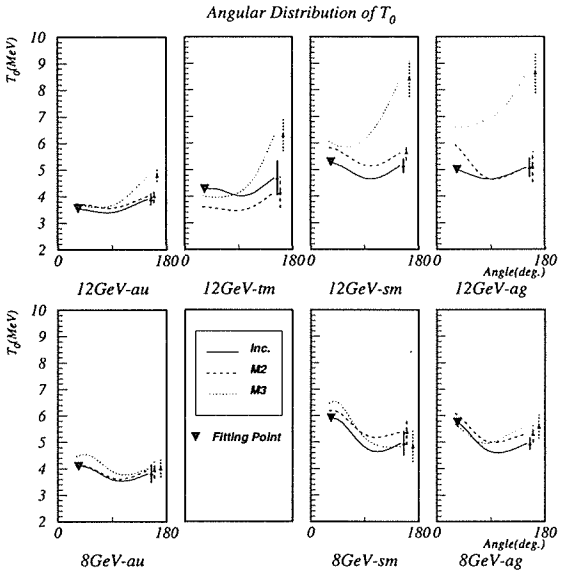

Figure 72: Obtained angular distributions of T_0.

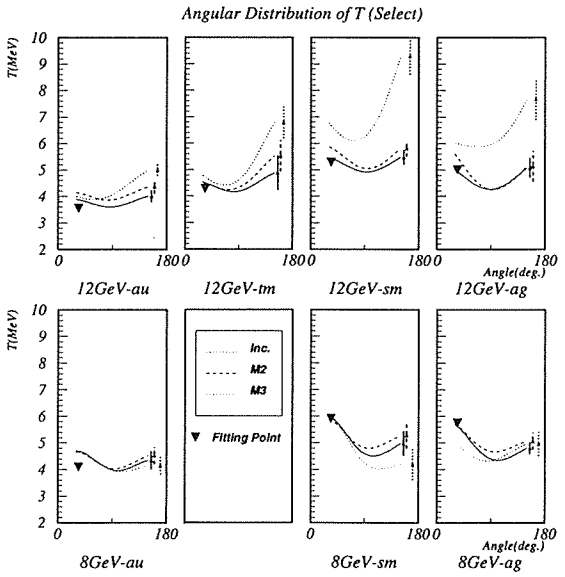

Figure 73: Obtained angular distribution of T_{select}.

5.6.2 Target Mass Dependence

Target dependence of the obtained nuclear temperatures can be found in Fig.72. Absolute values of them seem to have an tendency that higher temperature are produced in the lighter target reaction. Although there observed target mass dependences, the "A-dependence" can not be recognized as a clear correlation. It is because the A-dependences are not clear in the inclusive condition, and because the observed temperatures for the silver target reactions are not always higher than any other targets. Any way the tendency to have higher temperature at lighter target reactions can be understood considering the shared deposited energy on the target nuclei. Deposited energy can be considered to be roughly proportional to the penetrating path length of the incident proton. Then the mean energy density in the residual nuclei can be obtained for a central collision as below.

$$\rho_E = \frac{length}{Volume} = \frac{r_0 A_t^{1/3}}{4\pi r_0^3/3 A_t} \propto A_t^{-2/3} \tag{94}$$

The observed A-dependence can not be recognized as a simple correlation written as Eq.94. However, the global tendency can be understood qualitatively using Eq.94. Of course Eq.94 represents a relation between the target mass and the mean energy density, thus A-dependence of the temperature can not be obtained straightforwardly. Considering the caloric curve, the relation between temperature and energy density can be written as below.

$$\begin{aligned} T &\propto \sqrt{\rho_E}\,(LiquidPhase) \\ T &\propto const.\,(MixedPhase) \\ T &\propto \rho_E\,(GasPhase) \end{aligned} \tag{95}$$

Considering Eq.95, A-dependence may be small if the nuclei can be recognized as in liquid-gas mixed phase. In order to make detail discussion on this topics, energy density estimation is indispensable.

5.6.3 Beam Energy Dependence

As for beam energy dependence, it can also be found in Fig.72. Because of the existence of angular dependence and IMF-multiplicity dependence, the relation between the beam energy and the obtained nuclear temperature is not clear. There are two facts which can be found in Fig.72 as beam energy dependences.

1. IMF-multiplicity dependences for the light target reaction at $E_p = 12GeV$ is strong.
2. Shape of U-Shape the angular distribution is not same for different beam energy.

High IMF-multiplicity selection means very high temperature event selection for $E_p = 12GeV$, on the other hand, there are small IMF-multiplicity dependence at $E_p = 8GeV$. Deposited energy should be larger for higher beam energy reaction, therefore, higher temperatures should be observed at higher beam energy reactions in a nuclear gas phase. The small beam energy dependence except for light target reaction can be explained as a results of plateau in the caloric curve.

5.6.4 IMF Multiplicity Dependence

As pointed out in the previous section, there are small IMF-multiplicity dependence for $E_p = 8GeV$ reaction, on the other hand, strong IMF-multiplicity dependences have been found at $E_p =$

$12GeV$. IMF-multiplicity have been recognized as a prove for the impact parameter on the collision. On this assumption, deposited energy should be larger for higher IMF-multiplicity events than that of lower IMF-multiplicity events. However, IMF-multiplicity dependence can be found only at light target reaction with $E_p = 12GeV$. Possible reason why there are small IMF-multiplicity dependences may be following;

1. Temperatures have small impact parameter dependences. That is to say, there are small energy density dependences for the temperatures.
2. The correlation between IMF-multiplicity and impact parameter, or between IMF-multiplicity and energy density is weak.

The first possibility can be understood if they are in liquid-gas mixed phase. In the mixed phase, energy density dependence on the temperature is flat. For the second possibility, there are no way to check the correlation in this experimental data. It will be a subject of a simulation study. The second possibility do not contradict with almost all the experimental results, except for light target reaction at $Ep = 12GeV$ where strong IMF-multiplicity are found.

6 Density

6.1 Density Evaluation

In order to study the property of the nuclear matter, it is very fruitful if we can make density estimations as well as the nuclear temperature. As introduced in Sec.5, fragment density can be estimated using the three parameters (T, ρ_{pF}, ρ_{nF}). In Sec.5, isotope temperatures are deduced with some correlations. Remaining two parameters of free proton and neutron density (ρ_{pF}, ρ_{nF}) can also be obtained at the same time. Although it is possible to estimate not only the temperature but also the free nucleon density, there have been no experimental study on extracting free nucleon density after the publication of caloric curve in 1995 by J. Pochodzalla et al.[89] except of the present study. It is because using those single ratios of

$$\Delta Z = 0, \tag{96}$$

we cannot extract free proton density ρ_{pF}(Eq.54). It is also impossible to extract free neutron density ρ_{nF} using those single ratios of

$$\Delta(A - Z) = 0. \tag{97}$$

In order to obtain these yield ratios between $\Delta Z \neq 0$ isotopes, determination of the shape of the energy spectra is indispensable. Performing complete deformed moving source model fitting, we can obtain such single yield ratios.

If we got T, ρ_{pF}, ρ_{nF}, density of any fragments at the chemical freeze out can be estimated using Eq.55. In the following sections, free nucleon density will be estimated at the first, then fragment density will be discussed at the later.

6.1.1 Original Density Estimation

The isotope temperature method has been widely used in temperature measurements, on the other hand, it seems to fail in the evaluation of the nuclear densities. It is because the obtained

densities seem to have one order smaller value than expected [74], comparing to the results of some theoretical calculations [130], and the experimental results measured by particle correlation methods [131]. The original evaluation of the nucleon density is described in Eq.54. Using Eq.54 with the obtainted values of the temperatures, free nucleon density can be estimated. As discussed in Sec.5, there is an ambiguity on selecting two single ratios from the selected three single isotope yield ratios (Eq.72).

$$\rho_{pF}(i,j) = \frac{2}{\lambda_{TN}^3}[(\frac{R_i}{\alpha_i})^{\xi_j}(\frac{R_j}{\alpha_j})^{\xi_{-i}} exp(\frac{\Delta B_j \xi_i - \Delta B_i \xi_i}{T})]^{\frac{1}{\eta_i \xi_j - \eta_j \xi_i}} \tag{98}$$

$$\rho_{nF}(i,j) = \frac{2}{\lambda_{TN}^3}[(\frac{R_i}{\alpha_i})^{\eta_j}(\frac{R_j}{\alpha_j})^{\eta_{-i}} exp(\frac{\Delta B_j \xi_i - \Delta B_i \xi_i}{T})]^{\frac{1}{\xi_i \eta_j - \xi_j \eta_i}} \tag{99}$$

for $(i,j) = (1,2),(2,3),(3,1)$. The mean values of the additional combinations are calculated as the free nucleon density for the each ratio combination selected for the temperature evaluation.

$$\bar{\rho}_{pF} = (\rho_{pF}(i,j) + \rho_{pF}(j,k) + \rho_{pF}(k,i))/3 \tag{100}$$

$$\bar{\rho}_{nF} = (\rho_{nF}(i,j) + \rho_{nF}(j,k) + \rho_{nF}(k,i))/3 \tag{101}$$

In the density calculation, the mean value of the available three combination patterns $\bar{\rho}_{pR}$, $\bar{\rho}_{nR}$ are used as results. Therefore, there are same number of combinations to extract $\bar{\rho}_{pF}$ and $\bar{\rho}_{nF}$ as extracting temperatures. In Fig.76, Fig.77, Fig.78, "most probable densities" are shown. The definition of the most probable free proton density D_{p0} and free neutron density D_{n0} are

$$\begin{aligned} D_{p0} &= \frac{\sum_i \bar{\rho}_{pFi}/\sigma_i^2}{\sum_i 1/\sigma_i^2} \\ D_{n0} &= \frac{\sum_i \bar{\rho}_{nFi}/\sigma_i^2}{\sum_i 1/\sigma_i^2}, \end{aligned} \tag{102}$$

and the free nucleon density D_0 is

$$D_0 = D_{p0} + D_{n0}. \tag{103}$$

The summation is performed as same as in extracting the most probable temperature T_0 in Eq.80. As shown in Fig.76, Fig.77 and Fig.78, the obtained free nucleon densities are very small comparing to the normal nuclear matter density ρ_0.

6.1.2 Nuclear Binding Energy Variation Effects

In the original configuration, nuclear binding energies in the free space are used in the calculation as the binding energies of produced fragments. However, at the freeze out stage, external nuclear bath all around the fragments should be changed its binding energy because of the nucleus surface energy can be very different than in the standard situation. According to S. Albergo, the effect of the binding energy variation in the matter can be described as following [132].

$$B(A,Z)' = B(A,Z) - \Delta W_{surf} \tag{104}$$

Here $B(A,Z)$ is binding energy of a nucleus (A,Z) in the free space and $B(A,Z)'$ is the modified binding energy. ΔW_{surf} is a surface energy variation,

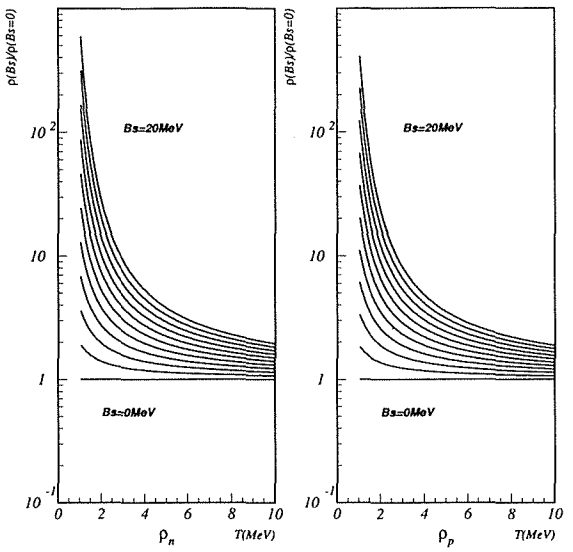

Figure 74: Binding energy variation effects are plotted as a functions of temperature. We cannot expect a large improvement at high temperatures.

$$\Delta W_{surf} = b_s A^{2/3} \tag{105}$$

where b_s is a parameter depending only on the density of the external nuclear matter ρ_S. Since ρ_S is unknown, b_s must be put as a parameter in the calculation. In the range of $0 < \rho_S < \rho_0$, b_s varies in $0 < b_s < 17MeV$. Free nucleon densities obtained using Eq.104 can be changed, while temperature is slightly affected by the variation [132]. In Fig.74, ratio between the corrected density obtained assuming $b_s > 0MeV$ and the original results are shown as functions of temperature. If the temperature were under $3MeV$, obtained free nucleon densities can be changed by orders of magnitude. On the other hand, variation effect is not large at the high temperature region.

As for the temperature, there are constraint of $T_0(MSU) = 4.0 \pm 0.4MeV$. T_0 for other reactions is strongly restricted because of the common $k(A, Z)$ (Eq.79) for the each reaction in the sequential decay correction. $T_0(MSU)$ was measured by the relative population ratio between excited states of the fragments in particle correlation method [88]. The restriction is indispensable to get probable results on the $k(A, Z)$ and T_0 fitting. As for the free nucleon density, the absolute values are very small comparing to the results of some theoretical calculation and the experimental results measured by particle correlation methods [13]. Similar small values are also reported in previous experiment [74]. The origin of the small estimated density may be lie on the isotope temperature method itself [132]. The nuclear binding energy used in the formalism may be influenced by the nuclear matter density of the surrounding medium. According to Albergo and Tricomi [132], the nuclear binding energy of each fragment $B(A, Z)$ should be replaced with $B'(A, Z)$.

We can find the effect of the binding energy variation in Figure 75. The free nucleon density obtained by $B_s = 10MeV$ has only about twice value of that for $Bs = 0MeV$ (No variation). The

effect of the variation $\rho(B_s)/\rho(B_s = 0)$ has strong temperature dependence as shown in Fig.74. They have large effects as order of magnitude for small T $(2 - 3MeV)$, on the other hand, the effect are small for $T > 5MeV$. If we set the temperature as low as $3MeV$, we could get larger density for $B_s > 0MeV$. Since the temperature reported in this paper around $5MeV$ is obtained referring the results of the particle correlation experiment [88], we cannot expect an improvement on the small density estimation. There is room for further theoretical investigation.

6.2 Free Nucleon Density

Although the absolute value might not be true, relative density discussion may be a valid argument. An example of the angular distribution of the temperature and the free nucleon densities are shown in Fig.75 with the binding energy variation.

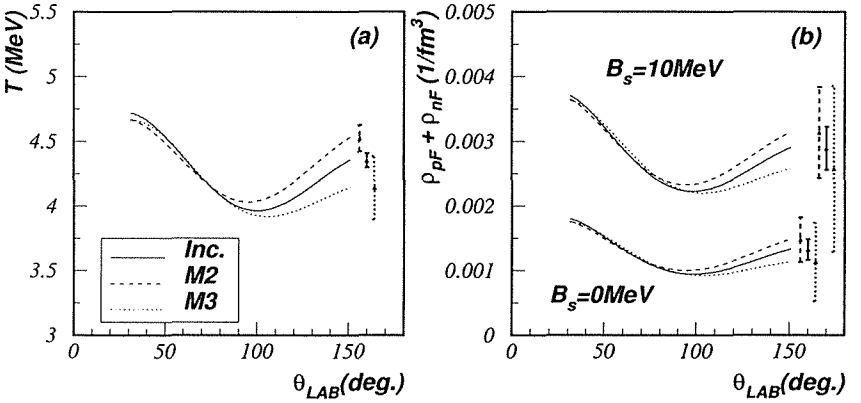

Figure 75: Temperature and free nucleon density obtained with the binding energy variation. Since there are little effect on the temperature evaluation, only the initial results are drawn for the temperature.

As shown in Fig.75, there observed angular distribution of the free nucleon densities with almost same shapes as that of the temperature. It is independent of the binding energy variation. This similarity can be understood by the correlating relation between the temperature and the free nucleon gas density. According to the starting assumption of the isotope temperature method, the considering system must be a mixed gas of fragments and free nucleons. Thus, there must be positive correlation between the temperature and the nucleon gas density. The experimental correlation will be introduced in the following section.

In Fig.76, most probable free nucleon densities $D_0 = D_{p0} + D_{n0}$ are shown as angular distributions with IMF-multiplicity selections for all the reactions. There are no binding energy variation ($B_s = 0MeV$). The global features are very similar to Fig.72. The similarity can be found not only in angular distributions but also in the target mass dependences, IMF-multiplicity dependence, and in the beam energy dependences. This general similarity can be also understood in the positive correlation between temperature and free nucleon gas density.

We should not discuss only the total free nucleon density. The free proton and the neutron density can be obtained individually in the experiment. The obtained results of D_{p0} and D_{n0} are shown in

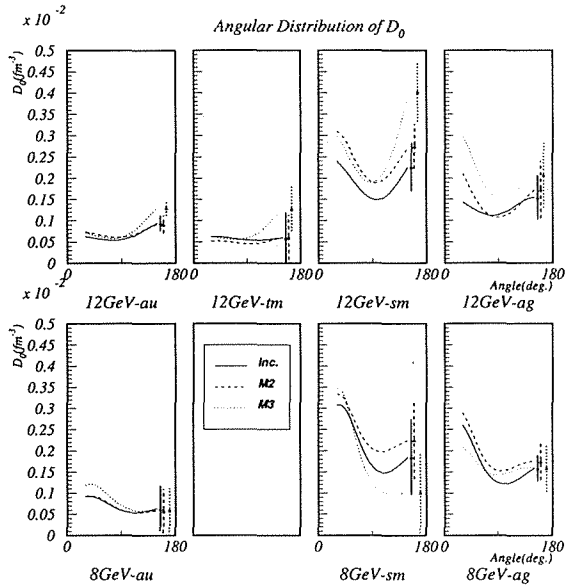

Figure 76: Obtained angular distributions of the free nucleon density.

Fig.77 and Fig.78. Here we can find the same similarity between D_{p0} and D_{n0} . The only exception is the absolute value. The ratio between D_{p0} and D_{n0} are far small from 1. It is not certain whether the obtained ratios are true or not as well as the problem of the absolute value.

6.3 Free Proton-Neutron Density Ratio

We are able to see ratio between the free proton and the neutron density $R_{pn} = \rho_{pF}/\rho_{nF}$. Obtained value of the ratio R_{pn} are about 0.15 with small angular dependences. The free proton density can be smaller than that of neutron, however, the obtained ratio should be more close to 1. It needs further consideration on the procedure too. Resultant R_{pn} seems to have target mass dependences. R_{pn} has tendency to show lager value in the light target reactions, where high temperature and large free nucleon density are expected. N/Z ratio of the target can partially explain the target mass dependence on R_{pn}. It is because the ratio between the proton number and the neutron number in the initial target nuclei should affect in the resultant free nucleon densities. On other words, the N/Z ratio of the target on the isotope temperature evaluation can influence only on the free nucleon density. It is one of the reason why isotope temperature can not be extracted from one single isotope yield ratio. Thus isotope temperature evaluated from double or multi ratio can not be affected by the initial N/Z ratio.

6.4 Temperature-Density Correlation

In the former section, the similarity between the temperature and the free nucleon densities have been pointed out. The similarity can be understood in the positive correlation between the

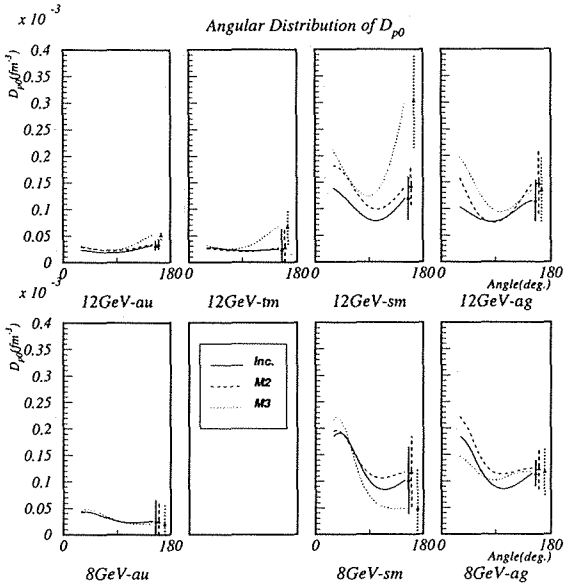

Figure 77: Obtained angular distributions of the free proton density.

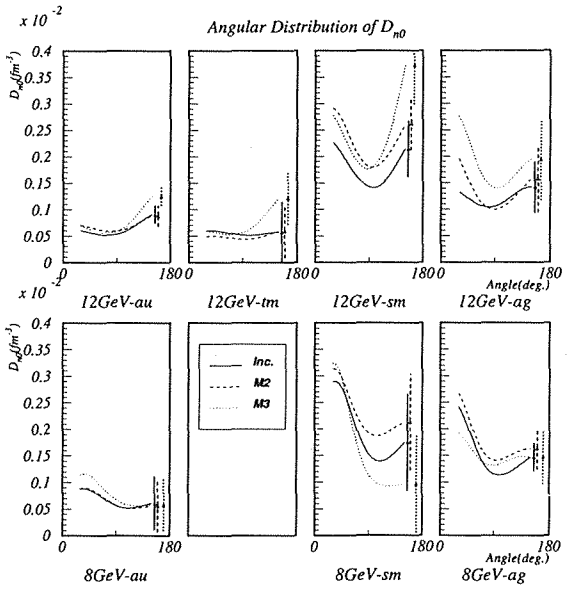

Figure 78: Obtained angular distributions of the free neutron density.

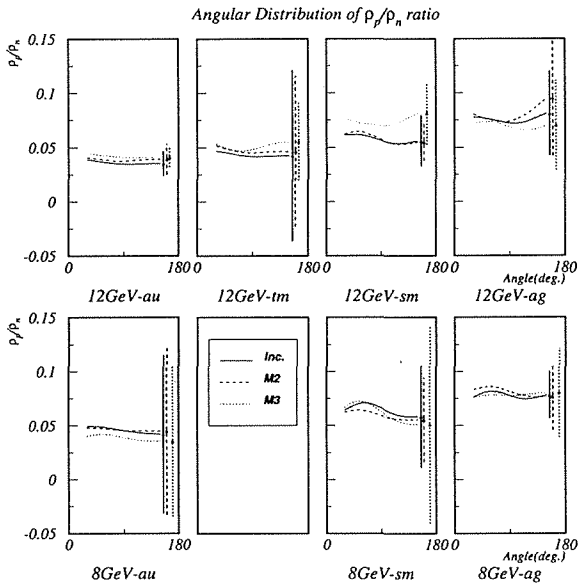

Figure 79: Free proton density vs. Free neutron density

temperature and the free nucleon densities shown in Fig.80. Fig.80 can be understood assuming the fragment-nucleon mixed ideal gas. In a relatively higher temperature condition, more nucleons should be emitted from the composite particles. And in a relatively lower temperature condition, more free nucleons should be absorbed in the fragments.

The correlation results shown in Fig.80 can be used for the test of theoretical models on dilute nuclear matter. For example, nucleon capture interaction on fragments in mixed dilute system can be studied [83]. Albergo et al. predicted in [83] that;

$$\rho_{pF} + \rho_{nF} = 5.3 \times 10^{-6} T^3 (fm^{-3}). \tag{106}$$

Eq.106 is drawn in the Fig.80 as a solid line. Although it is possible to fit the obtained correlation data between the free nucleon density and the temperature, it is not important here because of the very small absolute value of the evaluated densities. The only one point which makes sense is that, the obtained values of the free nucleon densities and the temperature agree well as the calculated results shown by Albergo's original paper. It should be noticed again, that the origin of the very small value of the free nucleon density exists in nowhere but in the original isotope temperature procedure itself. The binding energy variation effects can not make significant improvements. Further theoretical study is also needed.

6.5 Fragment Density

In the starting point of the isotope temperature procedure, we assume that any fragment density $\rho(A, Z)$ can be expressed using T, ρ_{pF} and ρ_{nF} using Eq.55, which is used in the introduction

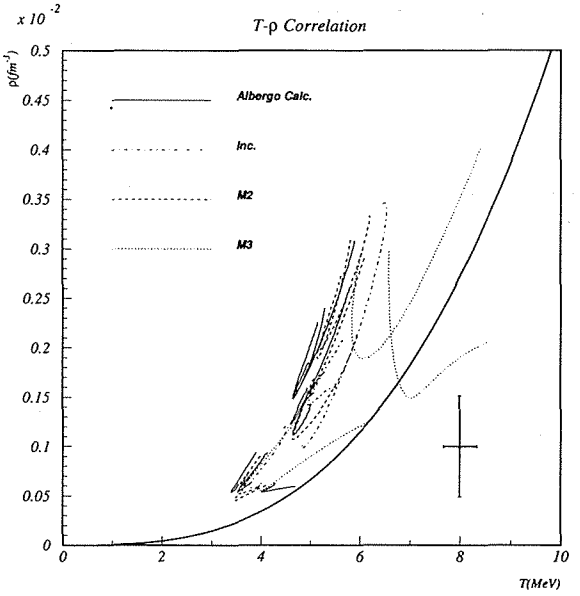

Figure 80: Free necleon density D_0 vs. Temperature T_0. All the obtained points are drawn. The solid line shows a result of the calculation by Albergo et al. [83]

of the isotope temperature procedure. Four independent isotope yield, which are assumed to be proportional to the corresponding fragment density at the chemical freeze out, can deduce T, ρ_{pF} and ρ_{nF}. Once T, ρ_{pF} and ρ_{nF} are obtained, any fragment yield can be estimated using Eq.55. Of course there are an assumption that all the fragments should be produced at the same freeze out stage. This assumption may not be able to be accepted. It is a natural consequence that a heavy fragment formation should be occurred at a relatively later time stage when the environment temperature have became enough low to bind the heavy fragment (see Sec.7). However, it is worth comparing the reproduced fragment yield and observed yield for understanding the feature of the isotope temperature method.

6.6 Nuclear Matter Density

Free nucleon density can be obtained directly in the isotope temperature evaluating process. It is also possible to estimate fragment density using the obtained temperature and free nucleon densities as an extrapolation. Nuclear matter density is an very attractive observable for studying the property of the nuclear matter. Temperature and the total nuclear matter density around the critical point for the nuclear liquid-gas phase transition can be a strong tool for determining the equation of states of the nuclear matter at the intermediate energy. After obtaining the fragment densities, nuclear matter density can be obtained as a sum of all the fragment densities.

$$\rho = \sum_A \sum_Z \rho(A, Z) \tag{107}$$

Although it is a fascinate analysis, we cannot perform the calculation. It is because the fragment density can not be obtained because of the violation of thetiming stage assumption. The main fraction of ρ is the light fragments, considering the production cross section which is considered to obey in power law.

$$\rho(A,Z) \propto A^{-\tau} \tag{108}$$

Here τ is the power law index. Typical value of the index is $\tau \sim 2.6$, which was reported by Hirsh et al.[18]. Thus a first order calculation can be performed using the results of isotope temperature procedure obtained from the relatively light fragment region. However, the remaining problem of the absolute value prevent the motivation.

6.7 Fragment Density vs. Free Nucleon Density

Although the accurate fragment density estimation can not be performed, it is possible to make qualitative discussion. The positive correlation between the free nucleon densities and the temperature shown in Fig.80 can be understood by the fragment-nucleon mixed ideal gas assumption. It is also possible to expect the "negative correlation" between the heavy fragment densities and the temperature at the same time. On other words, larger fragment densities should be obtained at smaller free nucleon gas density condition. Because of the negative correlation between temperature and fragment densities, expected angular distributions of the fragments should have opposite shapes to that of temperature, which show U-Shape angular distribution. Thus, the fragment densities may have "anti-U-Shape" angular distribution. It have already been observed. That is the sideward peaking of the IMF production. It is not need to reconstruct the angular distribution of the fragments. Because they have been put into the isotope temperature evaluation at the starting point as the fragment density. Thus, U-Shape angular distribution of the temperature and the free nucleon densities, and sideward peaking of the IMF emission is a same phenomena with different expression. After long way evaluating the isotope temperature, now it is possible to say that the anisotropy of the temperature can be an origin of the sideward peaking of the fragment emission. This is the core of the conclusion of this study. Detail discussion will be held at Sec.7.

6.8 Liquid-Gas Phase Transition with Density Probe

Search for a nuclear liquid-gas phase transition seems to be achieved in the caloric curve reported by Pochodzalla et al [89]. That may be a clear signal of the phase transition if it was made by a direct temperature measurement experiment. However, we do not have such direct thermometers. The obtained caloric curve can not be treated as a direct evidence of the nuclear liquid-gas phase transition. In order to assist the results, it is desirable to get information on another dimension. Free nucleon gas density can be such an observable. In the plateau in the caloric curve, the corresponding phase of the nuclear matter can be considered to be in the liquid-gas mixed phase. This means that at a collision timing stage, when the maximum temperature in the collision have been achieved, there must be a fragment and free nucleon mixed system. At this mixed gas phase, the temperature may not arise with the energy density. This is the plateau in the caloric curve. However, if we got the free nucleon density vs. energy density plot, the free nucleon density may not make a constant line. If the corresponding condition is the mixed phase, the free nucleon density must increase with the energy density. If the "rising" were observed, there might be no doubt on the appearance of the nuclear liquid-gas phase transition.

However, such rising of the free nucleon densities cannot be expected from the observed results on the temperature-free nucleon density correlation Fig.80. Considering some other contraction in

the results using the densities, something may be wrong in the density evaluation procedure. How the density evaluation treatment in the isotope temperature method should be modified is a question which we want to keep beyond the scope of this present work.

7 Collision Dynamics and Hot Nuclear Matter

7.1 Possible Origin of the Anisotropic Fragment Yield

As shown in Sec.4, the deformed moving source model is the best model which can fit the energy spectra including the sideward yield enhancement. In order to reproduce the sideward yield enhancement, normalizing constant N is enlarged for the sideward region without changing the shape of the energy spectra in the deformed moving source.

$$N = N(\theta^*) = N_0 + N_f exp[-\frac{(\theta^* - \theta_f^*)^2}{2\sigma_f^{*2}}] \tag{109}$$

Notations are written in Sec.4. This is a pure phenomenological treatment. Meanings of the functional form for the yield enhancement should be considered. Possible reasons which can cause the anisotropic fragment yield are listed in the following.

1. non-thermal dynamical effects
2. shadowing effects
3. anisotropic fragment formation probability

Main candidate for the origin of the dynamical effects may be a matter flow. The expected fragment yields may be enhanced at the fragment emitted angle towards the flow direction. In this case, kinetic energy of the fragment at the flow direction must be increased because of the flow velocity. This effect can be seen in Fig.46. The observed energy spectra do not show such energy spectra shift towards the high energy side at the sideward angle. This is shown in Sec.4 that the flow moving source model can not reproduce the sideward region successfully because of the energy shift effects. Although it can not completely denied the possibility of the nuclear matter flow effect on the sideward fragment yield enhancement, it is clear that the flow is not the main origin.

Nuclear shock-wave can be a driving force of the sideward flow phenomena. It is a strong candidate of the sideward peaking because of the fact, that the sideward yield enhancement has a peak around 70°. This peak angle suggests a shock-wave angle in the nuclear matter. However, expected effects on the observed fragment yield by the nuclear shock-wave should be as same as by the nuclear flow. Thus it is hard to say the nuclear shock-wave is the main origin of the sideward peaking as discussed above.

The next possibility is the shadowing effects. If there were a large heavy matter around forward direction, fragment yields should be suppressed towards the forward direction comparing to the single moving source emission. However, this idea has a difficulty that the observe fragment must have sufficiently large size comparing to the target nuclei. It is hard to suppose such condition.

If emitted fragments were broken at forward direction, fragment yields would have forward suppressed angular distributions. Only one possible breaking power is the fireball emitted towards the forward direction. It is a high energy fire ball. However, the fireball velocity and the fragment emission velocity must be very different from each other. Fragments can not effected by the fireball if the fragment velocity is significantly smaller than that of the fireball.

The last possibility is the anisotropic fragment formation probability. It is clear that if the fragment producing probability were anisotropic, anisotropic yield would be observed. Note that this possibility is an integrated possibility along the emission direction from the fragment emission center. The expected fragment formation probability $P(\theta)$ at θ can be estimated as following.

$$Y(\theta) \propto P(\theta) = \int_{center}^{surface} dl(\theta) \cdot p(\vec{r}) \tag{110}$$

The integration should be performed along the line starting from the fragment emission center to the source surface. Here $p(\vec{r})$ is the fragment formation probability at $\vec{r}$. In order to get anisotropic fragment formation probability $P(\theta)$, there are two additional possibility.

1. anisotropic $p(\vec{r})$ distribution
2. anisotropic integrating volume area
3. both of above 1. and 2.

In the first case, it is clear that the integrated fragment formation probability $P(\theta)$ may show anisotropic distribution. In the second case, the initial fragment formation probability $p(\vec{r})$ at $\vec{r}$ can be uniform, but the integrated area should be deformed. For example, if there were tunnel along the penetrating path at a central collision, forward yield and backward yield would be suppressed because of the lack of the source matter. Both possibility can be considered at the same time. In the next section, the origin of the sideward yield enhancement will be discussed on the base of deformed fragment formation probability.

7.2 Sideward Enhancement

7.2.1 Source Geometry

The most simple idea to understand the sideward peaking fragment formation probability $P(\theta)$ is the formation of a deformed fragment source matter. Toroidal-shaped source nuclear matter is one of the possible source which may reproduce the sideward peaking. It is shown that the formation of such toroidal-shaped nuclear matter is possible using a kind of Relativistic Quantum Molecular Dynamics (RQMD) by Maruyama et al. [107]. Although the calculation can not reproduce the absolute value of the fragment production cross section, it is able to treat the fragmentation process in the framework. As a result, Maruyama et al. reported that if there were toroidal-shaped nuclear matter (Case II), observed fragment yield would have sideward peaking angular distribution. On the other hand, if there were spherical-shaped fragment source (Case I), which is produced in the calculation with a different interaction parameter L than in the Case II, the resultant angular distribution of the fragment yield would have forward peaking. The results are shown in Fig.81,82, and in Fig.83. These results are obtained for 5GeV/u α induced reactions.

Time evolution of the nuclear density and the temperature are also studied with similar RQMD formalism. The results are shown in Fig.84. The results were reported by Ohtsuka et al. [133]. Although the formalism of the RQMD itself cannot probe the freeze out timing, the results confirm the deformed source matter formation.

In spite of the great progress in studying GeV proton induced reactions, quantitative explanation of the multifragmentation has not been succeeded. The main theoretical difficulties lay on the large gap of the energy scale between the collision dynamics (GeV) and the nuclear fragmentation (MeV).

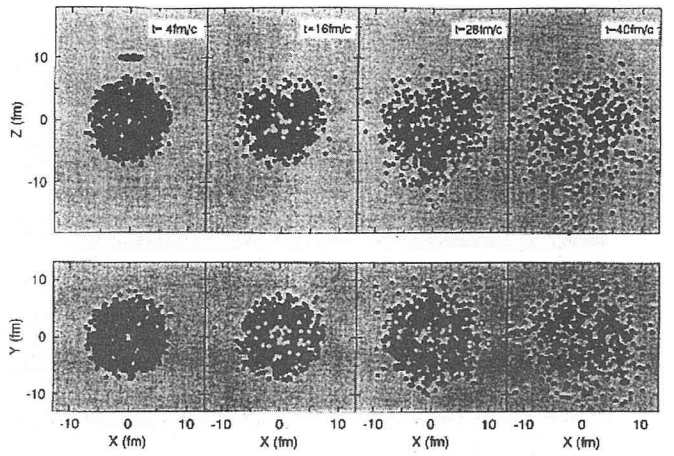

Figure 81: (Case I). Time evolution of the baryon and meson distributions in the coordinate space at time steps 4, 16, 28 and 40 fm/c in α (5GeV/u) + Au collisions for the impact-parameter $b = 0$ fm. The upper display the distributions in the xz-plane, restricted by $|y| < 1$ fm, while the lower columns in the xy-plane, restricted by $|z| < 1$ fm. The black, grey and white circles denote the nucleons, resonances and mesons, respectively. In this case, interaction width parameter is defined by $L = 1.301$ fm.

7.2.2 Fragment Formation Probability

In Sec.5 and Sec.6, "U-Shaped" angular distribution of the temperature and the free nucleon densities are shown. The positive correlation between the temperature and the free nucleon densities are also obtained. The starting assumption of the isotope temperature is the chemical and the thermal equilibrated free nucleon and fragment mixed ideal gas as shown in Fig.85. It is clear that in a high temperature system, many nucleons may be exist as free nucleons. At the same time, fragment density must be decreased at such high temperature condition. It is almost same as in the system of water and vapor. At the low temperature conditions, there may be little vapor and a lot of liquid water. On the other hand, a lot of vapor and little water may be found in high temperature condition. It is natural, therefore, that the fragment densities must be large at low temperature and small free nucleon densities. Thus, following statement would be correct.

- U-Shape angular distribution of T, ρ_{pF} and ρ_{nF}
  $\Leftrightarrow$ Sideward peaking angular distribution of the fragment densities

In Fig.86, one example of a resultant angular distribution of a fragment density reconstructed by observed U-Shape temperature and free proton and neutron densities using Eq.107, selecting heavy fragments. In this figure, clear sideward peaking is confirmed, however, it cannot be reconstructed for all the fragments. Although qualitative relation between sideward peaking and U-Shape temperature and free nucleon densities may be accepted, quantitative confirmation of the equivalence have not been completed at this time.

Although it is not possible to obtain direct results of the fragment densities, the expected angular distribution must have sideward peaking shape. It is because the sideward peaking is not a result,

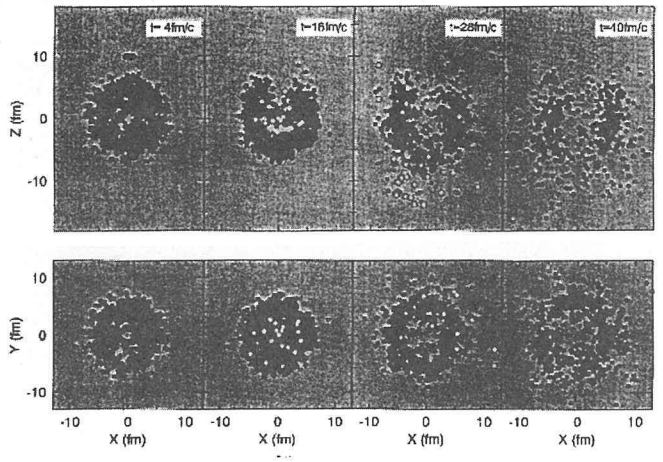

Figure 82: (Case II). Formation of a"nuclear donuts" can be found. In this case, interaction width parameter is defined by $L = 0.884$ fm, which is smaller than in the Case I.

but the input experimental information. Remind that the assumption

$$Y(A, Z) \propto \rho(A, Z) \tag{111}$$

in the isotope temperature procedure. The observed U-Shape can not obtained only by the sideward peaked fragment yield itself, but by the fine shape differences between the different isotopes. The shape differences between the isotopes shown in Fig.113, 114, 115, 116, 117, 118, 119 are explained in the anisotropic angular dependence of the fragment formation temperature. Obtained U-Shape angular distribution of the temperature re-confirm the explanation.

The relation between the observed fact and output information is very confused in the logic discussed here. A simple logic chart is shown in Fig.91.

7.3 Caloric Curve

7.3.1 Nuclear Stopping Power

In order to understand the beam energy dependence, target mass dependence, IMF-multiplicity dependence, and the angular dependence on the estimated temperature, qualitative discussion can be made by a deposited energy density estimation. Deposited energies can not be determined directly using the experimental data. In order to estimate the deposited energy on the residual target, results of theoretical calculation on the proton-nucleus interaction is used. According to Cugnon [134], energy loss in proton-nucleus collision can be estimated using the inter-nuclear cascade model (INC). Incident proton beam energy dependence of the energy loss is shown in Fig.92 for a central p+Au and a p+Ca reaction. There are points corresponding to the total energy loss and to the energy loss

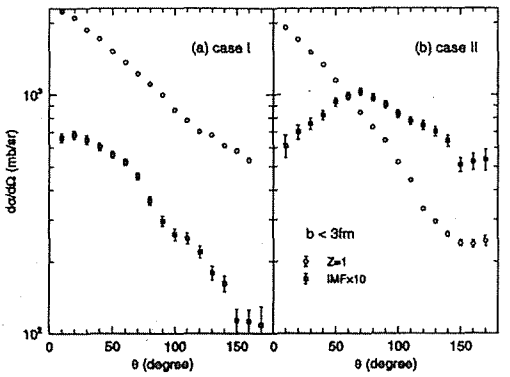

The angular-distributions of fragments for cases I (a) and II (b): $Z = 1$ (open circles) and $3 \leq Z \leq 20$ (full squares). The cross-section for the second fragment is multiplied by 10. Events are restricted to those satisfying $b < 3$ fm.

Figure 83: Resultant angular distribution of IMFs for (Case I) and (Case II): $Z = 1$ (open circles) and $3 \leq Z \leq 20$ (full squares). The cross section for the second fragment is multiplied by 10. Events are restricted to those satisfying $b < 3$ fm. Forward peaking is obtained for the case of spherical source formation (a). Case I. On the other hand, the sideward peaking is confirmed in the case of "nuclear donuts" formation (b) Case II.

which is not used to create pions. At least in the 1-10 GeV range, the energy loss obeys more or less the following law

$$\Delta E = a + b \cdot lnE. \tag{112}$$

Incident energy dependence of the energy loss ΔE shown in Fig.92 are fitted using Eq.112 for 1-10GeV. The fitted results are also shown in the Fig.92. Nuclear stopping power can be obtained by following relation using the ΔE and the target radius.

$$-dE/dX = \Delta E/2R_t, \tag{113}$$

where R_t is the target radius. According to J. Cugnon, the nuclear stopping power dE/dX has small target mass dependence. Therefore, dE/dX can be estimated as the mean value between dE/dX on the p+Au and the p+Ca reaction.

$$-dE/dX = \left(\frac{\Delta E(p+Au)}{2R_t(Au)} + \frac{\Delta E(p+Ca)}{2R_t(Ca)} \right) /2 \tag{114}$$

Incident energy dependence on the obtained nuclear stopping power are plotted in Fig.93. In this case, energy deposition on the fragment source should not contain the energy for creating pions. As a result, energy deposition on the fragment source can be estimated with the following relation.

$$-dE/dX(MeV/fm) = 48.9 + 42.9 \cdot lnE \tag{115}$$

Using Eq.115, nuclear stopping power for p+A reaction at $Ep = 8GeV$ and $12GeV$ are estimated as

$$\begin{aligned} -dE/dX(Ep = 8GeV) &= 138.0MeV/fm \\ -dE/dX(Ep = 12GeV) &= 155.0MeV/fm. \end{aligned} \tag{116}$$

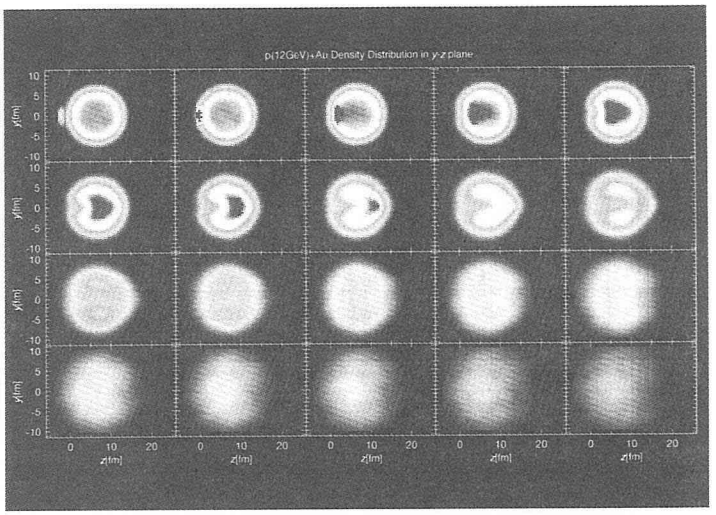

Figure 84: Time evolution of the nuclear density in 12GeV p+Au reaction. Reported by Ohtsuka et al.[133].

Considering the fact that the nuclear stopping power should be independent on the incident proton energy above $Ep > 10GeV$, dE/dX at $Ep = 12GeV$ should be replaced with the value for $Ep = 10GeV$. Thus,

$$-dE/dX(Ep = 12GeV) \sim -dE/dX(Ep = 10GeV) = 147.6MeV/fm \tag{117}$$

will be used as the nuclear stopping power at $Ep = 12GeV$ in the following discussions. Total energy deposition on the residual target are estimated with Eq.116 and the penetrating pass length in the target.

Using Eq.116, we can estimate the total deposited energy ΔE onto the target nuclei. For central collisions, ΔE have obtained as shown in Tab.18. If the total target nuclei were the spectator, mass of the fragment source could be fixed to the target mass M_t. In this assumption, the source velocity cam be also obtained from the momentum balance as following.

$$\beta = \frac{\sqrt{(E_p + M_p)^2 + M_p^2} - \sqrt{(E_p + M_p - \Delta E)^2 - M_p^2}}{M_t + \Delta E} \tag{118}$$

In the above calculation, all the deposited energy have been assumed to be used for the forward moving. The obtained "source velocity" β should to be compared to the moving source velocity obtained by the moving source model fitting. Results of deformed moving source model fitting of the energy spectra for IMF-multiplicity=3 event are also shown in Tab.18. The moving source velocity have about half values of the corresponding values estimated by ΔE.

7.3.2 Deformed Nuclear Matter Formation

In Fig.72, most of the observed temperatures are distributed around $T \sim 5MeV$, however, there are some exception. Observed temperatures for Ag and Sm targets in $Ep = 12GeV$ reactions show very high temperatures if they are required IMF-multiplicity=3. Considering the incident proton

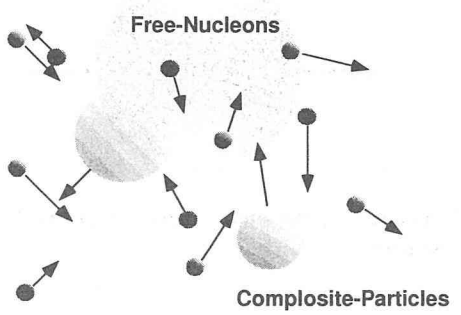

Figure 85: Assuming system of mixed ideal for the isotope temperature evaluation, consisted with free nucleons and fragments.

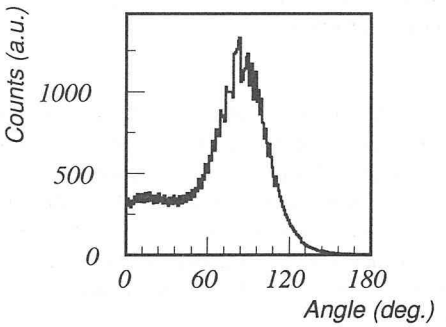

Figure 86: Example of a resultant angular distribution of a fragment density extracted from typical U-shaped temperature and free nucleon densities.

	$12GeVp+A$				$8GeVp+A$		
	Au	Tm	Sm	Ag	Au	Sm	Ag
$\Delta E(GeV)$	2.532	2.404	2.356	2.072	2.248	2.092	1.840
β	0.0140	0.0155	0.0171	0.0209	0.0125	0.0152	0.0187
β(MS fit)	0.0064	0.0063	0.0069	0.0058	0.0076	0.0089	0.0156

Table 18: Total deposited energies (for a central collision) ΔE, expected moving source velocities β, and typical moving source velocities obtained by the deformed moving source model fitting.

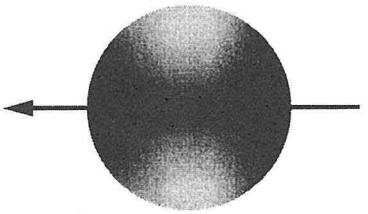

Figure 87: Temperature distribution in the source matter expected by the U-Shaped angular dependence of the obtained temperature.

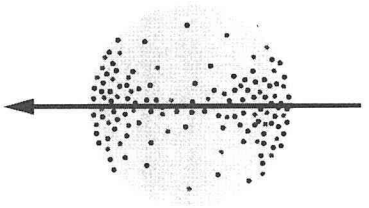

Figure 88: Free nucleon distribution in the source matter expected by the U-Shaped angular dependence of the obtained free nucleon densities.

penetrating path length in the target nuclei and the target volume which shares the deposited energy, these reaction should have largest energy densities because of their higher beam energies and smaller impact parameters and smaller target volumes. Thus it is possible to assume that the observed high temperature is a trace of nucleon gas phase produced in the collision. Because of the small cross section comparing to the inclusive cross section ($<\sim 10^{-4}$), those events which IMF-multiplicity equal 3 may be recognized as nearly central collision if the negative correlation between impact parameters and IMF-multiplicity is true [115]. Using the assumption, first order energy density ρ_E can be estimated as following.

$$\rho_E = -\frac{dE}{dX}\frac{2r_0A^{1/3}}{4\pi/3r_0^3A} \tag{119}$$

$$\propto A^{-2/3} \tag{120}$$

Eq.120 is obtained by the total deposited energy, which is obtained by the nuclear stopping power multiplied by the incident proton penetrating path length, and divided by the target volume (See Fig.95).

If the considering events were in the system of complete gas phase, observed temperature should be proportional to the energy density. Thus, target mass dependence of the temperature can be expressed as following;

$$T \propto \rho_E \propto A^{-2/3} \tag{121}$$

Mean value over the angular distributions from 30° to 150° of the temperatures (T_0) are shown in Fig.94 as functions of target mass. There are only IMF-multiplicity=3 events on $Ep = 12GeV$

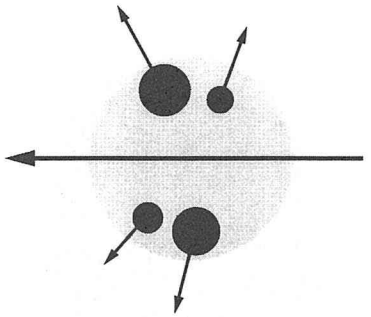

Figure 89: Fragment distribution in the source matter expected by the U-Shaped angular dependence of the obtained temperature and free nucleon densities.

reactions are plotted because they are assumed to be in the complete gas phase. The error bar represents the RMS value (Eq.84). In Fig.94, upper solid line represents the fitting results using Eq.121. The observed temperatures show more steep target mass dependence predicted by Eq.121.

In order to reproduce the steep target mass dependence, target volume should be modified. If there were a tunnel formation through the proton penetrating path, which is predicted by T. Maruyama et al.[107], it may be assumed that there are no matter which can be a source of the fragment inside the tunnel region. Thus the volume factor in Eq.120 should be subtracted with the tunnel volume. Considering the reaction dynamics of proton and nuclei, energy dispersion into the target nuclear matter should be independent to the size of the target. Thus the expected tunnel radius may be assumed to be independent on the target mass. In this assumption, Eq.120 can be modified using the common tunnel radius d as following;

$$\rho_E = -\frac{dE}{dX}\frac{2r_0A^{1/3}}{4\pi/3r_0^3A - \pi d^2 2r_0A^{1/3}} \tag{122}$$

$$\propto \frac{1}{2/3A^{2/3} - (d/r_0)^2} \tag{123}$$

The observed temperatures are fitted using

$$T \propto \frac{1}{2/3A^{2/3} - (d/r_0)^2}. \tag{124}$$

The results are also shown in Fig.94 as a lower solid line. Resultant relation between the temperature and the target mass is

$$T = \frac{62.05}{2/3A^{2/3} - 2.62^2}, \tag{125}$$

thus, expected tunnel radius is estimated as

$$d = (2.62 \pm 0.45)r_0. \tag{126}$$

This result of the tunnel radius may be used to restrict the theoretical calculations on the collision dynamics. The obtained geometry of the toroidal shaped source matter will be used in the following excitation energy estimation.

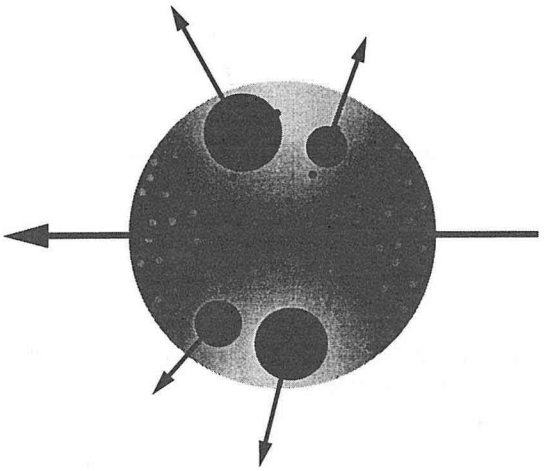

Figure 90: Expected phenomena. Fragment density should be large at the sideward region where the source matter has relatively low temperature and low free nucleon densities.

7.3.3 Energy Density Estimation

Using the results of nuclear stopping power, we can estimate the first order deposited energy onto the target nuclei. However, the deposited energy estimation by means of the nuclear stopping power is strongly dependent on the assumption of the calculation. The best way to obtain the energy density which is used as a horizontal axis of the nuclear caloric curve is, of course, direct experimental measurement of them. It is well known that there are clear correlation between average excited energy of the nuclear matter $\langle E \rangle / \langle A \rangle$ and Z_{bound}. HereZ_{bound} is defined as

$$Z_{bound} = \sum_{Z \geq 2} Z_{IMF}. \tag{127}$$

The summation should be performed for all the emitted fragment in a reaction. Thus it is necessary to detect all the charged fragment in the reaction in order to obtain Z_{bound}. It is less difficult in heavy ion induced experiments because of the large center of mass velocity. Although the experimental setup of KEK-E337 and E393 have a large solid angle coverage about 20% of 4π, it is not sufficient for this purpose. Thus it is impossible to estimate the excitation energies by means of Z_{bound} data.

Although it is impossible to obtain exact excited energy, it is worth try to make first order estimation of the excited energy in order to understand the obtained features of the temperatures in terms of nuclear caloric curve. There are two ambiguities in the excited energy estimation using the nuclear stopping power.

1. Total deposited energy estimation
2. How to share the deposited energy in the source nuclear matter

As for 1., it can be estimated as following;

$$E_{total} = -\frac{dE}{dX} \cdot l(b) \tag{128}$$

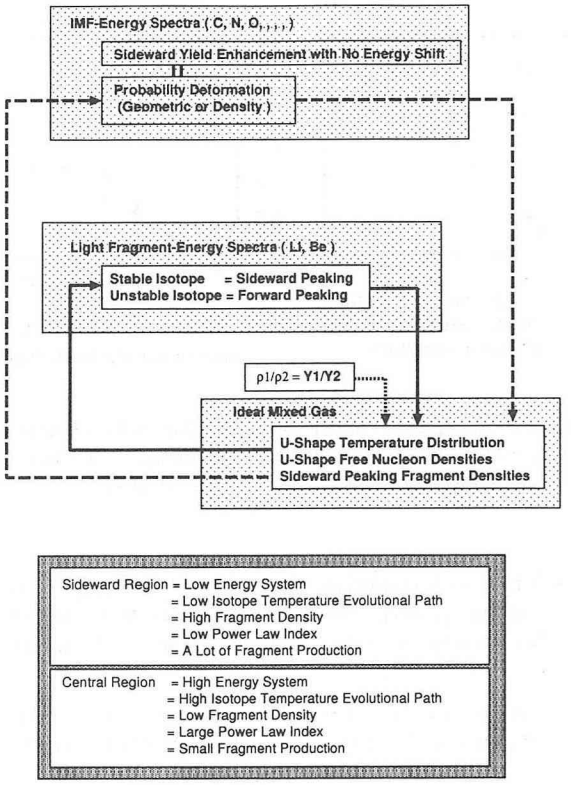

Figure 91: Logic chart for understanding the origin of the sideward peaking.

here E_{total} is the total energy deposition on the target nuclei, dE/dX is the nuclear stopping power estimated by Cugnon's calculation [134], and $l(b)$ is a penetrating path length of the incident proton at impact parameter b. There are ambiguities that the nuclear stopping power can be treated as a reliable quantity or not, and that the integrated total energy deposition may be obtained only by simply multiplying the path length or not. In spite of the ambiguities, it is not necessary to make a detailed discussion for this first order excitation energy estimation.

The second ambiguity is serious even in the present rough calculation. There are a lot of possible way to share the deposited energy E_{total}. There are two point to be considered as the following;

First. Energy density distribution at the freeze out

Second. Geometrical condition of the source nuclear matter.

For a simplicity, two cases are studied for the energy distribution.

1. uniform distribution
2. $\rho_E \propto 1/r$ from the path

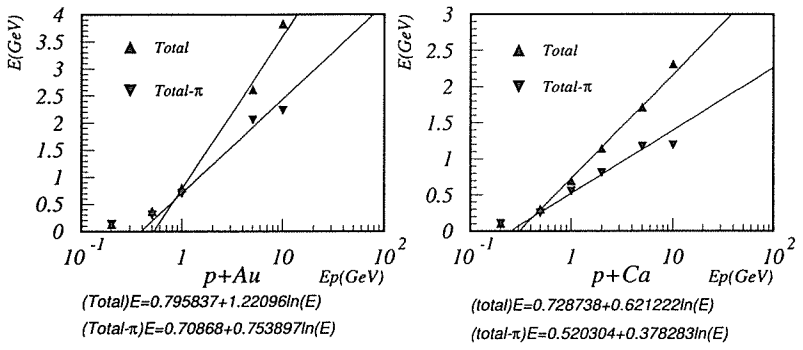

Figure 92: Calculated energy loss in p+Au and p+Ca reaction. Reported by Cugnon [134]. The fitting lines are obtained for those points of $1GeV \leq E_p \leq 10GeV$.

The second case is considering such condition where deposited energy should be larger around the penetrating path of the incident proton. Here r is a distance from the penetrating path line. Of cause there are many other possible case, but above two case is the most simple condition. Thus they may be studied at first.

In order to obtain the energy density which will be used in the expected caloric curve, they should be obtained as angular distribution. For this reason, there should be another assumption.

First. Fragment emission center is same as the target center

Second. Observed energy density is the mean value in the line starting from the target center to the direction of fragment emission.

On the above assumption, the energy density can be obtained as angular distribution. Expected energy density is obtained as following;

$$E_{exc}(\theta, b) = \frac{1}{sin(\theta_e)} \int_0^{2\pi} d\phi_e \int_0^{R_t arget} dR_e \rho_E(r_c, \theta_c, \phi_c) R_e^2 sin(\theta_e) \tag{129}$$

The normalization are performed as following.

$$\int_{totalV} dv \rho_E = E_{total} \tag{130}$$

Eq.129 is a formation for a exclusive case with an impact parameter b. In order to compare with the experimental data, inclusive value should be estimated as following.

$$E_{inc}(\theta, b_{max}) = \int_0^{b_{max} \leq R_{total}} db E_{exc}(\theta) \cdot 2\pi b \tag{131}$$

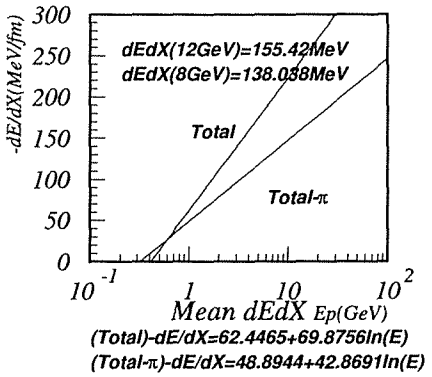

Figure 93: Resultant nuclear stopping power obtained as mean values between those of p+Au and p+Ca reactions.

Here b_{max} is the maximum impact parameter to be considered in the reaction. The target center O, center of the penetrating path P are defined as shown in Fig.96. The coordinates are defined as followings in spherical coordinates (r, θ, ϕ);

$$\vec{OR} = (R_e, \theta_e, \phi_e) \tag{132}$$

$$\vec{PR} = (R_c, \theta_c, \phi_c) \tag{133}$$

$$\vec{OP} = (b, \frac{\pi}{2}, 0) \tag{134}$$

The transformation from (R_c, θ_c, ϕ_c) to (R_e, θ_e, ϕ_e) is expressed as following.

$$R_c = \sqrt{R_e^2 - 2bR_c sin\theta_e cos\phi_e + b^2} \tag{135}$$

$$cos\theta_c = \frac{R_e}{R_c} cos\theta_e \tag{136}$$

Using the above transformation, the integration in Eq.129 can be calculated.

In order to obtain final results of $E_{exc}(\theta, b)$, ρ_E must be defined. As mentioned before, two cases are studied.

1. $$\rho_E(r_c, \theta_c, \phi_c) = const. \tag{137}$$

2. $$\rho_E(r_c, \theta_c, \phi_c) \propto \frac{1}{r_c} \tag{138}$$

Using above equations, $E_{exc}(\theta, b)$ and $E_{inc}(\theta, b_{max})$ can be obtained. In order to consider the tunnel formation effect, the volume integration in Eq.129 and Eq.130 should be performed in hole the volume of the target nuclei except in the tunnel region;

$$r_c \geq d \sim 2.6 r_0 \tag{139}$$

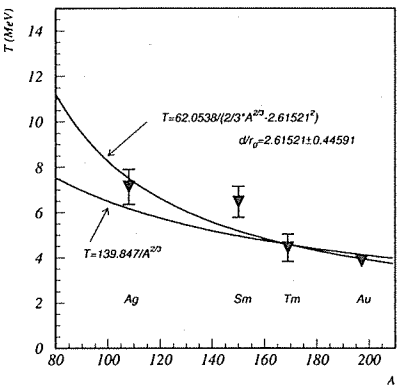

Figure 94: Target mass dependence of the temperatures obtained for central collision events (IMF-multiplicity = 3) at $Ep = 12GeV$. They are well described in the tunnel formation model.

Assuming the above relationships, excitation energy are obtained as functions of fragment emission angles. Examples for the obtained results are shown in Fig.97 and Fig.98.

The unknown parameters for the excitation energy estimation cannot be determined. Therefore, in spite of the above attempts to reproduce the angular dependence, only uniform case are used to make a caloric curve shown in the next section.

7.3.4 First Order Caloric Curve (Mean Temperature)

Using the results of the excitation energy estimation, it is possible to plot a nuclear caloric curve. In order to check the global features of the obtained temperatures, mean value over the angular distribution should be studied. In Fig.99, the mean temperature

$$\bar{T} = \int_{30^\circ}^{150^\circ} d\theta T(\theta)/sin(\theta) \tag{140}$$

are plotted as functions of the mean excitation energy which are obtained by the uniform energy distribution. In Fig.99, RMS values (Eq.84) are used as the error bars for the temperatures.

In Fig.99, turning point of the plateau to the gas phase is not clearly found. However, the tendency that those points, where higher excitation energies are evaluated, show higher temperature is found. This tendency can make an interpretation why the high IMF-multiplicity events in light target reactions shows higher temperatures. Fig.99 shows that the geometrical assumption used on the evaluation of the excitation energy have been roughly justified. At least, the assumption of the geometrical energy sharing, which results in the global relation

$$T \propto A^{-2/3}, \tag{141}$$

can be supported by Fig.99. As mentioned in the previous section, reliable results on the angular dependence of the excitation energies cannot be obtained. Fig.99 is the final results of the caloric

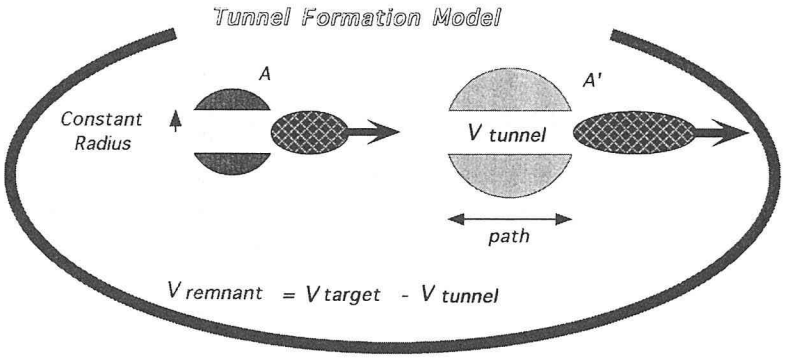

Figure 95: Schematic explanation of the tunnel formation.

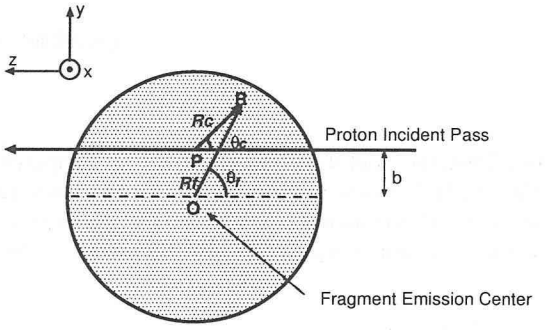

Figure 96: Definition of the coordinates used in the calculations.

curve made by the nuclear stopping power calculation at this time. Further discussion using the caloric curve are performed at later sections using power law index instead of the excitation energies estimated by the nuclear stopping power.

7.4 Fragmentation

7.4.1 Thermal Fragmentation

Fragment production probability can be estimated in the starting point of the isotope temperature procedure (Eq.55). Isotope production yield can be expressed as following.

$$Y(A,Z) \propto \rho(A,Z) = A^{2/3}(\frac{\lambda_{TN}^3}{2})^A \omega(A,Z)\rho_{pF}^Z \rho_{nF}^{A-Z} exp(\frac{B(A,Z)}{T}) \quad (142)$$

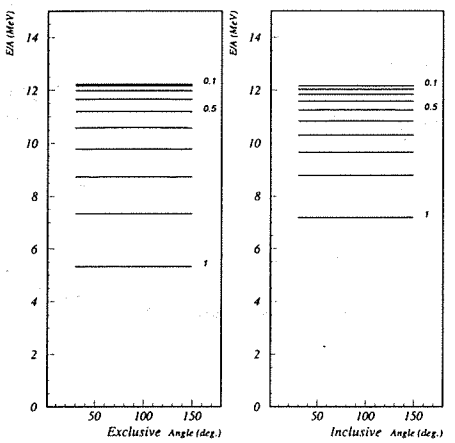

Figure 97: Angular dependence of expected excitation energy obtained for a uniform energy distribution in 12GeV p + Au reaction.

The resulting reconstructed fragment yield distribution should be compared with the experimental data. The main aim of this study is to check whether Eq.142 can reproduce the power law mass spectrum or not. Because of the Maxwell-Boltzmann statics factor $exp(B(A,Z)/T)$, the resulting fragment density might be close to simple exponential function form of the fragment mass A for a first order estimation.

$$Y(A,Z) \sim const. \cdot exp\left(\frac{B(A,Z)}{T}\right) \tag{143}$$

In fact, resultant fragment density have a exponential dependence on the fragment mass A as shown in Fig.100. Fragment densities are estimated on various conditions for examples. As predicted here, the obtained fragment mass spectra have exponential shapes. This fact clearly shows that the mass spectra resulting in thermal fragmentation Eq.142 cannot reproduce the power law mass spectra.

The temperature and the nucleon density dependences on the slope of the mass spectra can be found in Fig.100. As written in the figure, four cases $(T(MeV),\ \rho_{pF}(fm^{-3}),\ \rho_{nF}(fm^{-3})) = (4,5\times10^{-5},5\times10^{-4})$, $(4,4\times10^{-5},4\times10^{-4})$, $(5,5\times10^{-5},5\times10^{-4})$, $(5,4\times10^{-5},4\times10^{-4})$ are studied. The order represents the resultant slopes. As a result, following features are found.

1. Large $T \Leftrightarrow$ steep slope
2. Small $\rho_{pF}, \rho_{nF} \Leftrightarrow$ steep slope

The temperature dependence on the slope is clear because of the relation of Eq.143. The free nucleon density dependence can be understood considering the meeting probability of the nucleons to form the fragments. Sufficient free nucleon density is need to produce the fragments. However, there are positive correlation between the temperature and the free nucleon densities as mentioned before. The correlation is natural results from the assumption of the chemical equilibrium in the fragment and free nucleon system. As shown in Fig.100, temperature and free nucleon density variation effect opposite

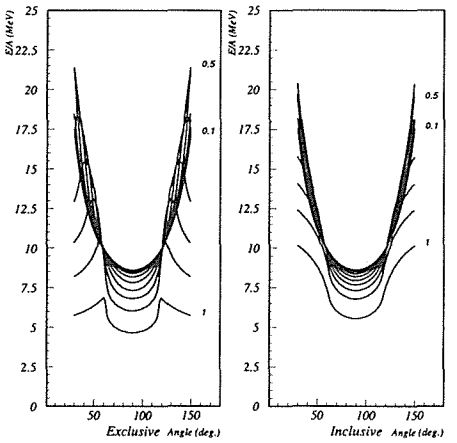

Figure 98: Angular dependence of expected excitation energy obtained for a energy distribution proportional to $1/r_c$ in 12GeV p + Au reaction.

influences on changing the slope of the mass spectra. Therefore it is not easy to predict the expected mass distribution from the obtained temperature and free nucleon densities. Considering the large angular dependence of the obtained free nucleon densities, major effects on the expected mass spectra by the thermal fragmentation should be caused by free nucleon densities. Therefore, shape of the expected angular distribution of the fragment densities may be U-Shape. An example of the obtained angular distribution of total nuclear matter density is shown in Fig.101. In fact, there is a U-Shape angular distribution. It is a contradiction. In the previous section, it was concluded qualitatively that the expected fragment density should have opposite shape as that of temperature and free nucleon densities. The origin of the contradiction is the significantly large angular dependence of the observed free nucleon densities. In order to solve the problem, following two possibility should be discussed.

1. Obtained free nucleon densities are not correct.

2. Sideward peaking phenomena can not explained as a results of thermal fragmentation.

For the first possibility, it can be accepted considering the clear failing in evaluating the absolute value of the free nucleon densities. On this assumption, if real free nucleon densities had small angular dependence, expected fragment density could have sideward peaking angular distribution as results of the thermal fragmentation.

For the second possibility, it may be true considering the actual phenomena. The observed power law fragment mass spectra shows that they cannot be produced in a simple thermal equilibrium system. This possibility should be discussed in a time evolution of the collision dynamics. It will be discussed in later section.

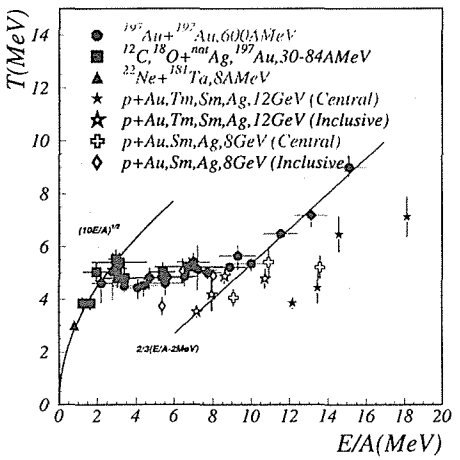

Figure 99: Resultant first order caloric curve obtained with the nuclear stopping power calculations.

7.4.2 Percolation Production

Multifragmentation is a complex and far-from-understood area of current nuclear physics research. A simple percolation model can reproduced the fragment production cross sections phenomenologically [135].

Here the most simple bond-percolation model is used to be compared with the experimental data. In this model, nucleons are supposed to be on sites of a simple cubic lattice in three dimensions and their nearest-neighbor interaction via bonds. The lattice sites are located in a spherical volume. The number of the lattice sites are equal to the number of nucleons in the fragment source. Since the nuclear matter binding energy is about 15.75MeV, energy of each bond E_{bond} can be roughly estimated as following.

$$E_{bond} = \frac{15.75MeV}{6/2} = 5.25MeV \tag{144}$$

It is because a nucleon shares 6 bonds with its neighbors. Then the lattice is broken with a bond-cutting probability p. Resulting size of the connected clusters, which are called as percolation clusters, are recognized as the size of the nuclear fragments. Although it is a simple formulation, the results reproduce the experimental fragment mass spectra very well. In Fig.102, examples of fragment mass distribution from ^{197}Au nuclei are shown with various percolation parameters p. As shown in Fig.102, this model can reproduce the power paw spectra of the mass distributions at around $p \sim 0.8$. It is widely believed that the critical point, where the mass spectra became single power law shape without any peak around the target area, is corresponding to a phase transition condition [135]. Generally, such critical point can be observed at around $p \sim 0.8$. The fragment yield distribution reported by Hirsh et al. for $p + Xe$ at 80 - 350 GeV/c reaction [18] is expressed as following.

$$Y \propto A_f^{-2.65} \quad (p + Kr) \tag{145}$$

$$Y \propto A_f^{-2.64} \quad (p + Xe) \tag{146}$$

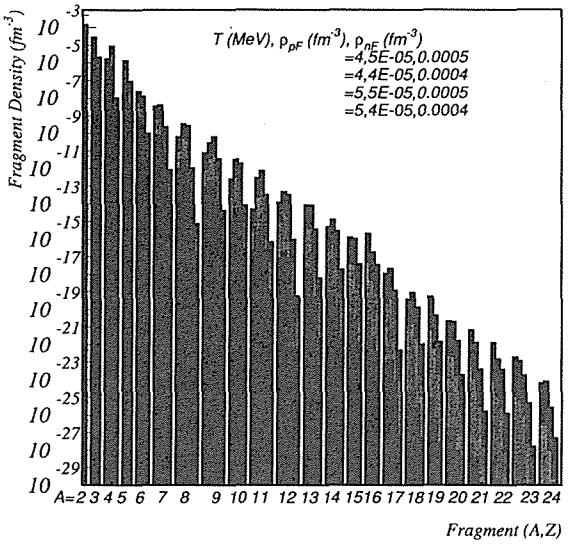

Figure 100: Examples of reconstructed fragment distributions caused by the thermal fragmentation.

Above distribution can be reproduced using following percolation parameters

$$p = 0.81 \quad (p + Kr) \tag{147}$$

$$p = 0.82 \quad (p + Xe) \tag{148}$$

in the bond percolation simulation [135]. Considering Eq.144, mean excitation energy E/A of the fragment source can be estimated as following using p.

$$E/A = p \times 15.75MeV \tag{149}$$

For the above case, resultant values of the excitation energy is estimated as;

$$E/A \sim 12.9MeV. \tag{150}$$

Because of the present experimental data taken by the BCC can not identify the mass numbers of the heavy fragment, the procedure may not be compared directly. Power law is also valid for a fragment charge distribution. In the small charge region where BCC can detect the fragments, fragment mass number may be roughly treated as $A_f \sim 2Z_f$. Thus expected mass distributions should be obtained as

$$Y \propto Z_f^{\tau_Z} \sim \left(\frac{A_f}{2}\right)^{\tau_A} \propto A_f^{\tau_A} \tag{151}$$

Therefore the power law index τ_Z obtained in the charge distribution can be assumed to be equal to that in the mass distribution τ_A. In the next section, experimental power law index τ_Z will be studied.

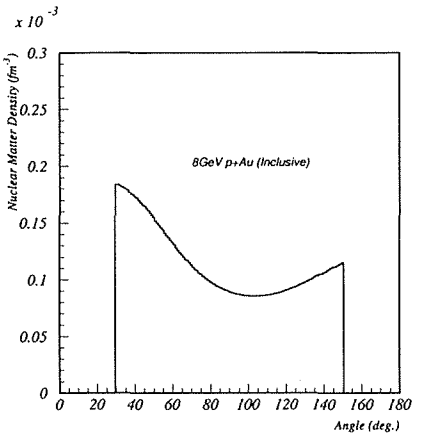

Figure 101: One example of the reconstructed angular distribution of total nuclear matter density. Error bars are not drawn.

7.4.3 Power Law

It is well known that the fragment mass spectra shows a power law spectra in multifragmentation reactions.

$$Y(A_f) \propto A_f^{\tau} \tag{152}$$

In Fig.103, typical fragment charge distribution is shown. Each fragment yield $Y(Z_f)$ is estimated using the results of deformed moving source model fitting. The solid lines imply the results of the power law fitting. As shown in Fig.103, obtained charge distributions show slightly larger tails than expected from the power law. Although the heavy side does not match with the power law, power law fitting is valid for parameterize the shape of the charge distribution at least for the lighter fragments.

Considering the thermal equilibrium, heavy fragments have smaller production probabilities than light fragments, which have smaller binding energies. At the same time, fragment production probability may be large at small equilibrium temperature. Therefore, expected mass spectra might have steeper shape in higher temperature system than in lower temperature system. It implies that without considering the relation between temperature and power law index, power law index τ should have larger value in high temperature system. If the results of the isotope temperature were correct, the observed angular distribution and some other features should be also found in resultant power law index τ.

Fig.104 shows the results of the power law fitting on the experimental data. Fragment yield have been obtained by integrating the energy spectra. The energy spectra integration have been performed on the results of the deformed moving source model fitting (Eq.26, 27). The fitting procedure is as same as for the isotope yield estimation. Detail report of the energy spectra fitting is reported in [123]. Although the fluctuations caused by the ambiguity on selecting fitting region, clear U-Shaped angular distributions can be found in Fig.104. It is corresponding to the U-Shaped angular distribution of the temperature shown in Fig.72. In addition, target mass dependence is also almost same as found in the results on the temperature. The correlation between the obtained temperature and the power

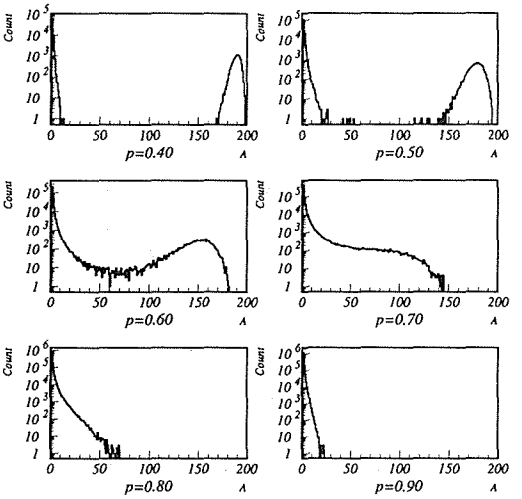

Figure 102: Cluster size distribution for disintegrating systems of ^{197}Au obtained by percolation simulations.

law index strongly supports the results of obtained U-Shaped temperature distributions.

As discussed in the previous section, power law index has correlation with the percolation parameter p, which can be roughly translated as the excitation energy as expressed in Eq.149. Therefore, if the percolation parameter p were estimated, excitation energy could be roughly estimated. In order to obtain the transformation between the power law index τ and the corresponding percolation parameter p, percolation simulation have been studied.

In Fig.105, results of the simulation are shown. Fragment mass spectra resulting from percolation process at each p are studied for each of the four source target nuclei. The vertical axis in Fig.105 means the fragment mass (cluster size), and the horizontal axis is corresponding to the percolation parameter p in (%). As shown in Fig.105, two peaks are observed in small p region, on the other hand, there are only one power law shaped mass spectra in the large p region. The mass spectra are obtained as inclusive spectra without multiplicity selection. Strictly speaking, the obtained results may not be used in the transformation between high multiplicity mass spectra and percolation parameters, but here the same results on the percolation simulation are used for a simplicity. It is because the ambiguity should be small comparing to the transformation procedure Eq.149 itself.

Power law fittings are performed at each p on the results of Fig.105. The fitting regions are selected as $A = 4 - 29$ (Au); $A = 3 - 28$ (Tm); $A = 2 - 27$ (Sm); $A = 1 - 26$ (Ag). Considering the difference of the mass spectra, the target size dependence put into the fitting region are chosen manually.

The results of the power law fitting are shown in Fig.106. Obtained τ parameters are plotted as functions of power law index p and corresponding excitation energy E/A (Eq.149). There are slight target source size dependence. Resultant τ spectra have peaks around $p \sim 70\%$. Using Fig.106, experimental power law index can be transformed to the corresponding percolation parameters. As shown in Fig.106, there may be two possible solutions of p for a τ. The smaller solution is

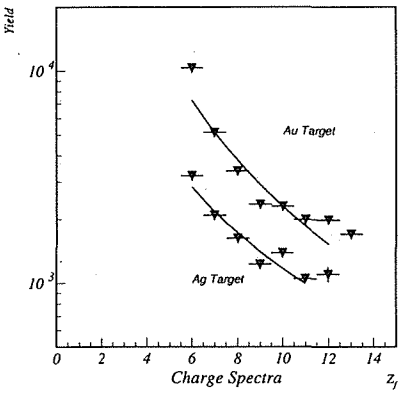

Figure 103: Typical fragment charge distributions obtained in E337. Power law fittings are performed for all the obtained charge spectra at each angle.

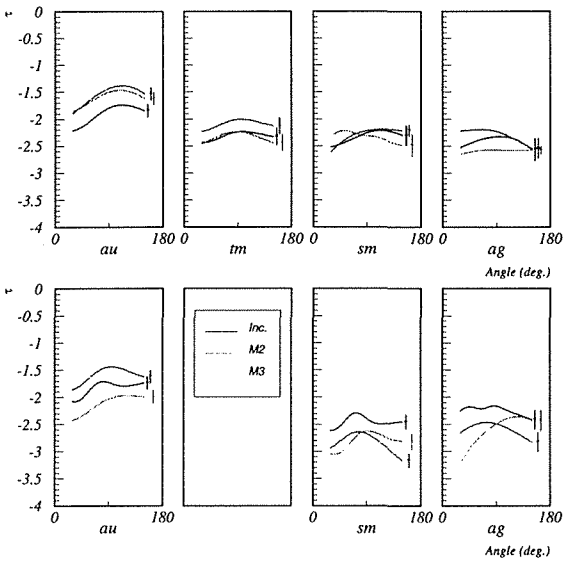

Figure 104: Experimental results of the angular distributions of the power law index.

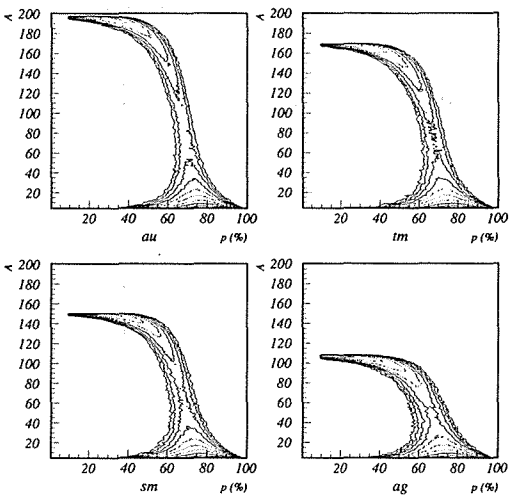

Figure 105: Cluster size distributions for various targets plotted as functions of the percolation parameter p, obtained from the bond percolation simulation.

corresponding to the mass spectra which has another heavy mass peak shown in Fig.105. It can not be decided which solution is true using the limited dynamic range of the experimental mass spectra. The similar calculation was studied by W. Bauer [135] as introduced before. The results

$$(\tau, p) = (2.64, 0.82) \; or \; (2.64, 0.58) \tag{153}$$

for FNAL experiment obtained by Bauer is also plotted in the Fig.106. According to Bauer, only higher solution meet with the ratio r_{KrXe} between the experimental cross section;

$$\frac{d^2\sigma/d\Omega dZ_f(Xe)}{d^2\sigma/d\Omega dZ_f(Kr)} \tag{154}$$

at $\theta = 34°$. The two solutions are indistinguishable in the mass spectra, but only higher solution can reproduce the ratio r_{KrXe}. Therefore, considering the Bauer calculation, higher solution of the expected two solutions in Fig.106 should be selected.

It must be noticed that there are no solutions for $\tau > \tau_c \simeq 2.2$. Here τ_c is the peak value of the τ spectra. Those small power law index are corresponding to the mass spectra which may not recognized as a power law spectra because of the existence of large tails. Considering the fact that the power law spectra are observed in a critical condition as in liquid-gas phase transition, the small τ mass spectra which do not have corresponding solution of the percolation parameter can not recognized as a resultant fragment mass spectra from a critical condition. On other words, these small τ value may be observed in low energy reaction below the critical energy at the liquid-gas phase transition.

This idea is well confirmed in Fig.107. In Fig.107, correlation between averaged temperature and τ on the angular distributions are plotted. The small τ region where no percolation parameter

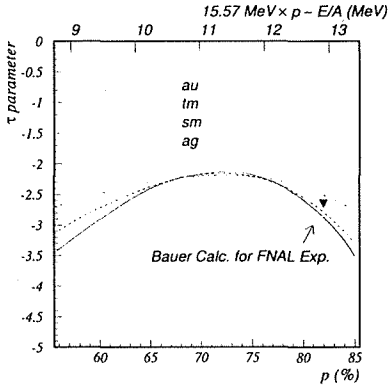

Figure 106: Results of power law fittings on the results of the fragment mass spectra obtained by the bond percolation simulation.

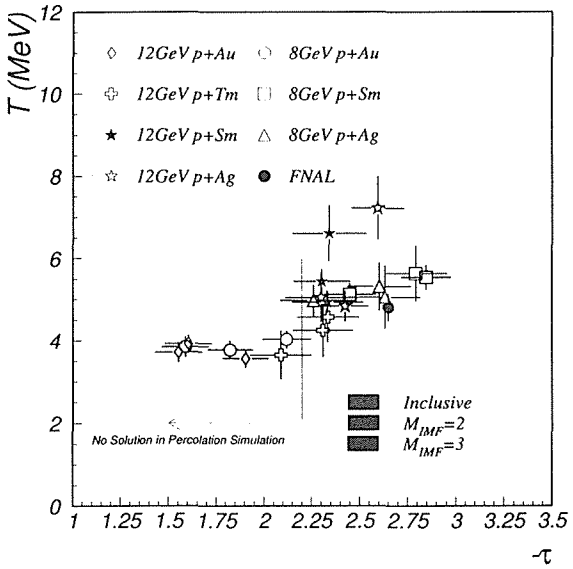

Figure 107: Correlation between the temperature and the power law index. Mean values are plotted.

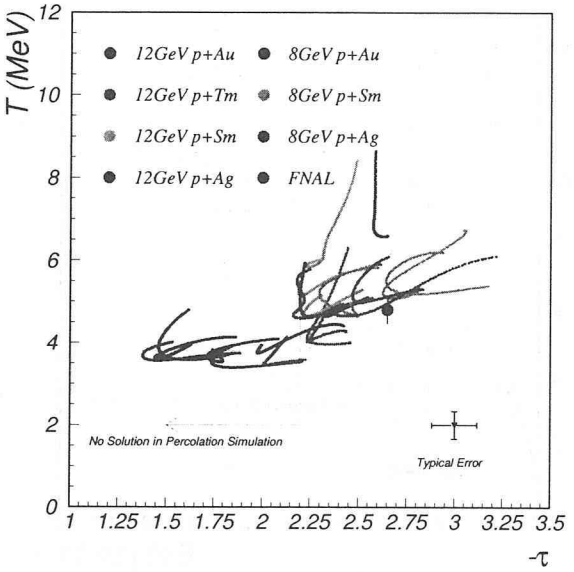

Figure 108: Correlation between the temperature and the power law parameter. All the observed points are plotted.

solutions exist show a plateau around $T \sim 4MeV$, which may be corresponding to the observed plateau in the caloric curve. On the other hand, in large τ region where τ can be transformed into percolation parameter, increasing temperatures can be found as functions of τ parameters. It may be corresponding to the gas region in the caloric curve.

In Fig.107, only mean values are shown in order to understand the global feature. It is also possible to make the same figure without averaging on the angler distributions. The corresponding results are shown in Fig.108. The point to be noticed is that, the expected plateau is also found in the correlation points. The increasing correlation in the gas region after the boiling point can be also observed in Fig.108.

Using Fig.106, it is possible to transform the obtained τ into the percolation parameters and corresponding excitation energies for $\tau \geq \tau_c$ points. However, it is impossible to obtain excitation energies for $\tau < \tau_c$ points.

Fig.109 shows the resultant caloric curve. As mentioned above, small τ points can not be plotted as reliable points. On the other hand, all the gas region points are plotted in $E/A \geq E/A_c \simeq 11.5MeV$ region. Here E/A_c is the excitation energy corresponding to the boiling point. Because of the restriction ;

$$70\% < p < 100\% \Leftrightarrow 11.5MeV < E/A < 15.57MeV, \tag{155}$$

expected points in the caloric curve can not be spread in a wide excited energy range. The points in the gas points are located in a very concentrated excitation energy region around $E/A = 12MeV$. Considering the ambiguity on the transformation between the raw τ parameters and the excitation

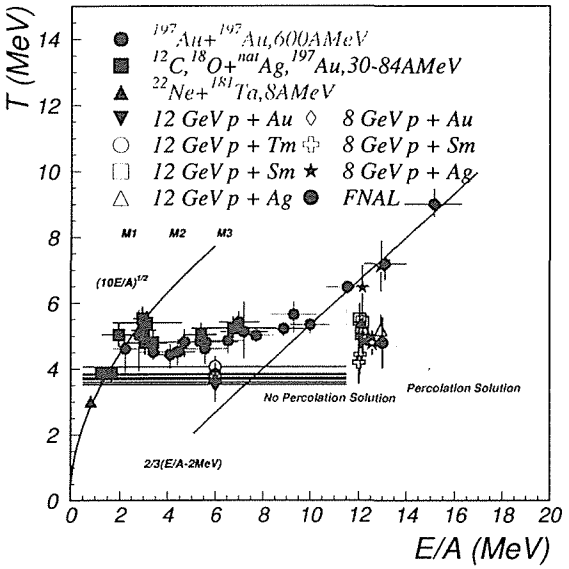

Figure 109: Caloric curve obtained with the percolation model calculations and experimental power law index.

energy, interpretation of the observed features in the obtained temperature in terms of caloric curve should be discussed using raw τ parameters in stead of excitation energies.

In Fig.107 and Fig.108, result of FNAL experiment is also plotted as a reference point. The point meet with the other many points very well as a point in the gas region . Fig.108 shows that all the points can be located in the plateau region or in the gas region. Therefore, although hole the targets may not be thermal equilibrated, obtained results of Fig.108 shows the success of the calorimetry for the local area of the source nuclear matter.

7.4.4 Interpretation of the obtained temperature analysis

There are some points which have been declared to be discussed in this chapter using expected caloric curve.

1. Angular distributions
2. Target mass dependences
3. Beam energy dependences
4. IMF-multiplicity dependences

As for 1. and 2., they have already partially been discussed before. It is because they are strongly

associated with the collision dynamics rather than the property of the nuclear matter which is suitable for being discussed in the caloric curve.

7.4.5 Angular distributions

In the reported caloric curve figure (Fig.6), fragment emission angle is a hiding dimension. On other wards, the figure can be interpreted as a projected figure into the direction of the emission angle. Considering above features, following discussion can be accepted.

1. Small angular dependence of the temperature $\Leftrightarrow$ in the plateau
2. Large angular dependence of the temperature $\Leftrightarrow$ in the gas region

Above relation can be confirmed in Fig.108. In the plateau region, considering system might be in liquid-gas mixed phase. Thus the equilibrium temperature should be distributed in a narrow region around the critical temperature. The small τ parameter dependences of the temperature in the plateau region might be corresponding to such mixed phase condition. Following reactions are considered to be in the mixed gas phase.

- All the p + Au reactions for all the IMF-multiplicity and at all the beam energy.

The large angular dependences of the temperature can be found in Fig.108 as a long leaning lines in large τ region. The lines are not collected as found in the plateau region. It seems to be a explosion after the boiling. There are no reason to collect the lines because of the pressure dependence. If the time evolution at a path in the phase diagram of the collision were different, resultant correlation between temperature and excitation energy could be different. Following reactions can be interpreted as in such condition.

- All the p + Tm, Sm, Ag reactions for each IMF-multiplicity and beam energy.

7.4.6 Target mass dependences

The origin of the target mass dependence may be the geometrical condition of the $p+A$ collision as discussed before. In the previous discussion, angular dependence are ignored for the first order calculation in the section of forming deformed shape nuclear matter. The target mass dependences can be found more clearly in Fig.108. As mentioned above, only $p + Au$ reaction are found in the plateau region. On the other hand, those points corresponding to other reactions are found in the gas region. Following fine relations can be also found.

$$T(Au) < T(Tm) < T(Sm) < T(Ag) \tag{156}$$

Of course there are exception of Eq.156 because of the angular dependences, but Eq.156 can be accepted as a global feature. The expected origin of the target mass dependence is the target mass dependence of the energy density caused by the geometrical dependence. It can also be confirmed in the Fig.108. Similar target mass dependence of the τ parameters as Eq.156 can be roughly found in Fig.108. This fact support the target mass dependent energy density assumption, which used to understand the origin of the observed target mass dependence.

7.4.7 Beam energy dependences

Beam energy dependences are not clearly observed comparing to other features. It might be because of the small beam energy dependence on the nuclear stopping power discussed before. The only clearly observed beam energy dependence is the IMF-multiplicity dependence of the temperature. The IMF-multiplicity dependence will be discussed later. It is well known that that the beam energy of $E_p = 10GeV$ is the critical energy on the $p + A$ reaction to change the fragment yield angular distributions. One simple candidate of the origin for the critical phenomena is the appearance of liquid-gas phase transition at around $E_p = 10GeV$. In order to confirm the assumption, it should be found that most of those points for 8GeV reactions are in the plateau region, and at the same time, most of those points for 12GeV reactions are in the gas region in the Fig.108. However, the expected results cannot be found in Fig.108. For a example, those points corresponding to the $p + Au$ reaction at $E_p = 12GeV$ are found in the plateau region.

7.4.8 IMF-multiplicity dependences

As mentioned in the previous section, the IMF-multiplicity dependences seem to be depend on the beam energy and the target mass. Observed features are following.

1. Small IMF-multiplicity dependence $\Leftrightarrow$ heavy targets, low beam energy
   Au,Tm targets on $E_p = 12GeV$, and all target reactions on $E_p = 8GeV$.
2. Large IMF-multiplicity dependence $\Leftrightarrow$ light targets, high beam energy
   Sm,Ag targets on $E_p = 12GeV$

Considering the τ distribution found in Fig.108, the above features can be translated as following.

1. Small IMF-multiplicity dependence $\Leftrightarrow$ low excitation energy
2. Large IMF-multiplicity dependence $\Leftrightarrow$ high excitation energy

If there are negative correlation between the IMF-multiplicity and the impact parameters of the collision, larger energy should be deposited on the target than in the smaller impact parameter reactions. The above observed features show that there are smaller excitation energy dependences at the low excitation energy reactions, and on the other hand, larger excitation energy dependences are expected for higher excitation energy reactions. This is corresponding to the condition where the slope of the correlation lines drawn in Fig.108 should increase as functions of excitation energies. It has been observed in Fig.108 as the existence of two phase. The slope of the points existing region became steep over the critical point. Therefore, although the origin of the IMF-multiplicity dependence are not clearly understood, it can be considered as a phenomena associated with the change of the correlation between temperature and excitation energy at the critical point.

7.4.9 Meaning of the observed fragment mass spectra

As mentioned before, fragment mass spectra might be exponential shape if the fragmentation is occurred in a thermal equilibrated system (Eq.143). Obviously it is contradict with the obtained mass spectra which show power law distribution. Eq.143 can be roughly re-expressed as following.

$$\begin{aligned} Y(A,Z) &\sim const. \cdot exp\left(\frac{B(A,Z)}{T}\right) \\ &\sim const. \cdot exp\left(\frac{\tilde{B}A}{T}\right) \end{aligned} \tag{157}$$

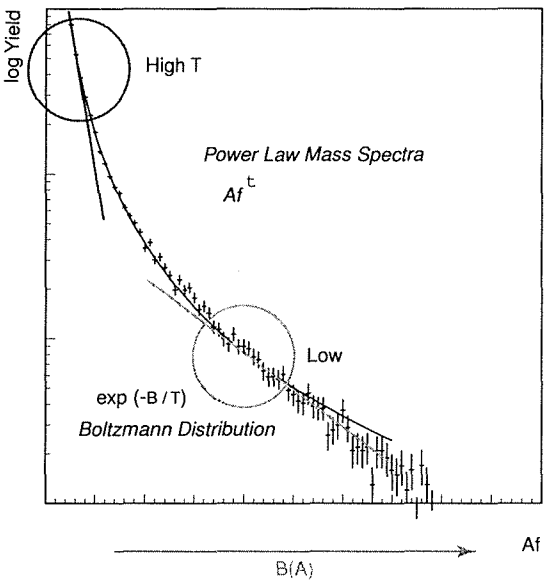

Figure 110: One explanation of power law mass spectra. Existence of the fragment source with a non-constant freeze out temperature is expected.

Here $\bar{B}$ is the mean nuclear binding energy per nucleon around the considering mass number A. Therefore, the slope of the mass spectra at each point can be considered to be associated with the corresponding temperature in the power mass spectra. As shown in Fig.110, it is obvious that if the above assumption is correct, lower temperature should be expected for larger fragment mass numbers. On other words, heavy fragments might be created in relatively low temperature condition. All the detected fragments can not be recognized as formed in a single equilibrated system. The inconsistency can clearly understood when Fig.100 and Fig.110 are compared with each other.

As a result, we can conclude that the power law mass spectra might be obtained when freeze out timing of the fragments depended on the fragment binding energies. Larger fragments should be produced in lower temperature condition, which might be appeared in relatively later timing stage in a collision. It does not imply that the limit temperature of the freeze out is depending on the fragment mass, but that the timing when most of the considering fragment have produced is depending on the fragment mass. Therefore, observed power law spectra can be understood as a summation of exponential shape mass spectra at each timing.

$$Y_{observed}(A) \sim A^{\tau} \tag{158}$$

$$\sim \int_0^{\infty} Y_{real}(t, A)dt \tag{159}$$

$$\sim \int_0^{\infty} exp\left(\frac{-B(A)}{T(t)}\right) dt \tag{160}$$

Here $T(t)$ is the equilibrium temperature at the timing t. $Y_{observed}(A)$ is the resulting mass distribution which can be determined experimentally. $Y_{real}(t, A)$ is the fragment formation probability at the

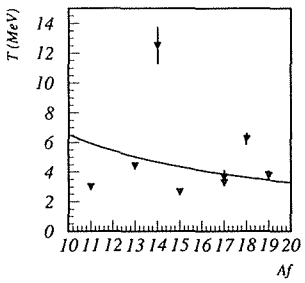

Figure 111: Fragment mass dependence of the isotope temperature.
Extracted for the FNAL data [18]. The solid line indicates the exponential fitting result.

timing of t. Eq.160 indicates that the observed power law index τ can be a probe for the distribution of the temperatures at fragment formation timings.

The interpretation of the power law mass spectra suggests that the isotope temperatures which consisted by heavy fragments may extract relatively lower temperatures than that obtained by light fragments. There are a few experimental data which can be used to check the tendency. Heavy fragment production cross sections were reported by the FNAL experiment [18]. They reported the cross sections of $^{6-9}Li, ^{7-12}Be, ^{10-15}B, ^{11-17}C, ^{13-20}N, ^{15-12}O, ^{19-19}F$. Using above isotope yields, mass dependence of isotope temperatures can be studied. Double ratio combined with three isotope yields $Y(A,Z), Y(A,Z+1), Y(A,Z+2)$ are used for the simple calculation. For this case, temperature can be obtained as following.

$$T = \frac{-B(A,Z) + 2B(A,Z+1) - B(A,Z+2)}{ln\left(\frac{Y(A,Z+1)^2}{Y(A,Z)Y(A,Z+2)} \frac{\omega(A,Z)\omega(A,Z+2)}{\omega(A,Z+1)^2}\right)} \tag{161}$$

Without any yield correction performed for extracting T_{LiBe}, mass depending isotope temperatures are obtained as shown in Fig.111. Here only ground states are taken into ω. A dependence of the isotope temperature is expected to be a decreasing function of A, however, it can not be confirmed in the present results. Further study should be performed in order to examine the assumption.

7.4.10 Time evolution in the phase diagram

In the previous section, it is shown that the power law spectra can be understood as the sequential fragment formation in a late stage of the collision. In this section, the reason why such phenomena can be occurred, and why the liquid-gas phase transition can be observed using fragment thermometers, is discussed. In Fig.112, expected path of in a collision are shown in a phase diagram. Note that the horizontal axis is not the nuclear matter density, but the matter density ρ of the colliding system. Therefore, the path start from the normal nuclear matter point $(T,\rho) = (0MeV, \rho_0)$, and end in the free space limit $(0MeV, 0fm^{-3})$. The time evolution can be followed in a path from right to left direction. The scenario of each path may be different according to their energies. In the followings, each scenario are going to be explained.

Scene I Collision to Maximum temperature timing

1. case A. (low energy)
   After hitting the target nuclei by the incident proton, the system immediately becomes at the maximum temperature condition. Because the maximum temperature is under the critical temperature for a liquid-gas phase transition, the system may be exists as a normal hot nuclear matter.
2. case B. (intermediate energy)
   The system become hot and the temperature reached to the critical temperature. After reaching the critical temperature around 5MeV, energy may be used to boiling the fragments into free nucleons. Because of the chemical energy, temperature of the system cannot become higher. In this energy region, total energy is not sufficient to make all the nucleons to be free from the fragments. Therefore, maximum temperature cannot be over the critical temperature.
3. case C. (high energy)
   If the system has a sufficient energy, there may be a positive remaining energy after boiling the fragments. The remaining energies are used to increase the temperature of the free nucleon gas system.

Scene II Maximum temperature to Li and Be fragments formation

1. case A. (low energy)
   In this case, fragment formation may not occurred by the freeze out of free nucleon gas. Fragmentation may be due to cracking of the system with the source expansion. Therefore Li and Be fragments which may be used to make a thermometer can not be a proper probe for the system temperature. For such low temperature system, excited state population ratio of the fragment may be the best thermometer.
2. case B. (intermediate energy)
   The system is going to be cool in the adiabatic expansion. Whether there exist Li or Be fragments at the maximum temperature point or do not, Li and Be fragments are going to be formed by the free nucleon gas. Of course, heavier fragments are created, however, the most suitable temperature for the heavier fragment creations should be lower than that for Li and Be fragments. The observed isotope temperature probes the system temperature at this timing.
3. case C. (high energy)
   The free nucleon gas system with high temperature are also going to make adiabatic expansion. After the temperature become lower than the critical temperature, fragment creation starts. Fragmentation may be started from d,t,^3He ,,, and so on. The sequential fragmentation may be same as in the case B. However, the temperature at the timing when most of the Li and Be fragments are created, may be higher than that for the case B. It is because the cooling path of this case are started from much more high temperature points than the critical temperature.

Scene III Sequential fragmentation

1. case A. (low energy)
   In this case, there are no phenomena corresponding to the sequential thermal fragmentation. There may only expanding group of the cracked fragments.
2. case B. (intermediate energy)
   Heavier fragments are going to be created sequentially after dominant Li and Be fragments formation timing. Because of the timing differences, resultant mass spectra may be

integrated spectra of the mass spectra at each timing. The slope of the mass spectra are roughly corresponding to the temperature at the freeze out timing.

3. case C. (high energy)
   Resultant phenomena may be same as in the case B. The difference is the system temperature at the fragment freeze out timing. Because of the relatively higher temperatures than that for the case B., resultant mass spectra should have steeper slopes.

In Fig.112, observed relation between isotope temperatures and τ parameters can be understood. What should be noticed is that, the isotope temperature which have been estimated using the Li and Be fragment yields is different from the maximum temperature of the collision. In order to confirm that the fragment chemical thermometers can be a probe for the liquid-gas phase transition at the timing of maximum temperature condition, the environment temperature at when most of the considering fragments are produced, should be dependent on the collision energy. If the fragmentation were occurred at a freeze out temperature independent on the system energy, there might be observed only constant isotope temperatures. The path difference drawn in Fig.112 can be a candidate for the explanation of the observed liquid-gas phase transition in caloric curve.

7.4.11 Understanding sideward peaking phenomena in the phase diagram

Fig.112 is shown as a trace of time evolution in a collision. It can be understood as that of local system in the colliding system. It means that in one collision, the expected path can be dependent on the local area in the colliding system. It is natural that the central region close to the incident proton penetrating path should be in high energy system. On the other hand, relatively low energy path may be the correct time evolution path for the nuclear matter in the sideward region. The angular dependence of observed τ parameter clearly shows the angular dependence of the time evolution path. Considering the following relation;

- High energy path $\Leftrightarrow$ steep slope mass spectra
  $\Rightarrow$ small heavy fragment production
- Low energy path $\Leftrightarrow$ slow slope mass spectra
  $\Rightarrow$ large heavy fragment production

Therefore, sideward region can produce more fragments than high energy region. This can be a candidate for the origin of the sideward peaking. Note that this idea is similar but different from the idea discussed in the previous section of thermal fragmentation. The observed temperatures and free nucleon densities are not same as that at the timing, when most of heavy fragments are produced after most of Li and Be fragment have been created. In this case, fragment density should be calculated using the temperature and free nucleon densities at the timing when most of the fragment are produced.

8 Conclusions

The first experiment (E337) on the target multifragmentation reaction was performed at KEK-PS EP1B primary beam line in 1996 using 12-GeV proton beam. Four targets (gold, thulium, samarium, silver) were used. The second experiment (E393) was performed at KEK-PS P1 primary beam line in 1997 using 8-GeV proton beam. Three targets (gold, samarium, silver) were used.

Produced intermediate mass fragments (IMFs; $3 \leq Z \leq 25$) were detected by the Bragg-Curve Counters. Kinetic energy and charge numbers were determined for all the detected IMFs. In addition,

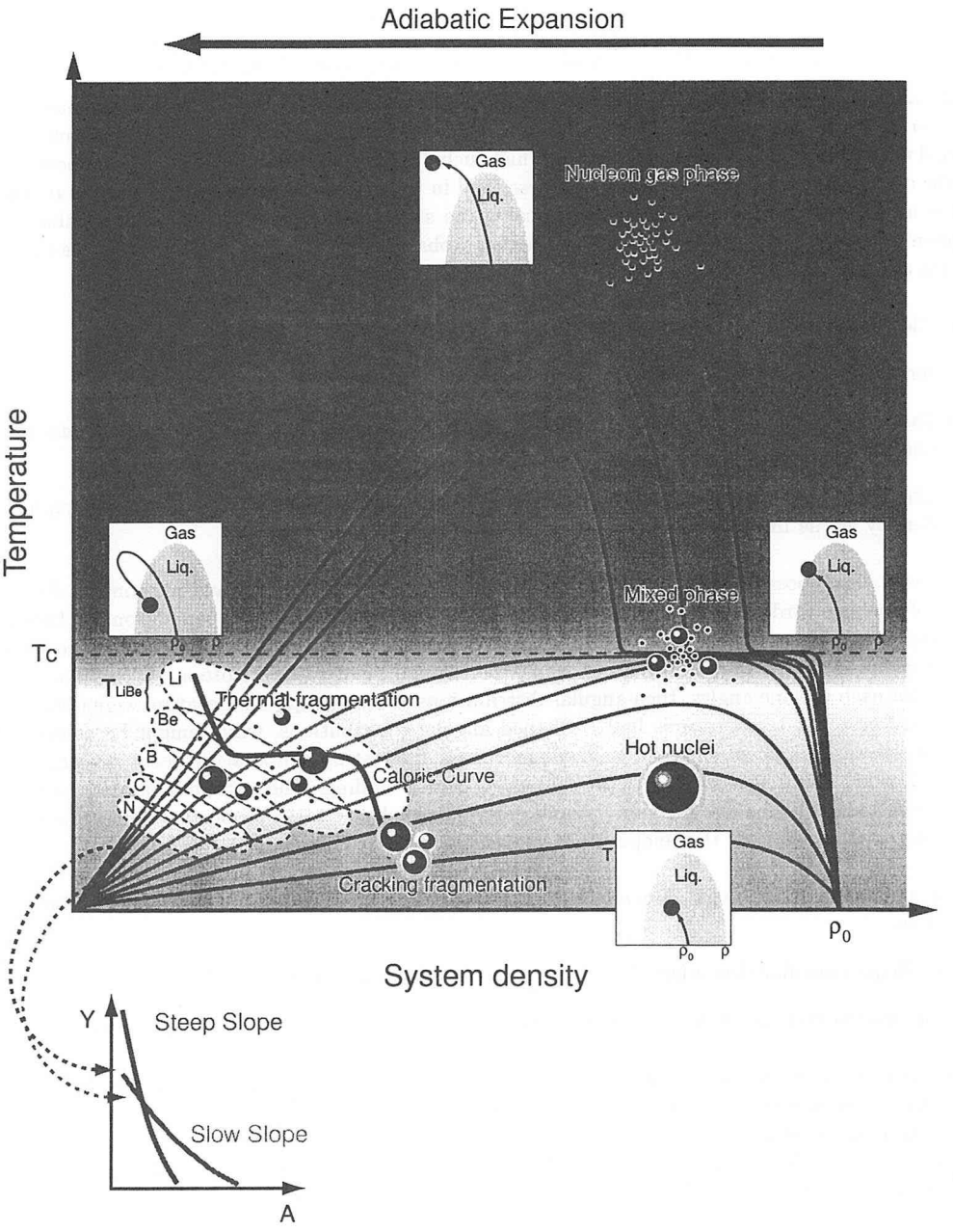

Figure 112: Expected timing evolution of the collision. The colliding systems begin their adiabatic expansions started from the normal nuclear conditions, and result in the multifragmentation system. T_{LiBe} has its sensitivity on the system temperatures on the conditions for the Li and Be freeze out.

mass separation for lithium and beryllium fragments were performed. $^{6,7,8,9}Li$ and $^{7,9,10}Be$ have been identified. Emission angle dependences, target mass dependences, IMF-multiplicity dependences on the detected fragment energy spectra have been obtained using the 37-channel BCC array. The total acceptance of the 37ch-BCC array is about 20% of 4π solid angle. Inplane emission angle dependences have been measured with 12 BCCs located at the angular step of 20° from 30° to 150°.

Resultant angular distribution of the fragment yield have anisotropic sideward yield enhancement. In order to study the component of the sideward enhancement, obtained energy spectra have been studied with deformed moving source model, which includes the component of sideward enhancement. All the obtained energy spectra can be well described in this model. Although the deformed moving source model was introduced phenomenologically, the success of the model fitting shows that the fragment source have deformed fragment production probabilities. Obtained conclusions in the energy spectra analysis are;

- Clear sideward peaking towards 70° was confirmed for all the reactions.
- Small IMF-multiplicity dependences were observed on the sideward enhancement.
- Target mass dependences of the coulomb energy shift and fragment mass distributions were observed.
- There must be formation of a geometrically deformed nuclear matter, or, non-uniform fragment density at the freeze out timing.

There were small possibilities of considering dynamical effects like shock wave phenomena for the origin of the sideward peaking. In addition to the charge separation, mass separation for lithium and beryllium fragments were performed. Main motivation of the isotope separation was the study on the chemical freeze out temperature using the isotope yield ratio. Isotope yield ratios were studied for each inplane angles, then angular distributions of the isotope temperature were obtained. Obtained freeze out temperatures had U-Shaped angular distributions, which might be associated with the sideward fragment emission yield enhancement. Interesting temperature behaviors were also obtained, which could be associated with the nuclear matter boiling. The isotope separation brought us a strong tool to probe the collision dynamics and the nuclear matter property at the same time. Resultant conclusions from the temperature analysis is listed as following.

- Fragment emission angle dependence on the isotope temperature was obtained for the first time.
- U-Shaped angular dependences on the temperature were observed.
- The fragmentation timing should be earlier than that of the total thermal equilibrium.

In addition to the freeze out temperature, free proton and neutron densities at the freeze out timing have been determined. The obtained free nucleon densities have very small absolute value. It is an open question why the obtained free nucleon densities had such small values. Resultant angular dependence on the free nucleon densities shows similar as on the temperature. U-Shaped angular distributions were also seen. The density analysis leads to the following conclusions.

- U-Shaped angular dependence of the free nucleon densities were observed.
- Clear positive correlation between the temperatures and the free nucleon densities were observed.

- Very small absolute values of the obtained free nucleon densities were obtained.

Observed beam energy dependences, IMF-multiplicity dependences, target mass dependences, and fragment emission angle dependences can be understood in the nuclear caloric curve and the geometrical condition of the collision. Non-uniform time evolution of the source nuclear matter around the critical point of the nuclear liquid-gas phase transition can explain most of the obtained phenomena. There conclusions are summarized as;

- Observed results on the nuclear calorimetry can be understood as phenomena around the critical point of the nuclear liquid-gas phase transition.
- Excitation energy difference on the different region of the expanding source matter must be the origin of the sideward peaking.

Existence of the non-uniform source matter formation were confirmed. The origin of the sideward peaking of the fragments have been understood at the same time. However, quantitative understanding on *how to produce* the non-uniform remnant matter has not been clear yet. Explanation of the deformed matter formation is an interesting theoretical subject. Complete understanding on the GeV proton induced target multifragmentation reaction, from the collision dynamics to the fragmentation, demands further experimental and theoretical investigations.

Fitting results of Energy Spetra

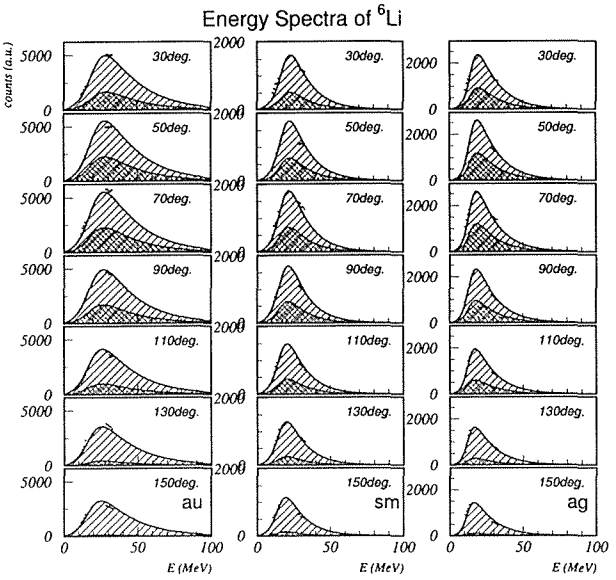

Figure 113: Fitting results of ^6Li energy spectra with the deformed moving source model. Inclusive spectra obtained in E393 with the data of P10 gas mode and of CF_4 gas mode are summed. Cross hatched area are corresponding to the side-ward component.

	^6Li			^7Li		
	Au	Sm	Ag	Au	Sm	Ag
N_0	3120	2104	1888	30113	7478	5929
T	18.61	10.84	11.24	11.02	9.80	9.90
$\beta \cdot 10^2$	0.351	0.407	0.368	0.650	0.737	0.947
B	19.18	17.09	13.82	28.98	23.90	22.16
B_c	28.93	20.39	14.93	40.00	37.80	52.85
N_f	3672	2716	2963	37587	10387	7475
σ_f	37.57	43.67	40.91	36.81	43.51	44.19
θ_f	61.35	68.25	61.81	67.51	75.69	83.36
χ^2/n	18.00	22.94	36.72	21.68	32.00	57.32

Table 19: Fitting parameters obtained in deformed moving source model fitting for the inclusive spectra of ^6Li and ^7Li fragments (E393). N_0 and N_f are listed in arbitrary unit. $T(MeV)$,$B(MeV)$ and $B_c(MeV)$ are the spectra shape parameters. $\sigma_f(deg.)$ and $\theta_f(deg.)$ are the anisotropic parameters.

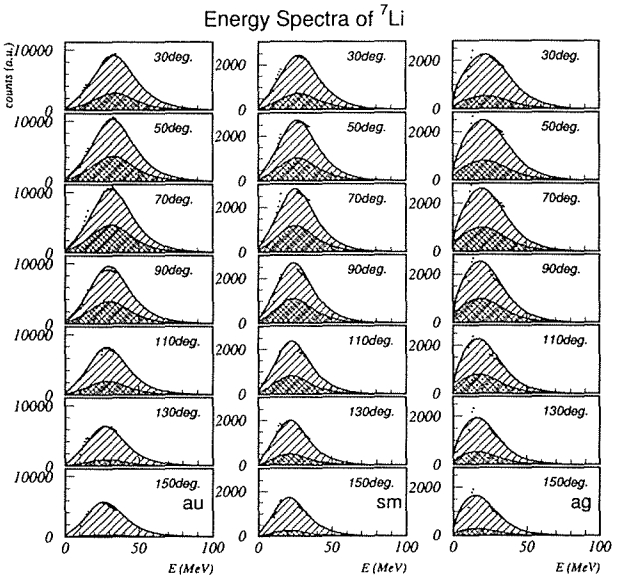

Figure 114: Same figure for ^7Li

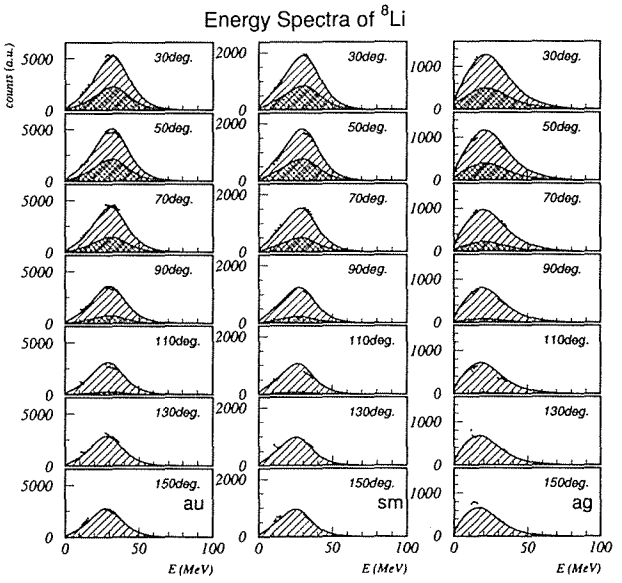

Figure 115: Same figure for ^8Li

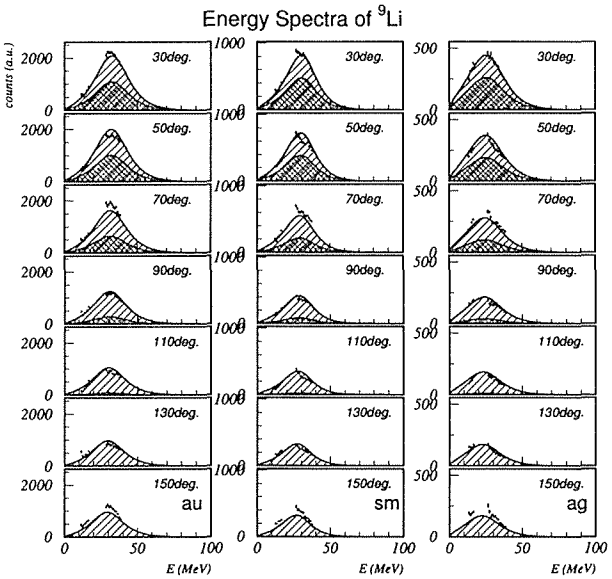

Figure 116: Same figure for ^9Li

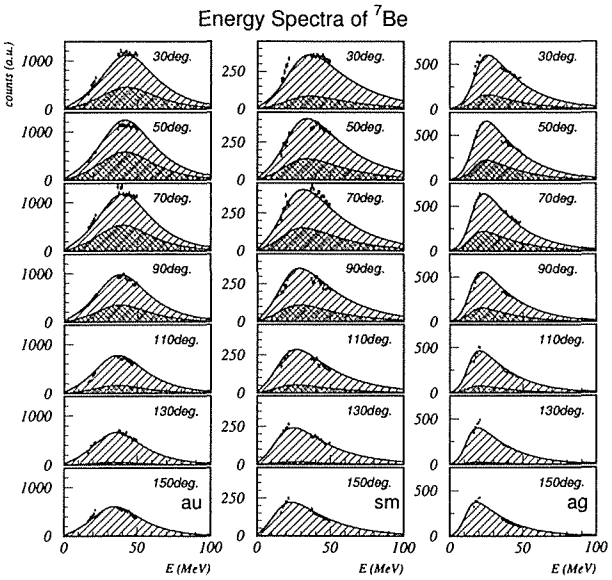

Figure 117: Same figure for ^7Be

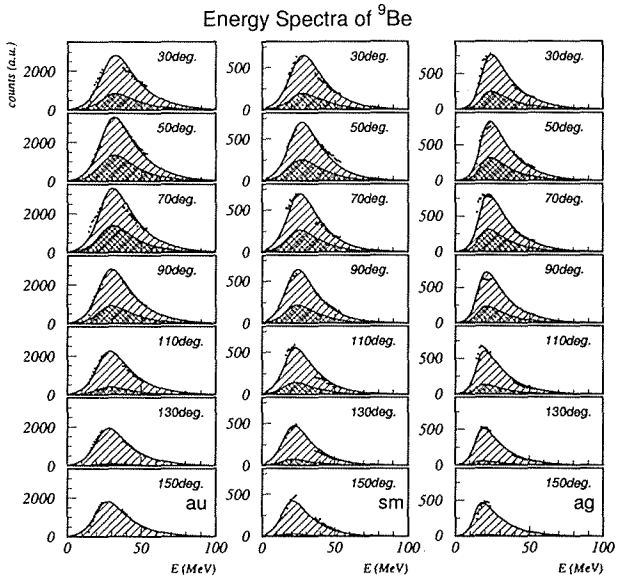

Figure 118: Same figure for ^{9}Be

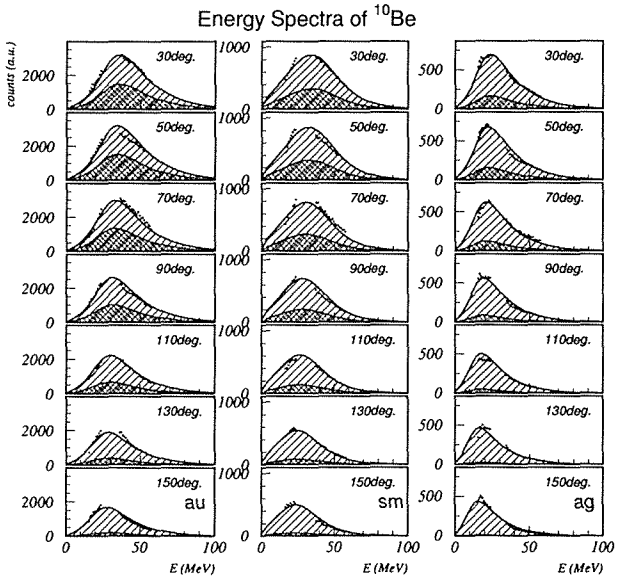

Figure 119: Same figure for ^{10}Be

	^8Li			^9Li		
	Au	Sm	Ag	Au	Sm	Ag
N_0	60551	32545	1997	15214	9367	1487
T	7.71	6.85	10.53	8.33	6.89	8.31
$\beta \cdot 10^2$	0.378	0.500	0.665	0.253	0.304	0.271
B	31.59	31.30	18.95	31.48	30.05	25.57
B_c	32.39	32.82	46.45	31.85	28.63	36.30
N_f	74784	39773	1799	24221	19272	3449
σ_f	36.05	34.55	32.72	32.53	33.54	35.47
θ_f	36.71	35.20	30.00	36.40	28.33	20.95
χ^2/n	18.51	23.49	22.52	14.21	20.84	11.55

Table 20: Fitting parameters obtained in deformed moving source model fitting for the inclusive spectra of ^8Li and ^9Li fragments (E393).

	^7Be			^9Be			^{10}Be		
	Au	Sm	Ag	Au	Sm	Ag	Au	Sm	Ag
N_0	3120	203	321	4335	943	672	2927	2595	573
T	18.61	22.66	18.49	13.41	11.89	12.53	15.86	11.45	13.57
$\beta \cdot 10^2$	0.351	1.245	0.898	0.423	0.660	0.586	0.681	0.865	0.858
B	19.18	19.31	14.65	25.18	20.65	16.54	26.13	30.73	13.72
Bc	28.93	42.41	22.36	28.42	26.76	17.59	38.40	50.22	26.90
N_f	3672	169	261	4333	1058	748	6195	4151	391
σ_f	37.57	31.62	34.13	30.39	41.84	38.63	53.26	59.27	49.96
θ_f	61.35	65.77	61.05	62.03	65.38	60.05	45.91	38.52	36.47
χ^2/n	4.32	4.45	9.79	14.80	14.73	19.88	16.55	15.67	13.61

Table 21: Fitting parameters obtained in deformed moving source model fitting for the inclusive spectra of Be fragments (E393).

	^6Li			^7Li		
	Au	Sm	Ag	Au	Sm	Ag
$(M2)N_0$	868	382	422	8703	1235	3620
$(M2)N_f$	740	225	251	9124	1044	2682
χ^2/n	5.87	5.92	19.15	26.03	22.37	25.07
$(M3)N_0$	84.9	24.5	17.5	822	79.1	141
$(M3)N_f$	54.6	11.2	8.97	665	61.6	122
χ^2/n	1.88	1.74	3.04	2.76	2.58	2.19

Table 22: Fitting parameters obtained in deformed moving source model fitting for the high IMF-multiplicity spectra of ^6Li and ^7Li fragments (E393). N_0 and N_f are listed in arbitrary unit.

	^8Li			^9Li		
	Au	Sm	Ag	Au	Sm	Ag
$(M2)N_0$	15331	5348	503	4105	1537	206
$(M2)N_f$	19459	3119	457	5798	1965	357
χ^2/n	22.09	5.58	6.34	5.67	4.77	3.76
$(M3)N_0$	1466	367	20.2	377	54.9	6.59
$(M3)N_f$	1773	121	17.8	577	170	10.1
χ^2/n	3.88	1.46	1.09	1.56	2.38	2.32

Table 23: Fitting parameters obtained in deformed moving source model fitting for the high IMF-multiplicity spectra of ^8Li and ^9Li fragments (E393).

	^7Be			^9Be			^{10}Be		
	Au	Sm	Ag	Au	Sm	Ag	Au	Sm	Ag
$(M2)N_0$	499	24.5	38.0	1050	159	140	727	425	100
$(M2)N_f$	501	13.5	33.4	965	137	67.0	1625	368	68.1
χ^2/n	2.49	2.64	2.55	13.55	4.29	12.26	4.02	4.03	3.33
$(M3)N_0$	37.8	1.39	1.59	96.7	9.33	5.47	69.6	25.1	3.29
$(M3)N_f$	44.0	1.35	0.96	81.4	8.52	2.68	109	19.1	3.93
χ^2/n	2.29	1.06	0.85	2.12	0.85	1.23	2.33	1.26	1.51

Table 24: Fitting parameters obtained in deformed moving source model fitting for the high IMF-multiplicity spectra of Be fragments (E393).

	^6Li				^7Li			
	Au	Tm	Sm	Ag	Au	Tm	Sm	Ag
$(Inc.)N_0$	56.08	116.03	140.72	91.71	699.22	940.76	612.60	235.73
$(Inc.)N_f1$	75.91	103.11	287.68	140.53	690.71	1216.68	767.30	472.35
χ^2/n	14.99	5.95	16.34	4.952	36.73	29.04	229.78	10.11
$(M2)N_0$	22.52	29.11	21.28	21.41	254.45	223.47	85.07	55.61
$(M2)N_f$	24.95	33.50	55.47	42.82	229.52	353.75	144.15	154.79
χ^2/n	4.05	5.38	12.71	1.93	3.15	8.26	45.38	3.28
$(M3)N_0$	2.32	2.39	1.44	2.33	26.86	19.35	4.97	7.40
$(M3)N_f$	3.59	3.88	3.59	5.66	30.11	39.24	11.08	16.23
χ^2/n	1.73	2.67	2.93	2.32	2.83	2.64	5.68	1.21

Table 25: Fitting parameters obtained in deformed moving source model fitting for the energy spectra of ^6Li and ^7Li fragments (E337).

	^8Li				^9Li			
	Au	Tm	Sm	Ag	Au	Tm	Sm	Ag
$(Inc.)N_0$	1425.02	1915.49	2623.76	85.29	330.91	581.88	1120.34	70.91
$(Inc.)N_f$	600.57	672.88	1227.50	21.86	242.74	332.44	491.80	71.43
χ^2/n	9.14	21.32	58.30	16.25	29.47	9.16	23.40	6.05
$(M2)N_0$	525.38	455.00	382.24	21.89	130.88	150.62	162.68	18.06
$(M2)N_f$	266.7	271.16	296.81	8.29	86.28	62.33	112.42	30.52
χ^2/n	8.57	10.85	19.50	6.36	5.22	5.48	4.96	2.68
$(M3)N_0$	54.98	44.02	24.75	2.42	17.45	16.14	15.28	5.23
$(M3)N_f$	41.36	28.53	20.99	2.27	0.974	6.76	4.91	-0.335
χ^2/n	3.94	2.36	1.99	1.18	1.42	0.93	0.57	0.53

Table 26: Fitting parameters obtained in deformed moving source model fitting for the energy spectra of ^8Li and ^{9} fragments (E337).

	^7Be				^9Be			
	Au	Tm	Sm	Ag	Au	Tm	Sm	Ag
$(Inc.)N_0$	33.37	61.63	15.04	14.80	87.80	141.91	77.62	32.12
$(Inc.)N_f$	24.47	47.01	8.81	7.85	92.86	130.69	112.91	30.09
χ^2/n	9.99	3.37	9.79	2.28	11.10	31.02	24.97	3.71
$(M2)N_0$	13.72	16.53	2.33	4.45	29.15	29.29	9.91	7.85
$(M2)N_f$	8.23	14.72	1.74	1.61	29.58	33.45	17.25	8.23
χ^2/n	1.57	1.53	2.21	1.85	11.78	16.84	8.48	3.63
$(M3)N_0$	1.600	1.864	0.2204	0.4143	3.425	2.361	0.5748	1.0781
$(M3)N_f$	1.1708	1.0048	0.0697	0.46802	2.0492	2.9556	1.2144	1.0689
χ^2/n	1.31	0.81	0.29	0.69	4.83	3.81	1.61	1.34

Table 27: Fitting parameters obtained in deformed moving source model fitting for the energy spectra of ^7Be and ^9Be fragments (E337).

	^{10}Be			
	Au	Tm	Sm	Ag
$(Inc.)N_0$	71.04	86.14	255.16	23.64
$(Inc.)N_f$	113.43	113.00	95.87	12.42
χ^2/n	6.32	4.15	15.18	2.74
$(M2)N_0$	23.46	15.86	32.38	7.04
$(M2)N_f$	35.19	41.46	23.87	0.145
χ^2/n	6.81	3.29	5.59	2.33
$(M3)N_0$	2.1695	1.2265	1.6929	0.7384
$(M3)N_f$	5.0451	4.5776	3.1624	0.17614
χ^2/n	1.84	1.87	2.29	1.22

Table 28: Fitting parameters obtained in deformed moving source model fitting for the energy spectra of $10Be$ fragments (E337).

Acknowledgments

I would like to acknowledge the guidance and advice of Prof. T. Murakami, who is the project manager of the KEK target multifragmentation experiments (KEK-PS E337 and E393). I gratefully acknowledge helpful discussions with Prof. K. Imai on several points in the paper. His comments helped to clarify the article. I am pleased to express my gratitude thanks to the considerable assistance and efforts of Prof. K.H. Tanaka. The experiment was made possible largely through his suggestions on the detector construction and his skilled beam engineering.

I wish to thank the efforts of all the members of the E337/E393 collaboration. I would like to acknowledge Prof. K. Nakai for the assistance for this work. I was fortunate to have had the assistance of Prof. Y. Tanaka for the development of the data acquisition system. I am also deeply indebted to Mr. Y. Yamanoi of the KEK-PS Beam Channel Group for his considerable assistance and time for the beam line construction and development of the vacuum system. I wish to express my gratitude to Prof. Y. Nagasaka for building the Linux-PC based data acquisition system.

It is a pleasure to acknowledge the hospitality and encouragement of the member of KEK-PS Accelerator Group and Beam-Channel Group for their successful double throw extraction, beam line construction, and beam transportation with small beam halo. I am indebted to the Counter-hall crew, Electronics and Online Group, the Computation Center, the Mechanical Engineering Center at KEK for their indispensable assistance. I also express my thanks to Prof. J. Chiba for his considerable efforts on the beam time managements.

I am indebted to all the participants in the studies for their gracious cooperation. I wish to thank all the member of Nuclear Physics Group and Particle & Nuclear Physics Group of Kyoto University for their hospitality and memberships. Thanks are due to Prof. H. Sakaguchi, Prof. M. Nakamura, and Prof. Y. Yosoi for their helpful suggestions. I am pleased to acknowledge the considerable encouragement and friendships of the members of the Nuclear Physics Group,

This work was supported in part by a Grant-in-Aid for Scientific Research (C) (No. 06640423 and No. 06640389) of the Japan Ministry of Education, Science, Sports and Culture (Monbusho). The author acknowledge the receipt of the JSPS Research Fellowships for Young Scientists.

References

[1] H.H. Heckman et al., Phys. Rev. Lett. **28**, 926 (1972).

[2] K. Beg and N.T. Porile, Phys. Rev. C **3**, 1631 (1970).

[3] Ø Scheidemann and N.T. Porile, Phys. Rev. C **14**, 1534 (1976).

[4] S. Biswas and N.T. Porile, Phys. Rev. C **20**, 1467 (1979).

[5] A.M. Zebelman et al., Phys. Rev. C **11**, 1280 (1980).

[6] N.T. Porile and A.S. Hirsh et al., Phys. Rev. C **39**, 1914 (1988).

[7] G.D. Westfall et al., Phys. Rev. Lett. **37**, 1202 (1976).

[8] H. Sato and K. Yazaki, Phys. Lett. B **98**, 153 (1981).

[9] V.I. Manko and S. Nagamiya et al., Nucl. Phys. A **384**, 475 (1982).

[10] H. En'yo et al., Phys. Lett. B **159**, 1 (1985).

[11] A.E. Glassgold et al., Ann. Phys. **6**, 1 (1959).

[12] H.G. Baumgardt et al., Z.Phys. A **273**, 359 (1975).

[13] H.A. Gustafsson et al., Phys. Rev. Lett. **53**, 544 (1984).

[14] G.S. Bertsh and S. Das Gupta, Phys. Rep. **160**, 189 (1988).

[15] G.F. Bertsch and S. Das Gupta, Phys. Rep. **160**, 189 (1988).

[16] H.M. Xu et al., Phys. Rev. C **48**, 933 (1993).

[17] D.R. Fortney and N.T. Porile, Phys. Rev. C **21**, 2511 (1980).

[18] A.S. Hirsh and N.T. Porile et al., Phys. Rev. C **29**, 508 (1984).

[19] L.G. Moretto et al., Phys. Rev. Lett. bf 74, 1530 (1995).

[20] H.H. Heckmann et al., Phys. Rev. C **17**, 1651 (1978).

[21] H.H. Heckmann, Phys. Rev. C **34**, 1333 (1986).

[22] J. Dreute et al., Phys. Rev. C **44**, 1057 (1991).

[23] C. Lewenkopf et al., Phys. Rev. C **44**, 1065 (1991).

[24] A.I. Warwick et al., Phys. Rev. C **27**, 1083 (1983).

[25] M.L. Gilkes et al., Phys. Rev. Lett. **73**, 1590 (1994).

[26] P. Kreutz et al., Nucl.Phys. A **556**, 672 (1993).

[27] R.T. de Souza et al., NIM. A **295**, 109 (1990).

[28] J. Pouthas et al., NIM. A **357**, 418 (1995).

[29] K. Kwiatkowski et al., NIM. A **360**, 571 (1995).

[30] S.P. Avdeyev et al., NIM. A **332**, 149 (1993).

[31] A.B. Migdal, Rev. Mod. Phys **50**, 107 (1978).

[32] H. Stöcker and W.Greiner, Phys. Rep. **137**, 277 (1986).

[33] P.J. Siemens Nucl. Phys. A **428**, 189c (1984).

[34] N.K. Glendenning. Phys. Rev. D **46**, 1274 (1992).

[35] R. Tamagaki Prog. Theor. Phys. Suppl. No. **112**, 1 (1993).

[36] D.Q. Lamb et al., Phys. Rev. Lett. **41**, 1623 (1978).

[37] H. Jaqaman et al., Phys. Rev. C. **27**, 2782 (1983);**29**, 2067 (1984).

[38] P.J. Siemans, Nature **305**, 410 (1983).

[39] A.L. Goodman, Phys. Rev. C. **30**, 851 (1984).

[40] Introduction to Percolation Theory. Taylor & Francis, London (1992).

[41] J.E. Finn et al., Phys. Rev. Lett. **49**, 1321 (1982).

[42] D.H.E. Gross and Meng Ta-chung. 4th Nordic Meeting on Intermediate and High Energy Physics, page 29, Geilo Sportell, Norway (1981).

[43] J.P. Bondorf, Nucl. Phys. A **444**, 460 (1985).

[44] M.E. Fisher, Physics (N.Y.) **3**, 255 (1967).

[45] A.D. Panagitou et al., Phys. Rev. Lett. **52**, 496 (1984).

[46] X. Campi, Phys. Lett. B **208**, 351 (1988).

[47] W. Trautmann et al., Z. Phys. A **344**, 447 (1993).

[48] W. J. Aichelin et al., Phys. Rev. C **37**, 2451 (1988).

[49] C.A. Ogilvie et al., Phys. Rev. Lett. **67**, 1214 (1991).

[50] T. Li et al., Phys. Rev. Lett. **70**, 1924 (1993).

[51] A. Schüttauf et al., Nucl. Phys. A **607**, 457 (1996).

[52] M. D'Agostino et al., Phys. Rev. Lett. **75**, 4373 (1995).

[53] T. Li et al., Phys. Rev. C **49**, 1630 (1994).

[54] L. Phair et al., Phys. Lett. B **314**, 271 (1993).

[55] S. Pratt et al., Phys. Lett. B **349**, 261 (1995).

[56] E.E. Zabrodin, Phys. Rev. C **52**, 2608 (1995).

[57] L.V. Bravina and E.E. Zabrodin, Phys. Rev. C **54**, R464 (1996).

[58] J.A. Hauger et al., Phys. Rev. Lett. **77**, 235 (1996).

[59] J.B. Elliott et al., Phys. Lett. B **381**, 35 (1996).

[60] P.L. Jain et al., Phys. Rev. C **46**, R10 (1992).

[61] M.L. Cherry et al., Phys. Rev. C **52**, 2652 (1995).

[62] Y. Imry, Phys. Rev. B **21**, 2042 (1980).

[63] P. Labastie and R.L. Whetten, Phys. Rev. Lett. **65**, 1567 (1990).

[64] W.A. Friedman, Phys. Rev. C **42**, 667 (1990).

[65] R. Blümel et al., Nature **334**, 309 (1988).

[66] Hai-Ping Cheng and C.K. Gelbke, Phys. Rev. C **38**, 2630 (1988).

[67] A. Hüller, Z. Phys. B **93**, 401 (1994).

[68] H.A. Bethe Rev. Mod. Phys. **9**, 69 (1937).

[69] V.F. Weisskopf, Phys. Rev. **52**, 295 (1937).

[70] W. Benenson, D.J. Morrisey, and W.A. Friedman, Ann. Rev. Nucl. and Part. Science, **44**, 27 (1994).

[71] R. Brockmann et al., Phys. Rev. Lett. **53**, 2012 (1984).

[72] S.A. Bass et al., Phys. Lett. B **335**, 289 (1994).

[73] C. Müntz et al., Z. Phys. A **352**, 175 (1995).

[74] J. Pochodzalla et al., Phys. Rev. C **35**, 1695 (1987).

[75] W. Bauer, Phys. Rev. C **51**, 803 (1995).

[76] C. Schwarz et al., Phys. Rev. C **48**, 676 (1993).

[77] T.K. Nayak et al., Phys. Rev. C **45**, 132 (1992).

[78] G.J. Kunde et al., Phys. Lett. B **272**, 202 (1991).

[79] C.B. Chitwood et al., Phys. Lett. B **172**, 27 (1986).

[80] Xi Hongfei et al., Nucl. Phys. A **552**, 281 (1993).

[81] H.M. Xu et al., Phys. Rev. C **40**, 186 (1989).

[82] F. Hoyle, Monthly Notices of the Royal Astronom. Soc. **106**, 343 (1946).

[83] S. Albergo et al., Nuovo Cimento A **89**, 1 (1985).

[84] S. Albergo et al., Nuovo Cimento A **101**, 815 (1989).

[85] D. Hahn and H. Stöcker, Nucl. Phys. A **476**, 718 (1988).

[86] P. Braun-Munziger et al., Nucl. Lett. B **344**, 43 (1995); B **365**, 1 (1996).

[87] A.D. Panagitou et al., Phys. Rev. C **53**, 1353 (1996).

[88] M.B. Tsang, W.G. Lynch, H. Xi and W.A. Friedman, Phys. Rev. Lett. **78**, 3836 (1997).

[89] J. Pochodzalla et al., Phys. Rev. Lett. **75**, 1040 (1995).

[90] M.B. Tsang et al., Phys. Rev. C **53**, R1057 (1996).

[91] M.J. Huang et al., Phys. Rev. Lett. **78**, 1648 (1997).

[92] J.B. Natowiz et al., Phys. Rev. C **52**, R2322 (1995).

[93] V.A. Karnauknov et al., JINR pre-print E7-96-182 (1996).

[94] X. Campi et al., Phys. Lett. B **385**, 1 (1996).

[95] A. Kolomiets et al., Phys. Rev. C **54**, R472 (1996).

[96] W. Xi et al., Phys. Rev. C **54**, R2163 (1996).

[97] Y.G. Ma et al., LPC pre-print LPCC 96-10 (1996).

[98] A. Ohnishi, JAERI-Conf, 98-012, 6 (1998).

[99] A. Ohnishi and J. Randrup, Phys. Rev. Lett. B **75**, 596 (1995).

[100] L.P. Remsberg and D.G.Perry, Phys. Rev. Lett. **35**, 361 (1975).

[101] J.B. Comming et al., Phys. Rev. B **134**, 167 (1964).

[102] N.T. Porile et al., Phys. Rev. C **19**, 1832 (1979).

[103] N.T. Porile et al., Phys. Rev. Lett. **43**, 918 (1979).

[104] J.A. Urbon et al., Phys. Rev. C **21**, 1048 (1980).

[105] D. R. Fortney and N. T. Porile, Phys. Rev. C **2511** (1980).

[106] W.c. Hsi et al., Phys. Rev. C **58** R13(1998).

[107] T. Maruyama and K. Niita, Prog. Theor. Phys. **97**, 579 (1997).

[108] W. Bauer, Phys. Rev. Lett. **69**, 1888 (1992).

[109] L. Phair and W.Bauer et al., Phys. Lett. B **314**, 271 (1993).

[110] D.O. Handzy et al., Phys. Rev. C **51**, 2237 (1995).

[111] J.R. Adam et al., Journal. App. Phys. **39**, 5173 (1968).

[112] K.H. Tanaka et al., Nucl. Phys. A **583**, 581 (1995)

[113] T. Murakami et al., Perspectives in Heavy Ion Physics (World Scientific, Singapore, 1996), p.152.

[114] H. Ochiishi et al., Nucl. Instrum. Methods A **369**, 269 (1996).

[115] J. Hubele et al., Z. Phys. A **340**, 263 (1991).

[116] K.H. Tanaka et al, Università degli Studi di Milano N.111, 208 (1997).

[117] J. Murata et al, Università degli Studi di Milano N.111, 216 (1997).

[118] T. Murakami et al, Università degli Studi di Milano N.111, 221 (1997).

[119] J. Murata, Master Thesis, Kyoto University (1996).

[120] Y. Ohkuma, Master Thesis, University of Tsukuba (1997).

[121] F. Kosuge, Master Thesis, Tokyo University of Science (1998).

[122] Y. Shibara, Master Thesis, Tokyo University of Science (1998).

[123] R. Kubohara, Master Thesis, Tokyo University of Science (To be published in 1999).

[124] Y.J. Tanaka, Master Thesis, Kyoto University (To be published in 1999).

[125] Y. Sugaya et al., NIM. A **368**, 635 (1996).

[126] L.C. Northcliff and R.F. Schilling, Nucl.Dat.Tab. A **7**, 233 (1970).

[127] Y. Tanaka et al., Nucl. Instrum. Methods A **425**, 323 (1999).

[128] M. Tairadate, KEK Internal **94-17**.

[129] L.G. Christophorou et al. NIM **163**, 141 (1979).

[130] L.P. Csernai, H. Stöcker, P.R. Subramanian, G. Buchwald, G. Graebner, A. Rosenhauer, J.A. Maruhn and W. Greiner, Phys. Rev. C **28**, 2001 (1983).

[131] H.A. Gustafsson et al., Phys. Rev. Lett. **53**, 544 (1984).

[132] S. Albergo and A. Tricomi, in Proc. of XXXVI Int. Winter Meeting on Nucl. Phys., Bormio, Italy, 1998 (edited by I. Iori); S. Albergo (private Communication).

[133] N. Ohtsuka et al., JAERI-Conf, 97-007, 83 (1997); (private Communication).

[134] J. Cugnon, Nucl. Phys. A **462**, 751 (1987).

[135] W. Bauer et al. Nucl. Phys. A. **452**, 699 (1986).